National Library of Canada
Acquisitions and Bibliographic Services Branch
395 Wellington Street
Ottawa, Ontario
K1A 0N4

Bibliothèque nationale du Canada
Direction des acquisitions et des services bibliographiques
395, rue Wellington
Ottawa (Ontario)
K1A 0N4

Your file Votre référence

Our file Notre référence

NOTICE

The quality of this microform is heavily dependent upon the quality of the original thesis submitted for microfilming. Every effort has been made to ensure the highest quality of reproduction possible.

If pages are missing, contact the university which granted the degree.

Some pages may have indistinct print especially if the original pages were typed with a poor typewriter ribbon or if the university sent us an inferior photocopy.

AVIS

La qualité de cette microforme dépend grandement de la qualité de la thèse soumise au microfilmage. Nous avons tout fait pour assurer une qualité supérieure de reproduction.

S'il manque des pages, veuillez communiquer avec l'université qui a conféré le grade.

La qualité d'impression de certaines pages peut laisser à désirer, surtout si les pages originales ont été dactylographiées à l'aide d'un ruban usé ou si l'université nous a fait parvenir une photocopie de qualité inférieure.

Canada

A C-GRID OCEAN CIRCULATION MODEL AND EDDY SIMULATION

By

Weimin Xu

SUBMITTED IN PARTIAL FULFILLMENT OF THE
REQUIREMENTS FOR THE DEGREE OF
DOCTOR OF PHILOSOPHY
AT
MCGILL UNIVERSITY
MONTREAL, QUEBEC
MARCH, 1994

ISBN 0-612-00147-4

Contents

List of Tables

List of Figures

Abstract

We have developed a C-grid primitive equation ocean general circulation model with Cartesian and β-plane geometry. Temperature is the only state variable. The C-grid gives better results than the B-grid in reproducing the growth rates of linear unstable modes of the Rayleigh-Bénard equations. A semi-implicit scheme is used to treat the Coriolis term, which is important for efficient integration in coarse resolution large scale modelling studies. A new viscosity term which has a damping effect only on the divergence field associated with gravity waves is also introduced. The model can reproduce sucessfully most of the coarse resolution model results of other studies. The biharmonic and Smagorinsky frictional parameterizations are not as efficient as our scheme in eliminating noise in the vertical velocity field.

This model is used to study the effects of no slip or free slip boundary conditions on the energetics and northward heat transport in the eddy resolving regime. The divergence dissipation term is used only in the subpolar gyre region, where the Rossby radius of deformation is not well resolved. This term has little effect elsewhere in the model domain. The eddy energetics is sensitive to the lateral boundary conditions used. Increasing vertical resolution can increase the basin average and midlatitude free jet energetics, but its effect is much less than that due to different lateral boundary conditions. The northward heat transports by eddies and mean flow are also examined.

The effect of a restoring condition is compared to a zero heat capacity atmospheric model as a surface boundary condition for the eddy resolving model. Two significant differences are found with the use of the zero heat capacity atmospheric model. First,

both eddy and mean kinetic energy near the midlatitude free jet are increased. Second, the vertical profiles of standard temperature deviation (eddy available potential energy) become more realistic.

An analysis of the mean advection and eddy convergence terms in the mean momentum equations shows that both enhanced horizontal resolution and the zero heat capacity atmospheric model can increase the midlatitude jets in the surface and deep layers. The eddy momentum convergence in midlatitudes is the dominant ageostrophic contribution to both the mean zonal flow and its variation. The mean advection is consistently less important. The effects of eddies have been further investigated by using the mean vorticity equation. The results again show that the eddy convergence term is the most important ageostrophic term, and can be as important as the geostrophic effect. The mean vorticity equation budget shows a similar sensitivity to the horizontal resolution and zero heat capacity atmospheric model as for the momentum equations.

Résumé

Nous avons développé un modèle de circulation générale océanique aux équations primitives avec une géométrie Cartésienne et de plan bêta à l'aide d'une grille C. Dans ce modèle, nous introduisons un schéma semi-implicite pour traiter le terme de Coriolis qui est important pour une intégration efficace dans le cadre de modèle à grande échelle et à résolution grossière. Nous introduisons également un nouveau terme de viscosité qui amortit seulement le champ de divergence associé aux ondes de gravité. Notre modèle peut reproduire avec succès la plupart des résultats obtenus avec un modèle de résolution grossière. Les paramétrisations de friction biharmonique et de Smagorinsky ne sont pas aussi efficaces que notre schéma dans l'élimination du bruit dans le champ de vitesse verticale.

Ce modèle a été utilisé pour étudier le transport d'énergie et de chaleur vers le nord en régime de résolution des tourbillons. Le terme de divergence de la dissipation est seulement utilisé dans la région du tourbillon subpolaire, où le rayon de Rossby de déformation n'est pas bien résolu. Ce terme est peu important dans les autres régions du modèle. L' énergie des tourbillons est sensible aux conditions de frontières latérales employées. Augmenter la résolution verticale peut augmenter la moyenne du bassin et l'énergie du jet libre aux latitudes moyennes, mais son effet est bien moindre que celui dû aux conditions de frontières latérales différentes. Les transports de chaleur vers le nord par l'écoulement moyen et les tourbillons sont aussi examinés.

L'effet d'une condition de rappel est comparé à un modèle avec une atmosphère de capacité thermique nulle comme une condition de frontière de surface pour un modèle à résolution des tourbillons. Deux importantes différences sont trouvées.

Premièrement, aussi bien l'énergie cinétique moyenne que celle des tourbillons est augmentée près du jet des latitudes moyennes. Deuxièmement, le profil vertical de la déviation de la température standard (l'énergie potentielle disponible des tourbillons) est plus réaliste.

En augmantant la résolution horizontale et en employant une atmosphère ayant capacité thermique nulle, on peut renforcer les jets des latitudes moyennes à la surface et aux couches profondes. La convergence de la quantité de mouvement par les tourbillons des latitudes moyennes a une contribution agéostrophique importante à l'écoulement de moyenne zonale et à sa variation. L'advection moyenne est moins importante. Le forçage par le vent peut aussi renforcer les jets des latitudes moyennes par la friction verticale. Les effets des tourbillons ont été étudié d'avantage avec l'équation du tourbillon moyen. Les résultats démontrent encore que le terme de convergence des tourbillons est le terme agéostrophique le plus important et que celui-ci peut être aussi important que l'effet géostrophique. La sensibilité du budget de l'équation du tourbillon moyen au modèle à résolution horizontale avec une atmosphère sans capacité thermique est semblable à celle des équations du mouvement.

List of Symbols

x,y,z: eastward, northward, upward Cartesian coordinates

u: x component of velocity (eastward)

v: y component of velocity (northward)

w: z component of velocity (upward)

p: pressure

t: time

f: Coriolis parameter

β: variation of the Coriolis parameter with latitude

ζ: relative vorticity

ρ: density

ρ_0: reference density

T: temperature

α: thermal expansion coefficient, 2.5 $\times 10^{-4}$ °C^{-1}

D: horizontal divergence

H: depth of ocean

A_{MH}, A_{HH}: horizontal viscosity and diffusivity

A_{MV}, A_{HV}: vertical viscosity and diffusivity

λ: eddy viscosity operating on the horizontal divergence

τ_x, τ_y: surface wind stresses in x, y directions

T_A: apparent (equivalent) atmospheric temperature

T_1: top layer ocean temperature

Δz_1: top layer model depth

τ_R: restoring time constant for surface thermal forcing

Q^T: surface heat flux

$\overline{P}$: mean available potential energy

P': eddy available potential energy

$\overline{K}$: mean kinetic energy

K': eddy kinetic energy

List of Abreviations

PE: primitive equations

QG: Quasi-geostrophic equations

FRS: free slip boundary conditions

NOS: no slip boundary conditions

SST: sea surface temperature

ZHCA: zero heat capacitiy atmosphere

WBC: western boundary current

WBL: western boundary layer

CME: Community Modeling Effort

Acknowledgments

The author wishes to express his sincere gratitude to his thesis advisor, Dr. Charles A. Lin, whose dedicated guidance and supervision made it possible for this research to be accomplished.

The author is grateful to the late Dr. André Robert, the thesis co-supervisor, for his help and guidance during the development of the numerical model.

Drs. K. Bryan and A. Arakawa answered some important questions regarding the numerical aspects of the model. Dr. R. Greatbatch participated in the work of Chapter 4 on the use of the zero heat capacity atmospheric model as a surface boundary condition. The author would also like to thank Drs. B. Barnier, C. Chen, P. Chen, D. Dietrich, G. Flierl, P. Galbraith, W. Gough, K. Hedstrom, R. Lu, J. Marotzke, D. Marshall, J. Marshall, L. Mysak, T. Reynaud, J. Sheng, D. Stammer, D. Straub, T. Warn, A. Weaver, and S. Xie for interesting and informative discussions. M. Beland and A. Schwartz provided excellent technical assistance in computing; Ms. U. Seidenfuss provided drafting help with the figures, and Mr. D. Le Roux and Mr. M. Klasa translated the abstract to French.

Computing time on the NEC SX3 supercomputer for this work was provided by Dr. M. Béland of Recherche en prévision numérique, Atmospheric Environment Service, Canada. The use of the computing facilities of CERCA (Centre de Recherche en Calcul Appliqué) is also gratefully acknowledged.

Statement of Originality

Convection simulation

- The linear Rayleigh-Bénard convection equations have been used to show that C-grid is better than B-grid in simulating linear convective instability.
- Non-hydrostatic effect becomes important only if the horizontal grid sizes are smaller than the depth of unstable stratification.

(The research paper is presented in Appendix A).

Model formulation

- A divergence dissipation scheme is introduced to eliminate noise in the C-grid model due to grid point averaging of the Coriolis terms, when the horizontal grid size is larger than the Rossby radius of deformation.
- A semi-implicit treatment of the Coriolis terms, useful for coarse resolution model studies, allows for larger time step than explicit methods.

Effects of lateral boundary conditions

- Effects of no slip and free slip boundary conditions have been examined in an eddy resolving primitive equation model with both wind and thermal forcing.
- The basin averaged eddy energetics for no slip conditions are stronger than for free slip conditions, with enhanced baroclinic and barotropic instabilities in the former case. The mean kinetic energy is however about twice as large for the free slip case. In contrast, quasi-geostrophic models show both eddy and mean kinetic energies are much larger for free slip than for no slip conditions.
- Free slip conditions results in stronger northward heat transport in the subpolar gyre due to the overshooting of the western boundary current.

Effects of surface boundary conditions

- The zero heat capacity atmospheric model has been used as a surface boundary condition. The simulated eddy variability has more eastward extension than the more conventional restoring condition on surface temperature.
- The simulated temperature variance can have maxima at surface or subsurface levels, while the restoring condition yields a maximum variance below the surface.

Maintenance of midlatitude free jets

- Both increasing horizontal resolution and the zero heat capacity atmospheric model can increase the midlatitude jets in the surface and deeper layers. The effects of eddies in midlatitude is the dominant ageostrophic contribution to the mean zonal flow and its variation. The mean advection is consistently less important. A similar conclusion is obtained through an analysis of the vorticity equation.

Chapter 1

Introduction

1.1 An overview

There has been considerable scientific, economic and political interest in understanding the mechanisms of climate change and its impact on the environment and human activity. The global oceans have a large heat capacity, with the top few meters having the same heat capacity as the entire atmosphere. The oceans also transport about half of the heat from low to high latitudes required to maintain the present climate. The understanding of climate change necessarily leads one to consider the global thermohaline circulation in the ocean and its heat transport.

Coupled ocean-atmosphere models have been used to study both past and present climates and climate change; these models currently represent the best means to obtain qualitative estimates and predictions of potential climate change. However, results from large scale ocean circulation models are dependent on the parameterizations of eddy effects on the larger, slower scales of motion. The precise nature of these parameterizations are not well understood.

Ocean currents and their associated fields of pressure, temperature and density vary significantly in both time and space throughout the ocean. Such variability (eddies) in fact contains more energy than any other form of motion. These eddies have a characteristic spatial scale of a few hundred kilometers and a time scale of

weeks to months. Their importance for mixing, heat and mass transport as well as their potential role on climate are subjects of current research. Although there have been field programs to measure eddy currents, the available observational data is still very limited due to the difficulty of obtaining observations in the open ocean. Eddy resolving numerical models can be used to better understand the role of eddies on the large scale flow in the ocean.

1.2 Convection simulation

Convection is important for the thermohaline circulation and tracer transport. Convection processes are not well understood as they appear to be transitory in both space and time (Killworth, 1989). Killworth (1983) summarized the limited available observations into two catogories of convections. The first is shelf-slope convection, as typified by dense water formation in the Weddell Sea. Intense winter cooling causes brine release through the formation of sea ice, forming wide shallow reservoirs of dense water. With the help of the prevailing circulation, they move off the shelf and descend along the slope. The second category is open-ocean convection. Typical examples include the Medoc (the MEDOC Group, 1970), Labrador Sea (Clarke and Gascard, 1983), Weddell Sea chimneys (Gordon, 1978; Killworth, 1979), and the polynya (Martinson et al., 1981). This type of convection take places in a narrow chimney of width 10 to 50 km, and is often accompanied by vigorous eddying at the chimney's edges. The MEDOC Group (1970), based on observations from the Mediterranean, proposed that the deep water formation process could be divided into three phases: preconditioning, violent mixing, and sinking and spreading.

Convection is currently parameterized in large scale numerical ocean circulation models. A hierarchy of such models has been summarised in Mysak and Lin (1990). In the near future, it may be possible to have sufficient horizontal resolution to explicitly resolve convective cells in large scale models. These cells have horizontal scales of less than a few kilometers. It is thus important to determine the criteria for resolving

convection in models, and the most appropriate schemes needed. The effects of the hydrostatic approximation and different finite difference schemes have been studied by Xu and Lin (1993) using the linear Rayleigh-Bénard equations. The paper is presented in Appendix A.

1.3 Eddy resolving numerical models

Since the pioneering eddy resolving studies of Holland and Lin (1975a, b) using a two-layer, adiabatic, wind-driven primitive equation (PE) model, eddy resolving models have used both the quasi-geostrophic (QG) and PE equations. Semtner and Holland (1978) compared QG models with the PE model of Semtner and Mintz (1977) and found that QG models can reproduce most of the basic dynamical features of a mid-latitude PE model. As the QG model is much more efficient computationally than a multi-level PE model, most sensitivity studies have used the QG equations (Holland, 1978; Schimtz and Holland, 1982, 1986; Holland and Schimtz, 1985; Barnier et al., 1991; Haidvogel et al., 1992). There are however limitations to QG models. It is difficult to include long term changes in basic stratification and its geographic variation, and it is not possible to examine the production of various water masses and the thermohaline circulation (Semtner and Holland, 1978; Bryan, 1987; Bryan and Holland, 1989; Treguier, 1992). Han (1975), Robinson et al. (1977), Semtner and Mintz (1977), Cox (1985), Boning (1989), Bryan, (1986, 1987, 1991), Bryan and Holland (1989), Boning and Budich (1992), Semtner and Chervin (1988, 1992) used PE models with both thermal and wind forcing to study eddy generating mechanisms and their effects on the large scale circulation.

Holland et al. (1983) provided a review of eddy resolving model studies. They identified four areas of significant mean flow in eddy resolving numerical models. They are strong western boundary currents and eastward flowing jets at the mid-basin zero-wind stress curl latitude for double gyre wind forcing or northern boundary currents for single gyre forcing. The other two areas are the weak, broad interior flow, with

Sverdrup dynamics, and the westward recirculation.

The origin of mesoscale variability is usually characterized by the energy transformations that maintain the eddy kinetic energy, $K' = (u'^2 + v'^2)/2$. Here, u and v denote the zonal and meridional velocities and a prime denotes instantaneous departure from the long time average. If there is no external forcing, K' can only be maintained either by conversion of mean flow kinetic energy via Reynolds stresses (barotropic instability), or by conversion of the mean potential energy via buoyancy fluxes (baroclinic instability).

Different experiments have shown that baroclinic, barotropic, and mixed baroclinic-barotropic instability can be a source of K' (Holland et al., 1983). Holland and Haidvogel (1978) suggested that realistic Gulf Stream parameters place the instability in the transition region between baroclinic and barotropic processes. In the interior, the relatively weak eddy field tends to be more barotropic than the strong current eddies; they result from the radiation of energy outward from the strong current region. For the strong current eddies, ageostrophic horizontal and vertical advections and strong baroclinic conversion are believed to be dominant processes (Spall and Robinson, 1990).

Cox (1985) applied the PE model of Bryan (1969) to a basin scale domain of the North Atlantic. This simulation showed features suggested by recent wind-driven theories of ocean circulation (Rhines and Young, 1982; Luyten et al., 1983). Boning (1989) examined the effect of topography on eddy simulation, using the same model as Cox. Boning and Budich (1992) also examined the sensitivity of the horizontal resolution. Bryan (1986, 1987, 1991) investigated the effect of eddies on the northward heat transport, using the above model results.

The previous eddy resolving models have only one state variable, temperature. Bryan and Holland's Community Modeling Effort (CME) (1989) extended Cox's (1985) study of the North Atlantic to include realistic topography and both temperature and salinity as state variables. They also included one-dimensional mixed layer physics and seasonal forcing. The seasonality of the depth of the thermocline

and some water mass properties were succesfully simulated. Semtner and Chervin (1988, 1992) applied the Bryan-Cox-Semtner model (Bryan, 1969; Semtner, 1974; Cox, 1984) to the global ocean, with a horizontal resolution of 0.5° in both the zonal and meridional directions. They used observational data (Levitus, 1982) as initial conditions in the robust diagnostic mode (Sarmiento and Bryan, 1982).

All of these studies used the Arakawa B-grid for horizontal discretization. For horizontal grid sizes less than Rossby radius of deformation, the Arakawa C-grid is more accurate (Arakawa and Lamb, 1977; Batteen and Han, 1981; Bryan, 1989; Xu and Lin, 1993). Indeed, the C-grid has been used successfully in studies of coastal circulations (Blumberg and Mellor, 1987; Mellor, 1992), and convective adjustment (Brugge et al., 1991; Jones and Marshall, 1993; Legg and Marshall, 1993; Lin and Dietrich, 1994). Hurlburt et al. (1992) used a C-grid layer model to study the wind-driven circulation of the North Pacific. Killworth et al. (1991) and Treguier (1992) suggested the use of the C-grid to avoid numerical difficulties near steep topography. However, C-grid models have some difficulties due to the grid point averaging of the Coriolis terms (Batteen and Han, 1981; Semtner, 1986a). All these difficulties may be one of the reasons why B-grid model of (Bryan, 1969; Semtner, 1974; Cox, 1984) have been usually used for basin scale eddy resolving model studies with both wind and thermal forcings.

It is thus desirable to develop a new C-grid model so that it can be applied to both noneddy and eddy resolving regimes. Note that results from coarse resolution simulations can be used as initial conditions of eddy resolving integration, as it is still not feasible to integrate eddy resolving models sufficiently long to obtain a statistical equilibrium with currently available computing resources. In addition, results from coarse resolution models can be compared with those of eddy resolving models to identify the effects of eddies on various physical processes.

1.4 Organisation of the thesis

In this thesis, we develop a C-grid model which can be used for both coarse and fine resolution studies. The model is used to examine the effects of different lateral boundary conditions (free slip and no slip) and surface thermal boundary conditions (restoring condition, and zero heat capacity atmosphere model) on eddy energetics and northward heat transport in eddy resolving regime. These process studies help in the understanding of more complex eddy resolving experiments, and also point to improvements in eddy simulation.

Chapter 2 decribes the model formulation, verification and frictional parameterizations. Chapters 3 and 4 investigate the effects of lateral and surface thermal boundary conditions respectively. Chapter 5 is a diagnostic study of the momentum and vorticity balance. Table 1.1 presents a summary of the horizontal resolutions, the model domain sizes, and the lateral and surface thermal boundary conditions used. The model domain is slightly reduced in Chapters 3 and 4 to reduce the computational requirements at eddy resolving scales. The conclusions are presented in Chapter 6.

Table 1.1: A table showing the east-west (Δx) and north-south (Δy) resolution, the zonal (L_x) and meridional (L_y) model domain size, the lateral boundary conditions (free slip (FRS), or no slip (NOS)), and the surface thermal boundary conditions (restoring, zero heat capacity atmosphere (ZHCA) model) used in Chapters 2 to 5.

Chapter	Δx(km)	Δy(km)	L_x(km)	L_y(km)	FRS	NOS	restoring	ZHCA
2.	220 100	220 115	4400	5500	yes	no	yes	no
3.	40	40	4000	4800	yes	yes	yes	no
4.	30	30	4000	4800	no	yes	yes	yes
5.	**analysis of momentum and vorticity balances of Chapters 3 and 4**							

Chapter 2

Model formulation and verification, and frictional parameterizations

2.1 Model equations and boundary conditions

The governing equations are the primitive equations with the Boussinesq and hydrostatic approximations. They consist of the horizontal momentum equations, the temperature equation, the hydrostatic approximation, the incompressibility condition, and the equation of state. They are shown below as Equations (2.1)-(2.6) respectively. The notation used is standard, and a description of the symbols used is given in the List of Symbols.

$$\frac{\partial u}{\partial t} + L(u) = -\frac{1}{\rho_0}\frac{\partial p}{\partial x} + fv + \frac{\partial}{\partial z}(A_{MV}\frac{\partial u}{\partial z}) + F_x + \epsilon\lambda\frac{\partial D}{\partial x} \tag{2.1}$$

$$\frac{\partial v}{\partial t} + L(v) = -\frac{1}{\rho_0}\frac{\partial p}{\partial y} - fu + \frac{\partial}{\partial z}(A_{MV}\frac{\partial v}{\partial z}) + F_y + \epsilon\lambda\frac{\partial D}{\partial y} \tag{2.2}$$

$$\frac{\partial T}{\partial t} + L(T) = \frac{\partial}{\partial z}(A_{HV}\frac{\partial T}{\partial z}) + F_T \tag{2.3}$$

$$p_z = -\rho g \tag{2.4}$$

$$\nabla \cdot \vec{V} = 0 \tag{2.5}$$

For simplicity, we assume temperature is the only state variable in the equation of state,

$$\rho = \rho_0(1 + \alpha(T_0 - T)), \tag{2.6}$$

Here, L() is the advection operator, while F_x, F_y are the horizontal viscosity terms in the x and y directions respectively; F_T represents the horizontal diffusion terms in the temperature equation; T_0 is a reference temperature, and α is the expansion coefficient of water. The expressions for the operators L(), F_x, F_y, F_T are

$$L(\sigma) = \frac{\partial(u\sigma)}{\partial x} + \frac{\partial(v\sigma)}{\partial y} + \frac{\partial(w\sigma)}{\partial z}$$

$$F_x = \frac{\partial}{\partial x}(A_{MH}\frac{\partial u}{\partial x}) + \frac{\partial}{\partial y}(A_{MH}\frac{\partial u}{\partial y})$$

$$F_v = \frac{\partial}{\partial x}(A_{MH}\frac{\partial v}{\partial x}) + \frac{\partial}{\partial y}(A_{MH}\frac{\partial v}{\partial y})$$

$$F_T = \frac{\partial}{\partial x}(A_{HH}\frac{\partial T}{\partial x}) + \frac{\partial}{\partial y}(A_{HH}\frac{\partial T}{\partial y})$$

An additional friction term is added in the horizontal momentum equations. It is multiplied by the multiplier ϵ, which takes on a value of either 0 or 1; λ is an eddy diffusivity which operates on the horizontal divergence (D) (Sadourny, 1975). This term is added to reduce the noise which may be present in the vertical velocity field due to gravity waves (Batteen and Han, 1981). As we will show later, the inclusion of the divergence term effectively eliminates such noise.

To examine whether other forms of lateral viscosity parameterizations can be used to eliminate the noise in the vertical velocity, we also examine the effects of

biharmonic diffusion and the Smagorinsky (1963) form of eddy diffusivity. Both the biharmonic and Smagorinsky diffusive formulations are more scale selective than Laplacian friction with constant diffusivity.

The horizontal boundaries are insulating with no normal flow. At the western and eastern boundaries, we thus have

$$(u, v_n, T_n) = 0$$

and at the southern and northern boundaries

$$(u_n, v, T_n) = 0$$

Here, $()_n$ indicates a local derivative with respect to the coordinate normal to the boundary of the walls. An additional boundary condition is required for biharmonic diffusion, which is the same as above but with u,v, and T replaced by their corresponding Laplacian derivatives.

The top boundary at $z = 0$ is rigid, with a specified idealized wind stress distribution. The surface boundary condition for temperature can be either of restoring (Haney, 1971) or flux form. These conditions at z=0 can be expressed as follows.

$$A_{MV}(u_z, v_z) = (\tau_x, \tau_y)$$

$$A_{HV}T_z = Q^T$$

$$w = 0$$

The bottom boundary at $z = H$ is flat and insulating with a slip condition.

$$A_{MV}(u_z, v_z) = (\tau_x^B, \tau_y^B)$$

$$A_{HV}T_z = 0$$

$$w = 0$$

where τ_x^B and τ_y^B are bottom friction in the x and y directions respectively, parameterized as linear Rayleigh friction for its simplicity.

Our model does not include salinity, the latitudinal variation of the metric factors and the spherical curvature terms. We use a domain which is similar in size to the North Atlantic and an idealized climatology of surface thermal forcing and wind stress, to examine the large scale features of the North Atlantic circulation. Other studies (Colin de Verdiere, 1988, 1989) have also used models without salinity to investigate the large scale ocean circulation.

2.2 Method of solution

The use of a top rigid boundary condition eliminates external gravity waves. For models with a rigid top boundary, the motion can be divided into barotropic and baroclinic components. To proceed, we denote the sea surface height and atmospheric pressure by ξ_1 and p_a respectively. The pressure in the ocean is then

$$p(x,y,z) = p_a(x,y) + \rho g \xi_1 + \int_z^0 \rho g d\xi = p_s + p_h \tag{2.7}$$

where p_h is the hydrostatic component of pressure at depth z, and is given by the integrated mass field between that depth and the surface; $p_s = p_a + \rho g \xi_1$ is the surface pressure, which includes the contributions from the atmospheric pressure and sea surface topography. p_s is usually not known explicitly in this type of model. A standard way to proceed is to introduce the mass transport streamfunction, and then solve the vertically integrated vorticity equation (Bryan, 1969; Cox, 1984; Haidvogel et al., 1991). An alternate method is to solve for the surface pressure directly by using the diagnostic divergence equation (Dietrich et al., 1987, 1990; Dukowicz et al., 1993); the primary variables in this case are the pressure and velocity. We have chosen the latter approach due to its relative ease of implementation (Harlow and Welch, 1965; Duckwicz et al., 1993). In addition, the only reliable observational data for a basin scale ocean is satellite altimetry; it is thus promising to develop a model which can easily accomodate these data. The surface pressure method is also easier

to use in a domain with islands, as solving for the barotropic streamfunction would require the determination of the streamfunction along the boundary of each island. We conducted some experiments with both methods and found identical results.

The use of a rigid top boundary requires a method to ensure the vertically integrated flow be non-divergent.

$$\hat{D} = \frac{\partial \hat{u}}{\partial x} + \frac{\partial \hat{v}}{\partial y} = 0 \tag{2.8}$$

where $\hat{()}$ denotes the vertical averaging operator,

$$\hat{()} = \frac{1}{H}\int_{-H}^{0} () dz.$$

By taking the vertical average of Equations (2.1) and (2.2), we obtain

$$\frac{\partial \hat{u}}{\partial t} = -\frac{1}{\rho_0}\frac{\partial p_s}{\partial x} + \hat{G}_x \tag{2.9}$$

$$\frac{\partial \hat{v}}{\partial t} = -\frac{1}{\rho_0}\frac{\partial p_s}{\partial y} + \hat{G}_y \tag{2.10}$$

where

$$G_x = -\frac{1}{\rho_0}\frac{\partial p_h}{\partial x} - L(u) + fv + \frac{\partial}{\partial z}(A_{MV}\frac{\partial u}{\partial z}) + F_x + \epsilon\lambda\frac{\partial D}{\partial x} \tag{2.11}$$

$$G_y = -\frac{1}{\rho_0}\frac{\partial p_h}{\partial y} - L(v) - fu + \frac{\partial}{\partial z}(A_{MV}\frac{\partial v}{\partial z}) + F_y + \epsilon\lambda\frac{\partial D}{\partial y} \tag{2.12}$$

From Equations (2.9) and (2.10), we obtain a prediction equation for the vertically averaged horizontal divergence.

$$\frac{\partial \hat{D}}{\partial t} = -\frac{1}{\rho_0}\nabla^2 p_s + \frac{\partial \hat{G}_x}{\partial x} + \frac{\partial \hat{G}_y}{\partial y} \tag{2.13}$$

To eliminate external gravity waves, we set the left hand side of Equation (2.13) to zero. This results in an elliptic equation for p_s. Its solution forms the first step in the time integration procedure. After obtaining the surface pressure, the horizontal velocity fields can be determined using the momentum equations, and the vertical velocity from the continuity equation. The temperature is then obtained from the thermodynamic equation, and the complete pressure distribution from the equation of state and the hydrostatic equation. Further details of the time and space diffencing schemes are discussed below.

2.3 Finite difference schemes

The spatial finite differencing is based on the Arakawa C-grid. The distribution of the variables is shown in Figure 2.1. On a horizontal plane, the u and v points are staggered, while p, T are carried at the center of the grid cell. These variables all reside at the mid-point of a vertical layer. The vertical velocity w is defined at the center of grid cells in each layer.

Let the label (i, j, k) denote the 3-dimensional indices of the centre of a grid cell. Given the values of a model variable η at the adjacent points $(i+\frac{1}{2}, j, k)$ and $(i-\frac{1}{2}, j, k)$, we define the difference and average operators in the x-direction as follows.

$$(\delta_x \eta)_{i,j,k} \equiv \frac{\eta_{i+\frac{1}{2},j,k} - \eta_{i-\frac{1}{2},j,k}}{\delta x} \tag{2.14}$$

$$\overline{\eta_{i,j,k}}^{x} \equiv \frac{1}{2}(\eta_{i+\frac{1}{2},j,k} + \eta_{i-\frac{1}{2},j,k}) \tag{2.15}$$

Similar operators are defined in the y- and z-directions. For time differencing, we have

$$(\delta_t \eta)_{i,j,k} \equiv \frac{\eta(t+\delta t) - \eta(t-\delta t)}{2\delta t} \tag{2.16}$$

We also define

$$\overline{\eta_{i,j,k}}^{xy} \equiv \overline{\overline{\eta_{i,j,k}}^{x}}^{y} \tag{2.17}$$

We now describe the time integration procedure, starting with the temperature equation. Assuming that we know the variables at time steps n and n-1, we use them to predict their new values at time step n+1. We use superscripts to denote the time level. The finite difference form of this equation is

$$(\delta_t T)^n = -L(T)^n + {F_T}^{n-1} + (A_{HV}\delta_z T)_z^{n+1} \tag{2.18}$$

The model uses a leapfrog time step for advection and a forward time step for horizontal diffusion. An implicit scheme (Richtmyer and Morton, 1967) is used for

vertical diffusion. In case of unstable stratification, convective adjustment is done by locally increasing the vertical diffusivity from the standard value of 1 $cm^2\ s^{-1}$ to 10^4 $cm^2\ s^{-1}$ (Cox, 1984). In this way, T^{n+1} can be obtained from known fields at time steps n and n-1. The density at time step n+1 can be obtained from the temperature using the equation of state, and the pressure can then be computed using the hydrostatic equation.

$$p_{k+1} = p_k + g\rho_{k+\frac{1}{2}}\delta z_{k+\frac{1}{2}} \tag{2.19}$$

where $\delta z_{k+\frac{1}{2}} = (\delta z_k + \delta z_{k+1})/2$, and $\rho_{k+\frac{1}{2}} = (\rho_k + \rho_{k+1})/2$. Note that p_s, being independent of height, is included in Equation (2.19).

In the momentum equations, the model uses a leapfrog time step for advection and pressure gradient terms and a forward time step for both horizontal and vertical diffusion. A semi-implicit scheme is used for the Coriolis terms. However, this use of the semi-implicit method is more complicated in the C-grid than in the B-grid (Bryan, 1969), thus we give a detailed description of the formulation here.

The Coriolis term in the x-momentum equation (2.1) is represented by

$$f\overline{[av^{n+1} + (1-a)v^{n-1}]}^{xy}$$

while that in the y-momentum equation (2.2) is represented by

$$-\overline{f[au^{n+1} + (1-a)u^{n-1}]}^{xy}$$

where $0 \leq a \leq 1$. The spatial averages of the velocities in the Coriolis terms are required to conserve kinetic energy (Arakawa and Lamb, 1977). The finite difference form of the horizontal momentum equations can then be written as

$$\frac{u^{n+1} - u^{n-1}}{2\Delta t} - af\overline{(v^{n+1} - v^{n-1})}^{xy} = Q_1 \tag{2.20}$$

$$\frac{v^{n+1} - v^{n-1}}{2\Delta t} + a\overline{f(u^{n+1} - u^{n-1})}^{xy} = Q_2 \tag{2.21}$$

where

$$Q_1 = [-\frac{1}{\rho_0}\frac{\partial p^n}{\partial x} - L(u)^n + f\overline{v^{n-1}}^{xy} + \frac{\partial}{\partial z}(A_{MV}\frac{\partial u^{n-1}}{\partial z}) + F_x^{n-1} + \epsilon\lambda\frac{\partial D^{n-1}}{\partial x}]$$

$$Q_2 = [-\frac{1}{\rho_0}\frac{\partial p^n}{\partial y} - L(v)^n - \overline{\overline{f\overline{u^{n-1}}^x}}^y + \frac{\partial}{\partial z}(A_{MV}\frac{\partial v^{n-1}}{\partial z}) + F_y^{n-1} + \epsilon\lambda\frac{\partial D^{n-1}}{\partial y}]$$

Taking spatial averages $\overline{()}^{xy}$ and $\overline{f\overline{()}^x}^y$ of Equations (2.20), (2.21) and substituting them back into the equations, we obtain

$$u^{n+1} = u^{n-1} + 2\Delta t\frac{Q_1 + 2a\Delta t f\overline{Q_2}^{xy}}{1 + (2a\Delta t f)^2} \tag{2.22}$$

$$v^{n+1} = v^{n-1} + \Delta t\frac{Q_2 - 2a\Delta t\overline{f\overline{Q_1}^x}^y}{1 + (2a\Delta t)^2\overline{f^2}^y} \tag{2.23}$$

This set of equations is similar to that of Bryan (1969) for his B-grid model. However, we have assumed here that the spatial average of u^{n+1} and v^{n+1} at a grid point can be represented initially by its local value. An iteration procedure is thus needed to get the solution. The Newton-Raphson method is used to solve for the horizontal velocities; this is usually a very efficient method because the initial guess is quite close to the solution. By choosing $a \geq 1/2$, it is possible to exceed time step limitations imposed by external Rossby waves and inertial waves (Bryan, 1969; Cox, 1984; Takano, 1974).

The two-dimensional Poisson equation for the surface pressure is solved using the direct method of Dietrich et al. (1987, 1990).

The schemes used here conserves mass, momentum, energy, temperature and temperature variance (Arakawa and Lamb, 1977). A Robert/Asselin time filter (Robert, 1966; Asselin, 1972) is used to remove the computational mode associated with the leapfrog scheme.

2.4 Results and discussion

In this section, we describe the results of experiments conducted with the model in an ocean basin with similar size as the North Atlantic. The vertical structure and the values of various model parameters are shown in Tables 2.1 and 2.2 respectively. The horizontal viscosity used is larger than that used in comparable B-grid models,

as the C-grid does not have the inherent smoothing due to grid point averaging in the calculation of the pressure gradient term. Figure 2.2 shows the equivalent atmospheric temperature and wind stress forcing distributions at the upper boundary. The former is the temperature distribution, to which the top model layer temperature is restored with a time scale of τ_R=30 day (Haney, 1971). The surface forcing is an idealized form of the climatological forcing, already used in experiments with the widely distributed B-grid Bryan-Cox primitive equation model (Gough and Lin, 1992). The total zonal extent, meridional extent and depth of the model are L_x=4400 km, L_y=5500 km, and H=4000 m respectively. The mid-point of the grid in the meridional direction of the model domain is taken to be 45°N.

Different time steps are used for the momentum and temperature equations: 30 minutes for the former and 1 day for the latter (Bryan, 1984). This is done to speed up the integration of the model; due to the large thermal capacity of the ocean compared to the atmosphere, ocean models require a much longer spin-up time. Another difference is that the baroclinic Rossby radius of deformation in the ocean is only about 50 km or less, compared to about 1000 km for the atmosphere. Here, we conduct experiments with coarse horizontal resolution, with the horizontal grid length larger than the Rossby radius.

The use of a divergence friction term is a new feature of our model. Although it has been used with success in atmospheric modelling (Robert, 1981) , it has not been used in ocean models. At coarse horizontal resolution which does not resolve the radius of deformation, a large viscosity coefficient must be used in order to avoid numerical instability. The resolved motion is thus quasi-geostrophic, with the horizontal divergence being an order smaller than the vorticity. This provides a physical basis for adding this friction term.

We now compare the model results to published results of other models, primarily the Bryan-Cox B-grid model. This provides a verification of our model. However, the comparison is not exact, as the Bryan-Cox model has both the temperature and salinity as state variables, and spherical geometry. Spherical geometry and salinity

are not required to qualitatively reproduce the large scale circulation, as shown by Colin de Verdiere (1988, 1989). After the model verification, we examine the effects of two other frictional parameterizations, biharmonic and Smagorinsky friction, and compare with the divergence dissipation used in this study.

Figure 2.3 shows the barotropic streamfunction, which reflects the wind stress distribution. The mid-point between the two gyres is at approximately $45°N$, the location of the zero wind stress curl. The gyre structure and maximum barotropic streamfunction (about 20 Sv) compare well with those obtained by Gough (1991) using the Bryan-Cox B-grid model. As in other coarse horizontal resolution models, the western boundary current is wider than that observed, due to the large viscosity coefficient used in such coarse resolution models.

Figure 2.4 shows the horizontal distribution of temperature at several model levels. The surface temperature (Figure 2.4(a)) shows a predominantly zonal structure, except in the western boundary. Due to the strong western boundary current, horizontal temperature advection dominates diffusion there. In the interior, where the currents are much weaker, the two terms almost balance, and the temperature is determined by the equivalent atmospheric temperature of the surface restoring boundary condition. As the equivalent atmospheric temperature varies only with latitude, the surface temperature distribution is almost zonal. The subtropical warm pool is evident in the temperature of the second layer (Figure 2.4(b)), with a warm tongue extending northward. The isotherms show significant departures from their zonal average, as surface forcing plays a less important role in this layer compared to the top layer. Figure 2.4(c) shows the temperature just below the thermocline. Comparing with the surface temperature (Figure 2.4(a)), we see a considerable difference between the top layer and this layer in the southern part of the domain, but this difference is much less in the northern convective region. The temperature near the bottom is shown in Figure 2.4(d); the deep ocean is uniformly cold with a temperature of near 1.5°C. These features are similar to those of Bryan and Cox (1968).

Figure 2.5 shows the baroclinic pressure at different levels, obtained by removing

the vertical average of the hydrostatic pressure at each level. They compare well with those simulated using a planetary geostrophic model by Zhang et al. (1992). The top layer pressure shows that our model produces a stronger recirculation and western boundary current which extends farther north due to the use of a larger vertical diffusivity. The latter phenomenon has been noted by Bryan (1987).

The horizontal velocity distributions are shown in Figure 2.6. The flow in the top layers (Figures 2.6(a), (b)) follow the baroclinic isobars of Figure 2.5, thus showing the importance of baroclinic effects in these layers. However in the lower layers, the horizontal temperature becomes almost uniform, and the barotropic contribution becomes more important. The flow at 850 m (Figure 2.6(c)) shows similar features to the barotropic streamfunction (Figure 2.3). Figures 2.6(c), (d) show deep northern boundary currents associated with deep water formation, and deep western boudary currents which are reversed from those at the top layers. Throughout most of the deep interior ocean, there is weak northward flow. All of these features have been simulated by Bryan and Cox (1968).

Figure 2.7 shows the vertical velocity. In general, there is strong upwelling near the western and southern boundaries, and strong downwelling near the eastern and northern boundaries. These distributions are required to satisfy geostrophic and thermal wind balance. At the surface (Figure 2.7(a)), the interior distribution has upwelling in the subpolar regions and downwelling in the subtropical regions with the zero contour near the centre of the domain; this is consistent with Ekman currents produced by the surface winds. The general features are similar to those found by Bryan (1987), and Weaver and Sarachik (1990). The effects of wind stress become weaker at a deeper level (Figure 2.7(b)). In the deep ocean below the thermocline (Figures 2.7(c), (d)), the upwelling in the interior produces cold upward advection which balances the warm downward diffusion. There is a downwelling region off the western boundary, which is needed to satisfy local mass conservation (Bryan, 1987); the downwelling along the eastern boundary retreats farther north compared to the top layers.

Figures 2.8(a), (b) show the temperature and zonal velocity in a meridional section along the western boundary. The isotherms have a bowl like structure in the equatorial regions due to Ekman pumping, while they are steep and almost vertical in the high latitudes due to convection. The stratification increases toward the south, as a result of the conservation of potential vorticity: the product of the vertical derivative of density and the sine of the latitude is constant. The zonal velocities show surface westward flow at low latitudes and eastward flow at high latitudes, consistent with the barotropic flow shown in Figure 2.2. Figures 2.8(c), (d) show the temperature and meridional velocity in a meridional section through the subtropical gyre. The isotherms tilt upward toward both the western and eastern boundaries, resulting in zonal pressure gradients of opposite signs. Geostrophic balance then gives a northward flowing western boundary current in the upper layers and a southward flowing Sverdrup current in the rest of the domain. In the deep ocean, we see a southward flowing western boundary current. These features are all consistent with the generally accepted characteristic of the large scale circulation.

The surface heat flux is shown in Figure 2.9. We see a large negative flux (i.e. from ocean to atmosphere) of maximum magnitude 220 W m^{-2} near the western boundary at mid-latitudes, due to warm advection by the western boundary current. Near the southern boundary, the upwelling of cold water produces a positive heat flux. The extent of the warming flux depends on the amplitude of the wind stress near the southern boundary (Colin de Verdiere, 1988, 1989). The zonally averaged meridional heat transport (figure not shown) reaches a maximum of 0.3 PW at the mid-point of the domain, in agreement with Gough and Lin (1992).

Figure 2.10 shows the mean meridional circulation, or the thermohaline circulation. The main cell reaches a maximum amplitude of 14 Sv, with sinking concentrated in a narrow band in the high latitudes due to the surface cooling, and rising motion throughout the rest of the domain. Near the surface, there are weak cells which are due to the Ekman transport produced by the surface wind stress (Gough, 1991).

Many more experiments have been performed to test the sensitivity of the model

to different parameters. The behaviour is quite similar to that reported by Bryan (1987).

2.5 Parameterization of lateral friction

In the above section, we have shown that our model can reproduce similar results as other models based on the B-grid at coarse resolution. We now compare the effects of two other lateral frictional parameterizations, biharmonic and Smagorinsky friction, to the divergence dissipation used for the C-grid in this study. The biharmonic and Smagorinsky parameterizations are both more scale selective than Laplacian dissipation.

Biharmonic friction is much more effective at damping short, high frequency waves than Laplacian friction, but is less effective for the large scales. It has ususally only been used in eddy-resolving models (Holland, 1978; Semtner and Mintz, 1977; Cox, 1985; Bryan and Holland, 1989). To compare with Laplacian friction, we relate the coefficients of the two forms of friction as (Semtner and Mintz, 1977):

$$A_{MHB} = -\frac{1}{4} A_{MH} L^2 \tag{2.24}$$

where A_{MH} is as before, and A_{MHB} is the viscosity coefficient for biharmonic friction. This scaling relation implies that the effect of dissipation are comparable at the scale L. A similar relation applies to the diffusivities as well. For the shortest resolved scale ($L = 2\Delta x$), a biharmonic friction coefficient of $A_{MHB} = \Delta x^2 A_{MH}$ would have the same effect as Laplacian friction at the scale of $2\Delta x$. For scales increasingly large compared to $2\Delta x$, the dissipative effect becomes less effective compared to Laplacian friction.

The Smagorinsky frictional parameterization depends on the fluid deformation and was first used in an atmospheric primitive equation model (Smagorinsky, 1963). It has recently been used in coastal ocean modelling (Mellor, 1992). We reformulate

the Smagorinsky viscosity and diffusivity as:

$$A_{MH} = A_{MH0} + C_M \Delta x \Delta y \sqrt{(\frac{\partial u}{\partial x})^2 + \frac{1}{2}(\frac{\partial v}{\partial x} + \frac{\partial u}{\partial y})^2 + (\frac{\partial v}{\partial y})^2} \tag{2.25}$$

$$A_{HH} = A_{HH0} + C_H \Delta x \Delta y \sqrt{(\frac{\partial u}{\partial x})^2 + \frac{1}{2}(\frac{\partial v}{\partial x} + \frac{\partial u}{\partial y})^2 + (\frac{\partial v}{\partial y})^2} \tag{2.26}$$

where Δx and Δy are the grid sizes, and C_M and C_H are dimensionless constants. We used the velocity field from the control experiment of the previous section to compute A_{MH} with $C_M = 10$ and $A_{MH0} = 0$; the resulting viscosity varies by several orders of magnitude depending on the location, so base values A_{MH0}, A_{HH0} were included in the above formulae. Note that in coarse resolution models, A_{MH} must be sufficiently large to resolve the Munk layer, while A_{HH} can be much smaller.

To better represent the effects of these two frictional parameterizations and to compare them to that used in the previous section, we have increased the horizontal resolution to Δx =100 km, Δy=115 km in this section. We are still in the coarse resolution regime, as the horizontal resolution is still larger than the radius of deformation. Table 2.2 shows a summary of the horizontal/vertical, viscosity/diffusivity (A_{MH}, A_{HH}, A_{MV}, A_{HV}) and the divergence dissipation parameter (λ) for the different cases. We have used the same symbols A_{MH}, A_{HH} to denote the coefficients for Laplacian and biharmonic friction, with units of $cm^2\ s^{-1}$ and $cm^4\ s^{-1}$ respectively. In the case of Smagorinsky friction, the symbols denote the base values of Equations (2.25) and (2.26), with units of $cm^2\ s^{-1}$. Note that the increased horizontal resolution in this section results in a smaller value of the horizontal viscosity A_{MH}, but a larger value of the vertical viscosity; the latter is needed as the vertical resolution is not increased correspondingly (Cox, 1985).

Case 2 has Laplacian friction as in the previous section, but without the divergence dissipation, while the latter is included in Case 3. Figure 2.11 shows the vertical velocity field and the root-mean-square horizontal velocity for the two cases. We see that the divergence dissipation is very effective at removing noise in the vertical velocity field, but leaves the horizontal motion field undisturbed. Other fields (not

shown) are also relatively unchanged. Thus small scale waves are effectively removed by the divergence dissipation parameterization.

Cases 4 and 5 correspond to biharmonic and Smagorinsky friction respectively. The viscosity coefficients are chosen so that both cases are equivalent to Laplacian friction with no divergence dissipation (Case 2). For biharmonic friction, the coefficients are chosen according to Equation (2.24) so that the frictional effects are comparable to Laplacian friction at the smallest resolved scale of $2\Delta x$. For Smagorinsky friction, the background base coefficients are identical to the viscosities and diffusivities of Case 2. We see from Figure 2.12 that considerable noise still remains in the vertical velocity field with these two parameterizations. Note that even if biharmonic friction is successful at eliminating $2\Delta x$ noise, noise would appear at larger scales due to its highly scale selective nature, unless unrealistically large viscosities are used (figures not shown).

In all the experiments described in this section, the standard stability criteria are satisfied by our choice of viscosities. In each case, the Munk layer is resolved to avoid chessboard noise (Takano, 1975),

$$A_{MH} > \beta(\frac{2\sqrt{3}\Delta x}{3\pi})^3$$

due to the use of centered differences in the diffusive terms; the grid Peclet number is small enough to supress 2-grid point waves,

$$A_{MH} > \frac{U\Delta x}{2}$$

and the use of a forward time integration scheme with diffusion requires

$$A_{HH} < \frac{\Delta x^2}{2\Delta t}.$$

2.6 Summary

In this study, we have presented the formulation of a C-grid primitive equation ocean circulation model. The motivation for using the C-grid, rather than the B-gird, is

that the former performs better at high resolution (Arakawa and Lamb, 1977; Batteen and Han, 1981; Bryan , 1989; Xu and Lin, 1993). A semi-implicit treatment of the Coriolis term is introduced, in order to allow for time steps larger than that allowed by external Rossby waves and gravity waves. A divergence dissipation (Sadourny, 1975) is also introduced, which effectively removes noise in the vertical velocity field and leaves other fields relatively undisturbed. This is important as noisy vertical motion fields have been a difficulty with the C-grid. An ultimate goal is to use the model for eddy resolving experiments.

We have shown that the model at coarse resolution is able to reproduce well many of the features of the large scale ocean circulation. Most of the model comparison has been made with the widely distributed B-grid Bryan-Cox model. This provides a verification of our model at coarse resolution.

We also compared the effects of two other lateral frictional parameterizations, biharmonic and Smagorinsky friction, to the divergence dissipation used in our study. It was shown that the latter is the most effective at removing noise in the vertical velocity fields. Biharmonic friction can also be effective at eliminating noise due to 2-grid length waves, but is less effective at longer wavelengths, due to its highly scale selective feature. The Smagorinsky frictional parameterization is not as effective as the other two formulations at removing such noise.

Table 2.1: The vertical coordinate of the model and the depth of each level.

level	level depth (m)	level thickness (m)
1	25	50
2	75	50
3	150	100
4	250	100
5	400	200
6	600	200
7	850	300
8	1200	400
9	1600	400
10	2000	400
11	2400	400
12	2800	400
13	3250	500
14	3750	500

Table 2.2: A summary of the dissipative parameters used in the numerical experiments. All parameters have units of $cm^2\ s^{-1}$, except for A_{MH}, A_{HH} in Case 4, which have units of $cm^4\ s^{-1}$.

Case	A_{MH}	A_{HH}	A_{MV}	A_{HV}	λ
	Section 2.5 $\Delta x = \Delta y$=220 km				
1	4×10^9	10^7	1	1	10^{11}
	Section 2.6 Δx= 100 km, Δy=115 km				
2	8×10^8	10^7	20	0.5	0
3	8×10^8	10^7	20	0.5	2×10^9
4	-10^{23}	-10^{21}	20	0.5	0
5	8×10^8	10^7	20	0.5	0
	$(C_M = 10)$	$(C_H = 0.1)$			

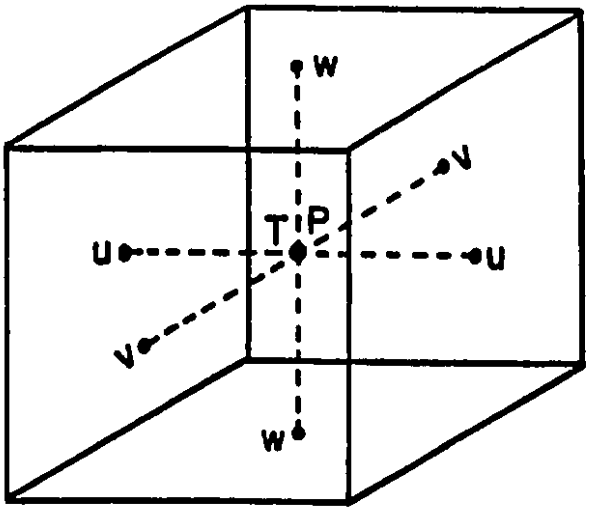

Figure 2.1: The grid structure of the C-grid, showing the position of the velocity (u,v,w), pressure (p) and temperature (T) points.

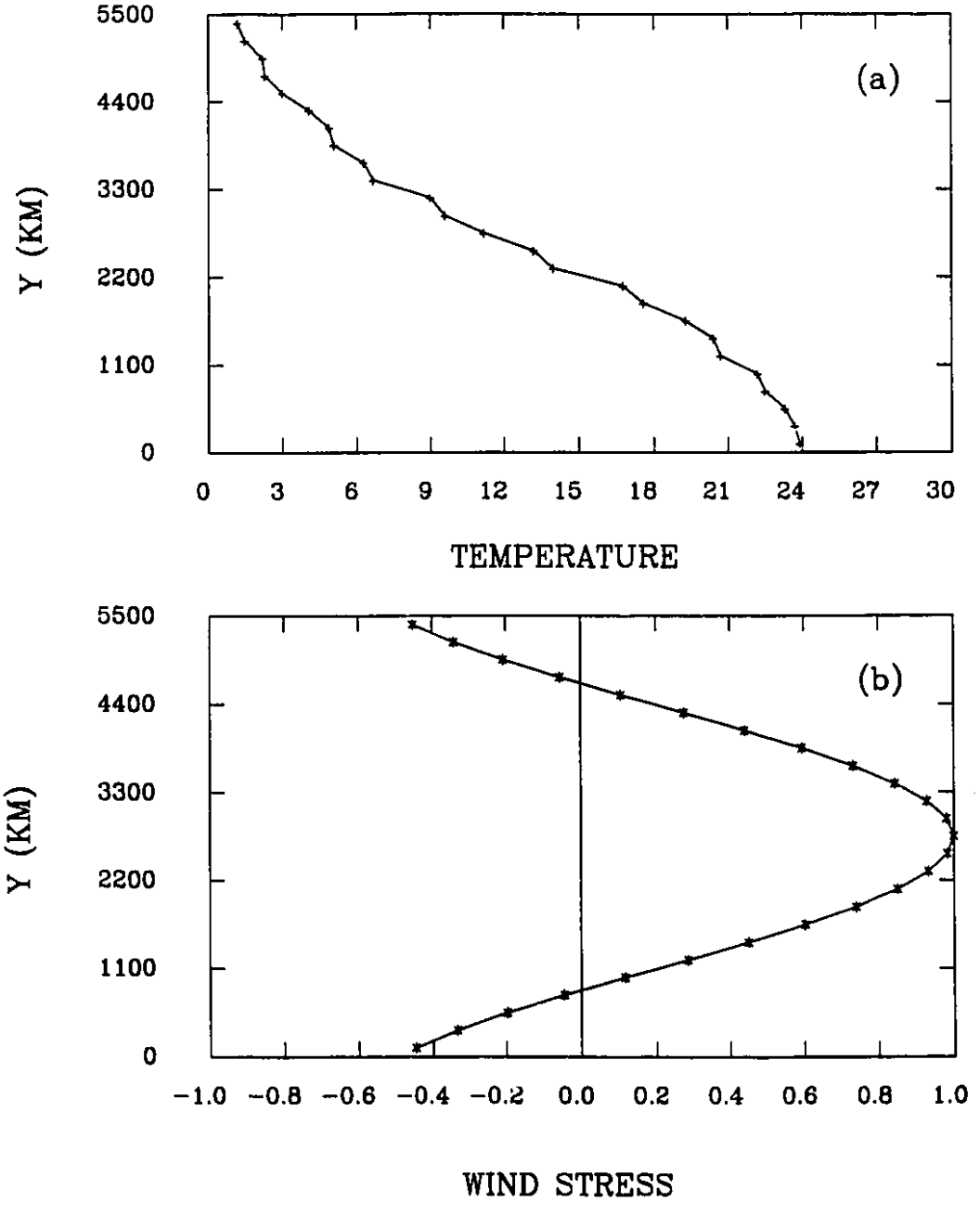

Figure 2.2: The latitudinal distribution of the (a) apparent atmospheric temperature (°C), and (b) zonal wind stress (dyne cm^{-2}), used as surface forcings. There is no variation with longitude.

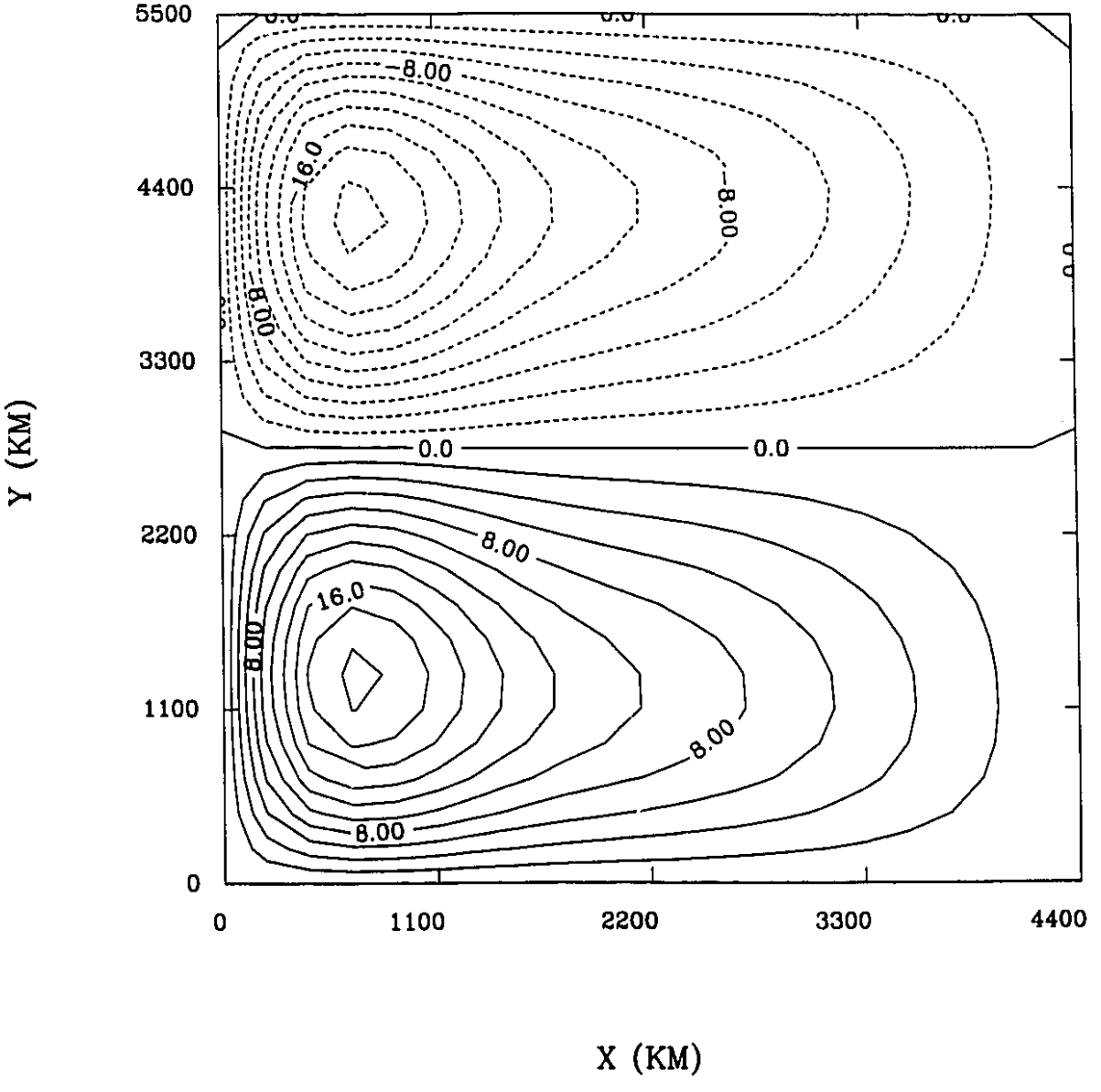

Figure 2.3: The barotropic streamfunction (Sv) as a function of the zonal and meridional coordinates.

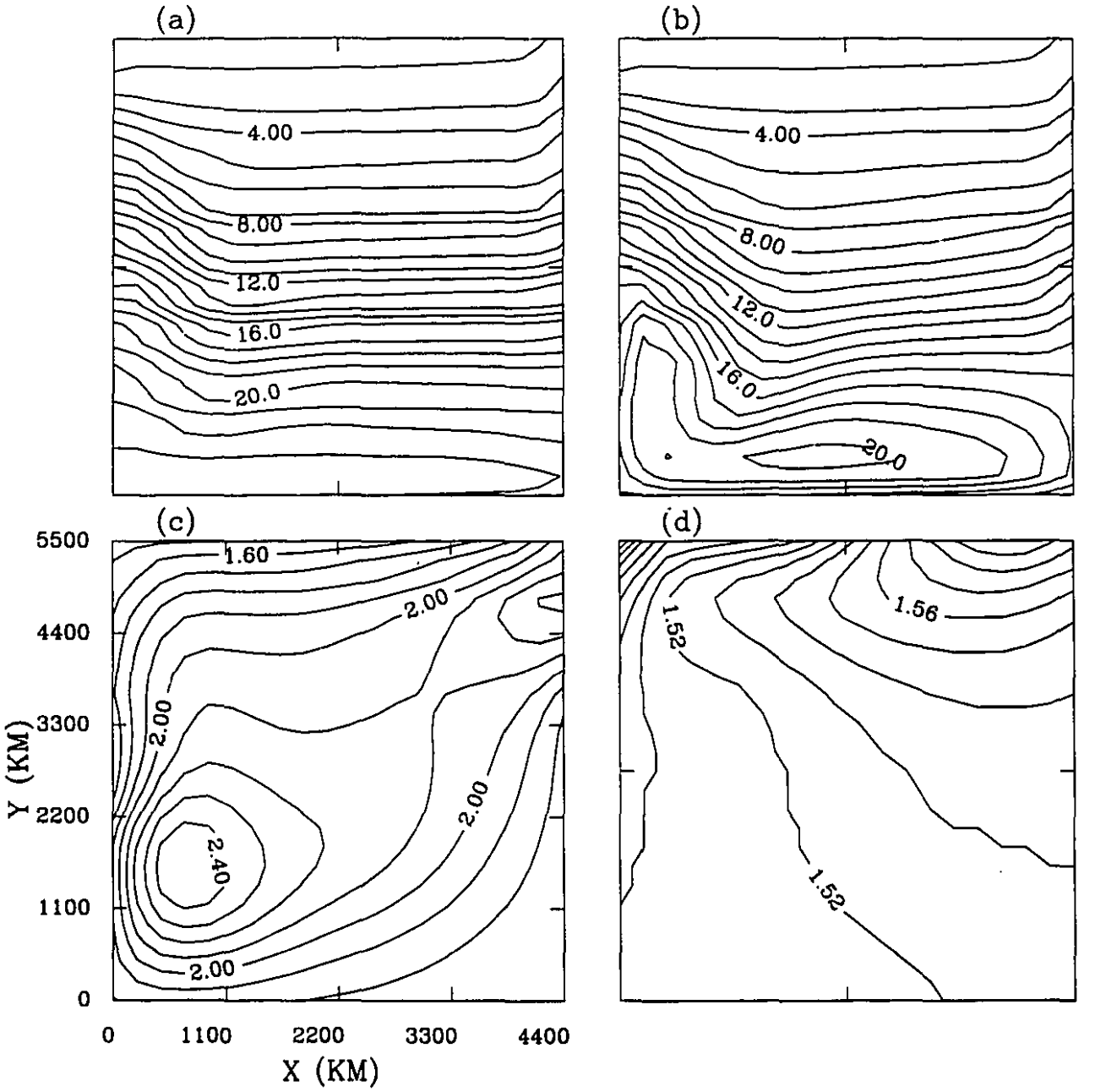

Figure 2.4: The horizontal temperature distribution (°C) at different levels: (a) 25 m (contour interval= 1); (b) 75 m (C.I.= 1); (c) 850 m (C.I.= 0.1); (d) 2800 m (C.I.= 0.01).

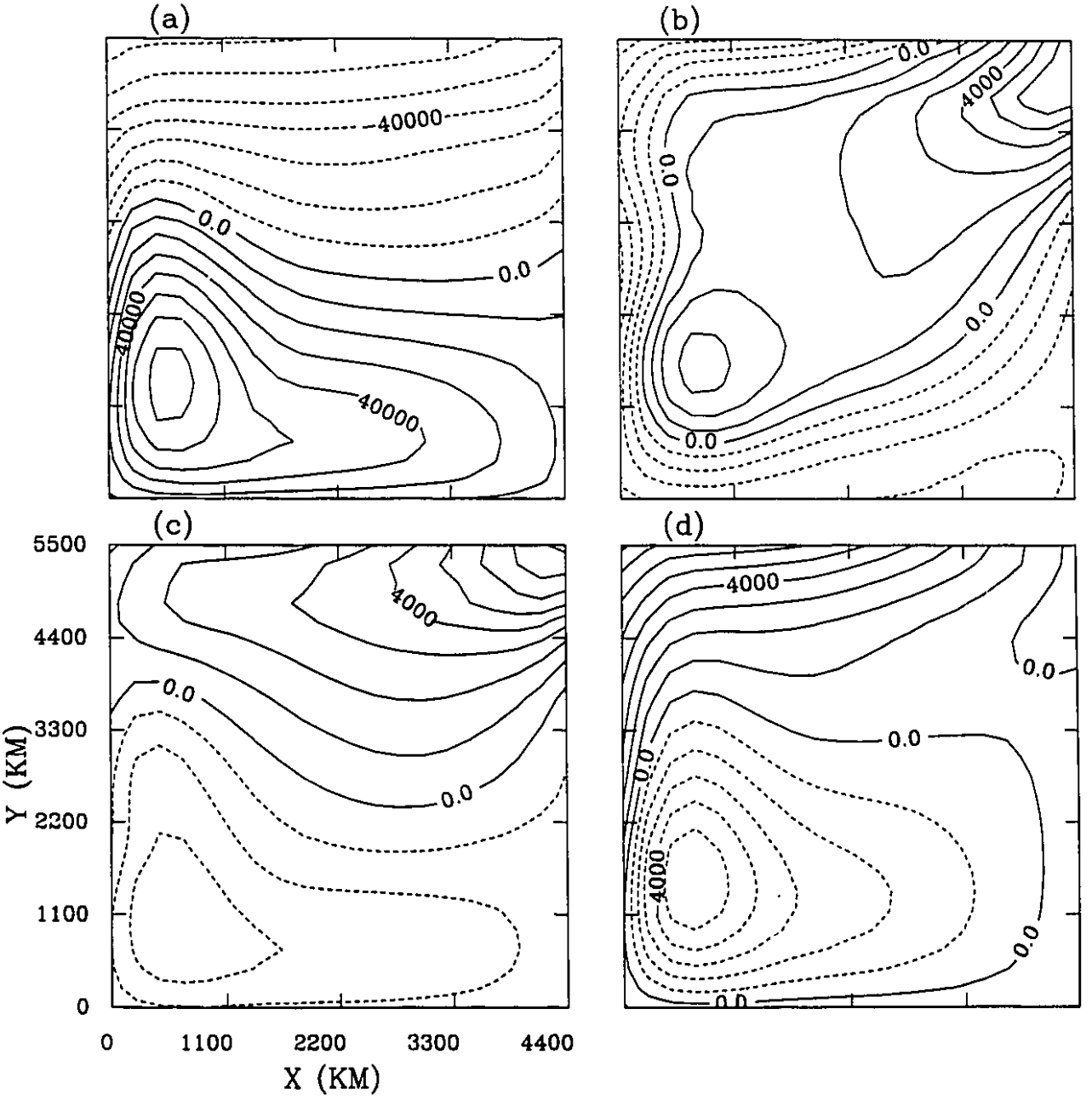

Figure 2.5: The horizontal distribution of baroclinic pressure (dyne cm^{-2}) at different levels: (a) 25 m; (b) 75 m; (c) 850 m; (d) 2800 m.

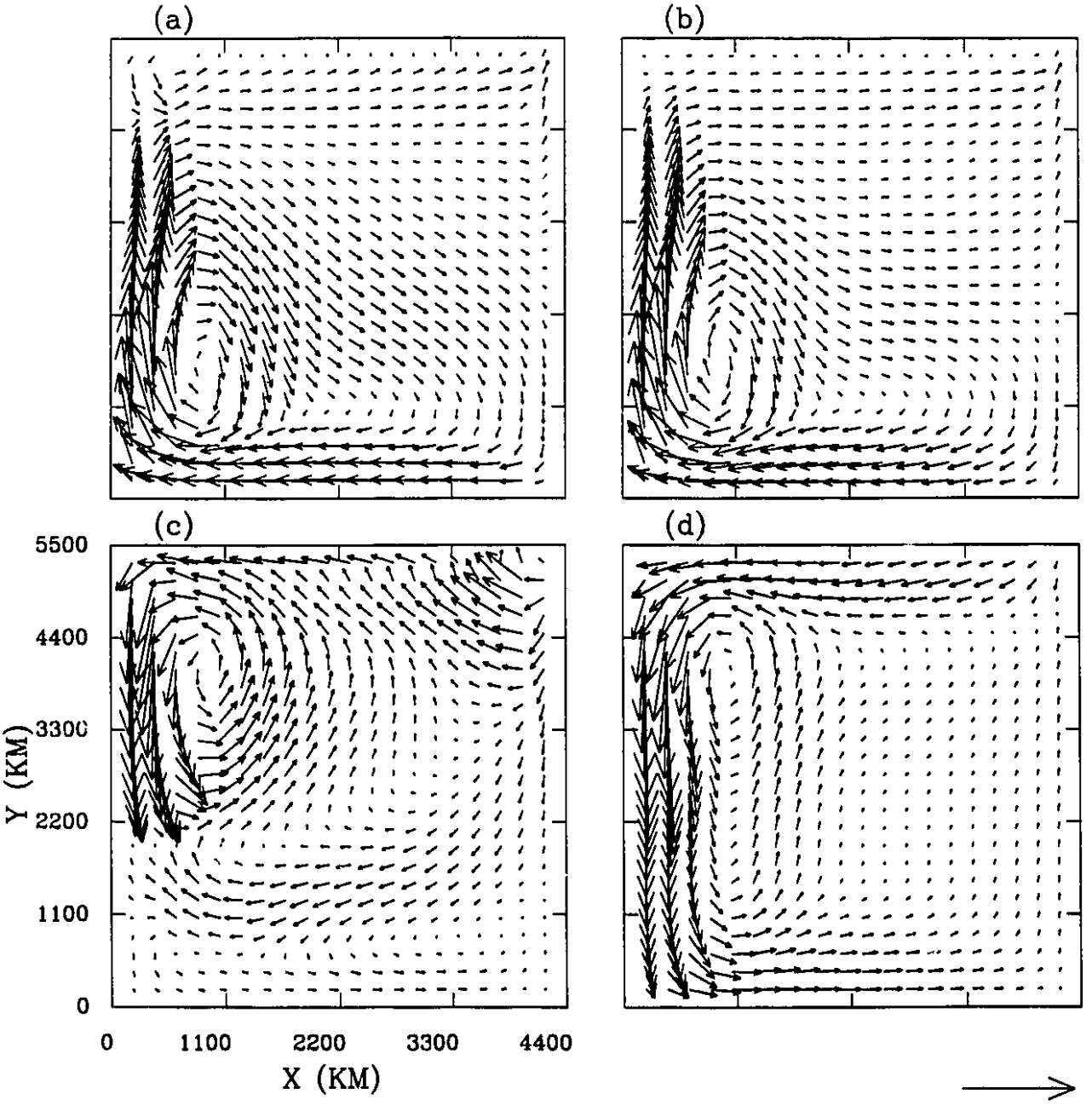

Figure 2.6: The distribution of horizontal velocities (cm s^{-1}) at different levels. The magnitudes corresponding to the vector shown at the bottom right are different for each level, and is given between parentheses: (a) 25 m (29); (b) 75 m (27); (c) 850 m (1.48); (d) 2800 m (2.25).

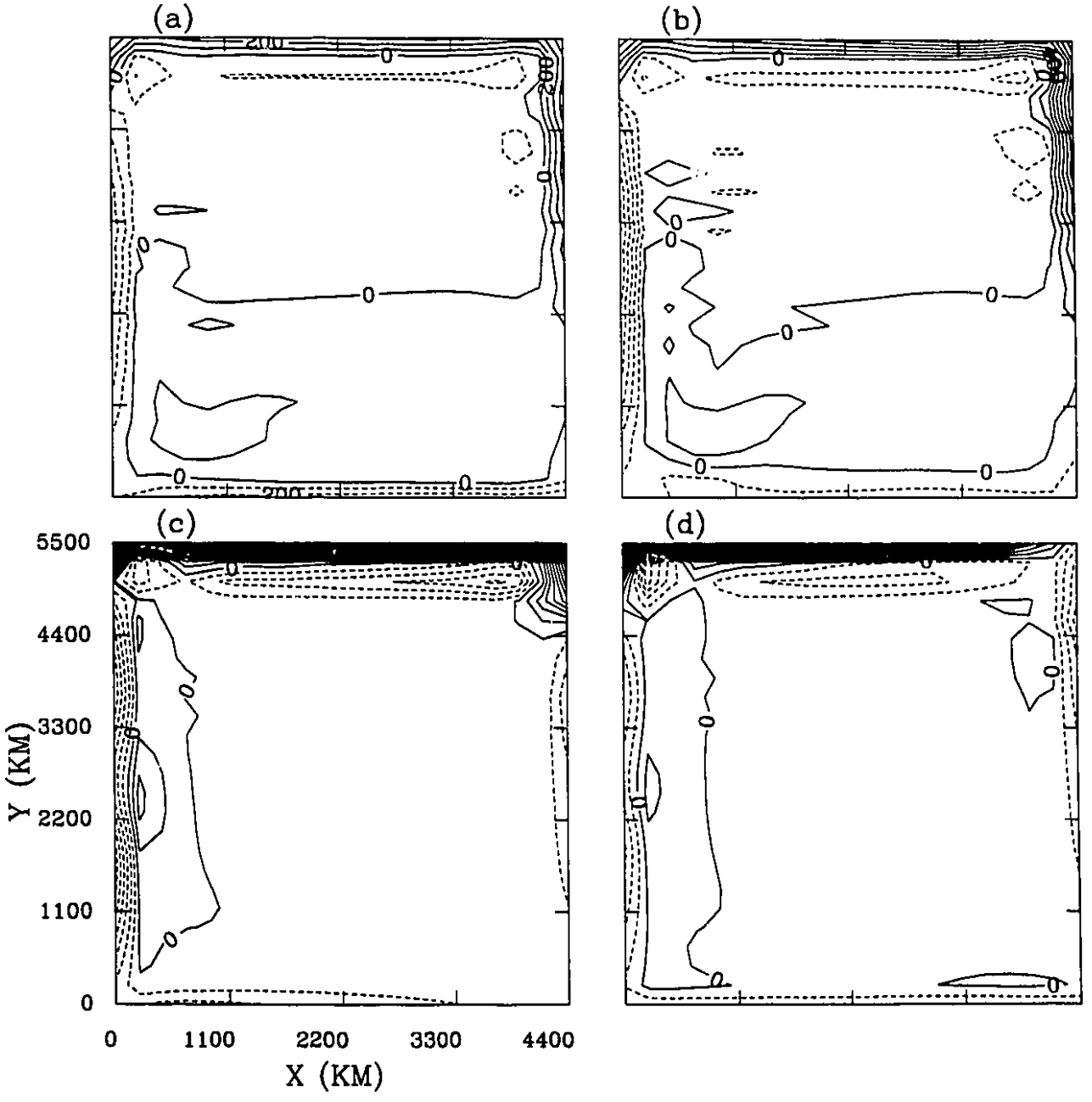

Figure 2.7: The horizontal distribution of vertical velocities (cm s^{-1}, C.I.= 10^{-4}) at different levels: (a) 25 m; (b) 75 m; (c) 850 m; (d) 2800 m. The dashed (solid) lines indicate upward (downward) vertical velocity.

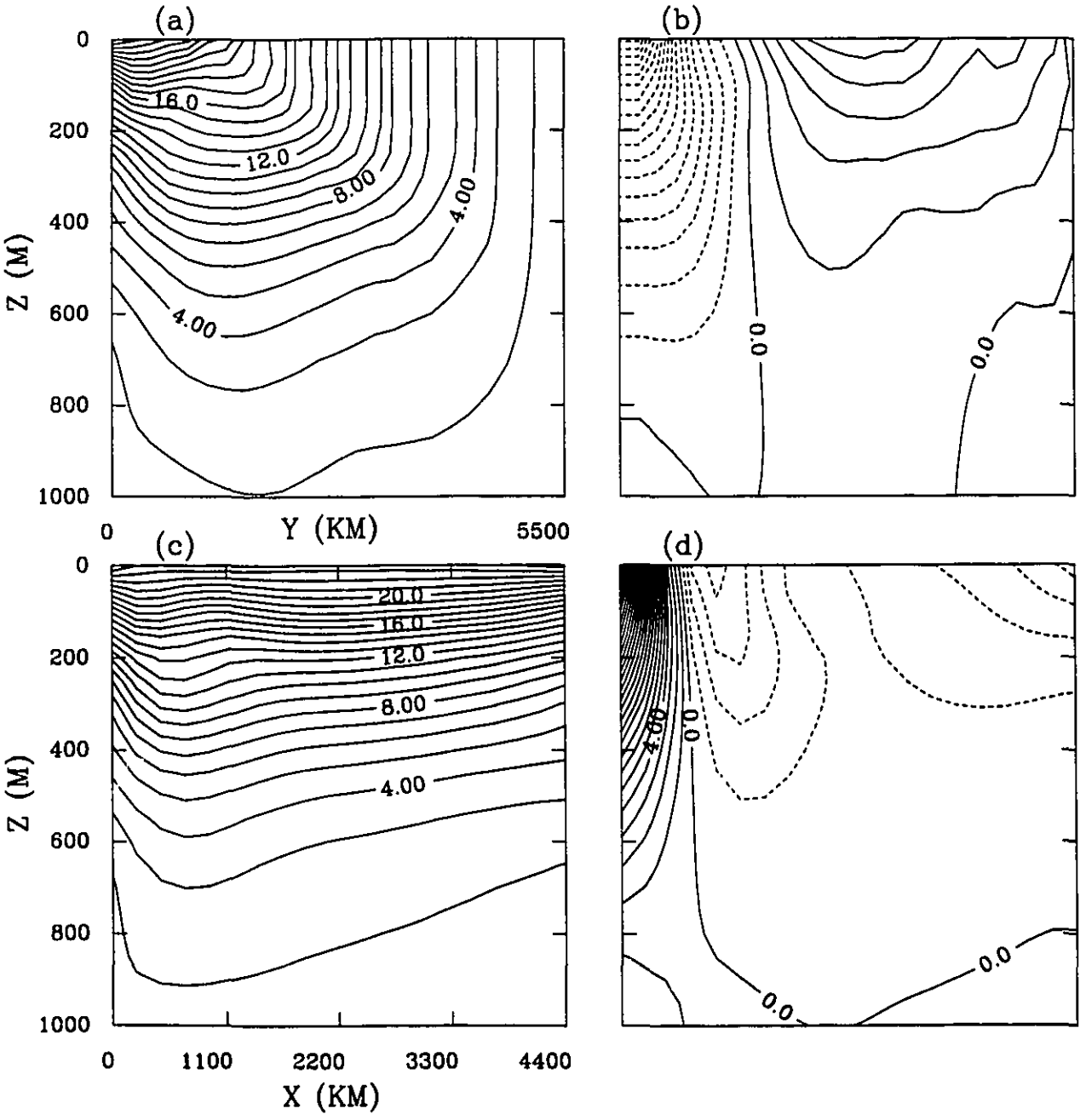

Figure 2.8: Meridional sections of (a) temperature (°C) and (b) zonal velocity (cm s^{-1}) along a cross section 1100 km away from the western boundary. Zonal sections of (c) temperature (°C) and (d) meridional velocity (cm s^{-1}) along a vertical cross section 1100 km away from the southern boundary.

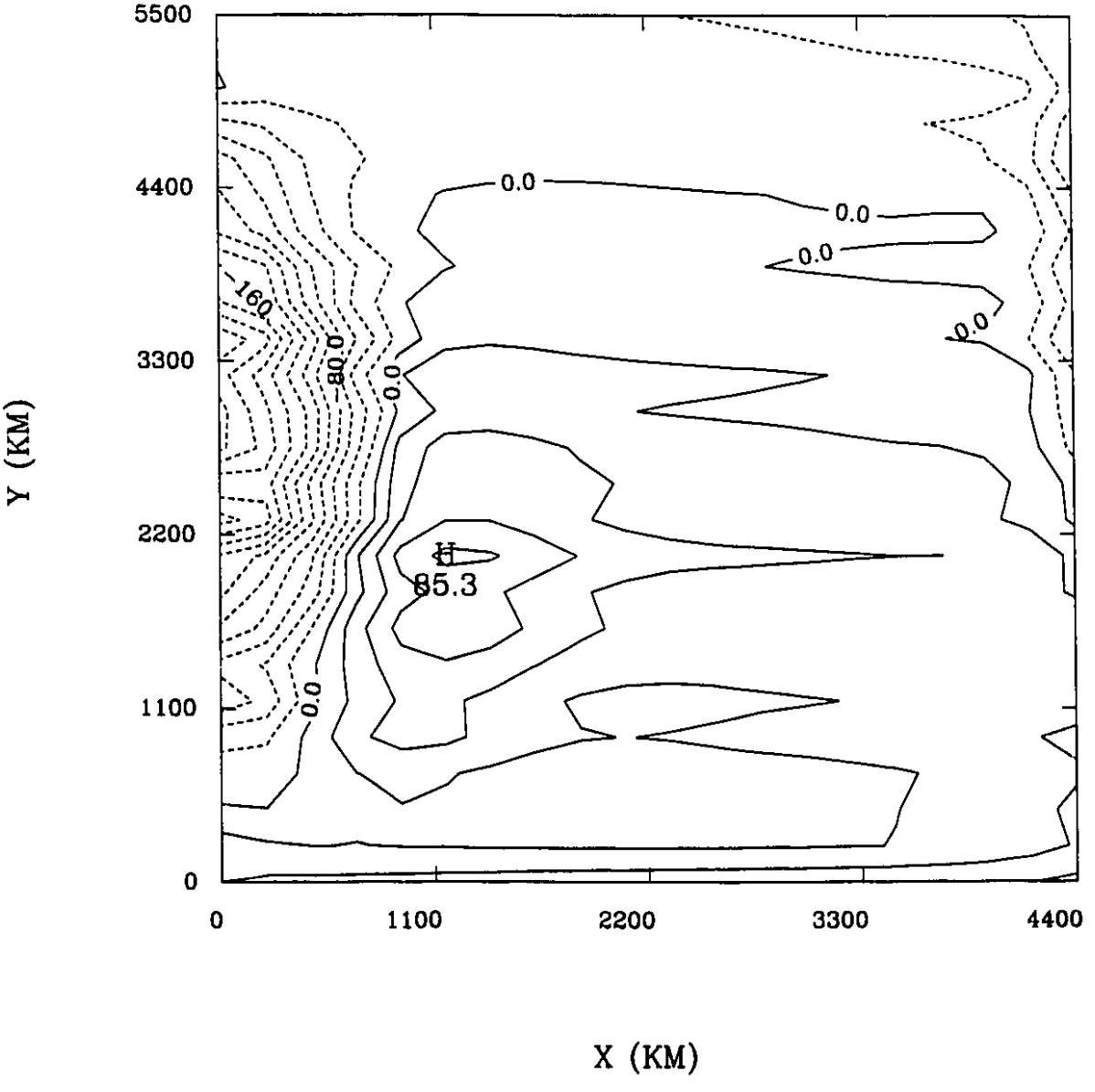

Figure 2.9: The surface heat fluxes (W m^{-2}), with negative values indicating a flux from the ocean to the atmosphere.

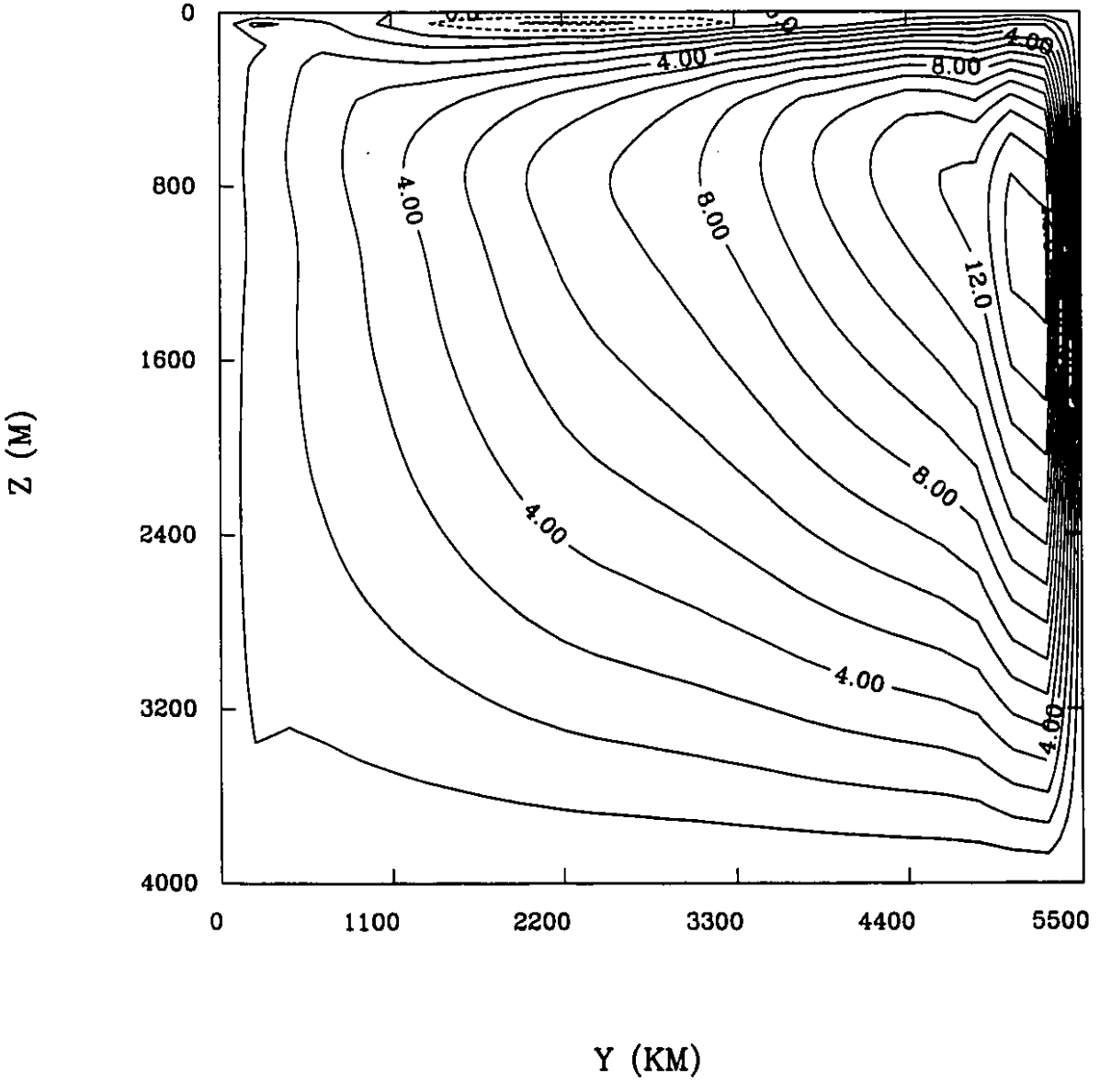

Figure 2.10: The mean meridional circulation, i.e., the thermohaline circulation (Sv), with dashed lines indicating anticyclonic circulation, and solid lines indicating cyclonic circulation.

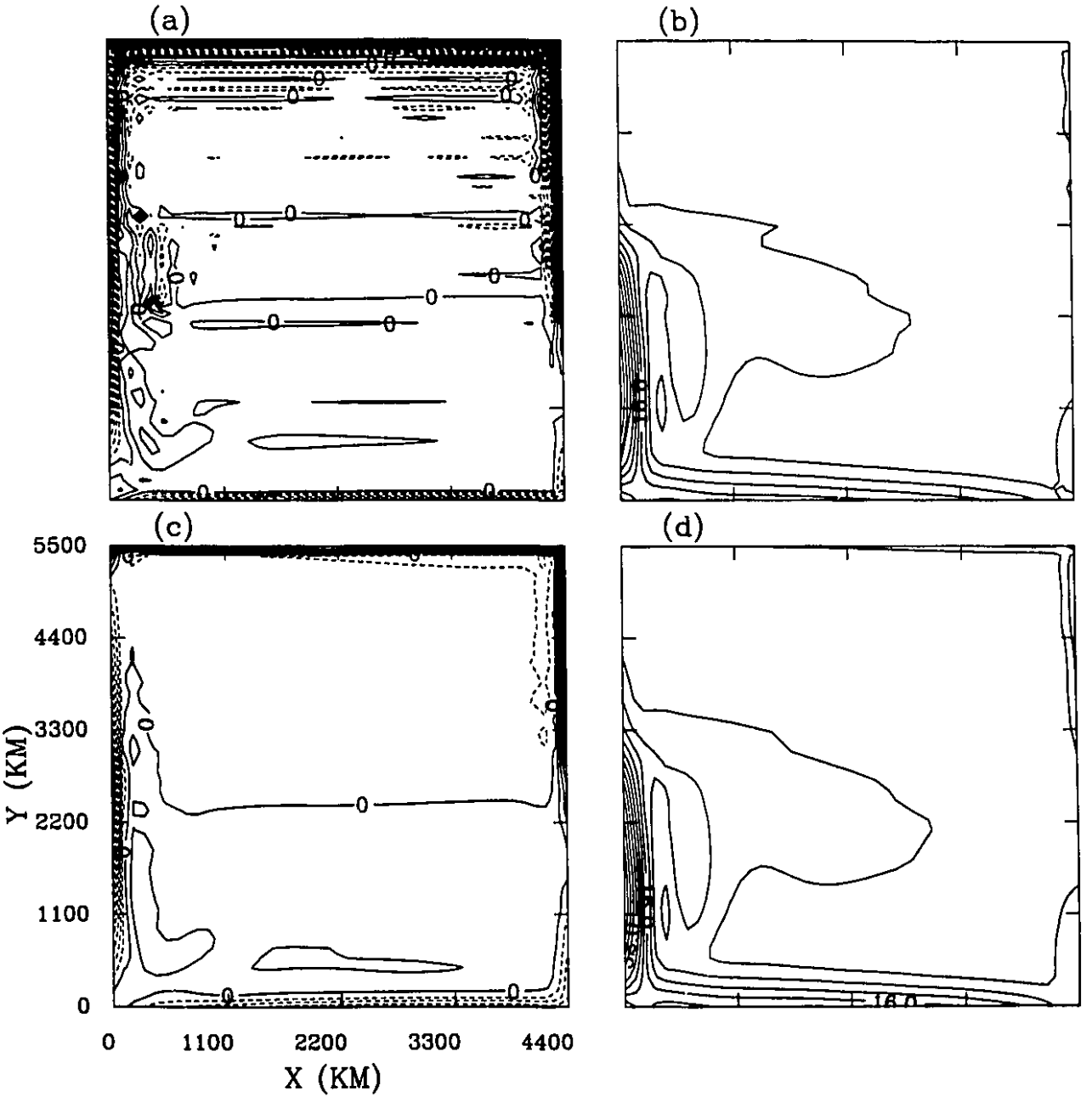

Figure 2.11: The horizontal distribution of (a) the vertical velocity (cm s^{-1}, C.I.= 10^{-4}) at the bottom of the first layer, and (b) the root-mean-square horizontal velocity (cm s^{-1}, C.I.= 4) of the first layer for Case 2. (c), (d) are similar to (a), (b) respectively, but for Case 3.

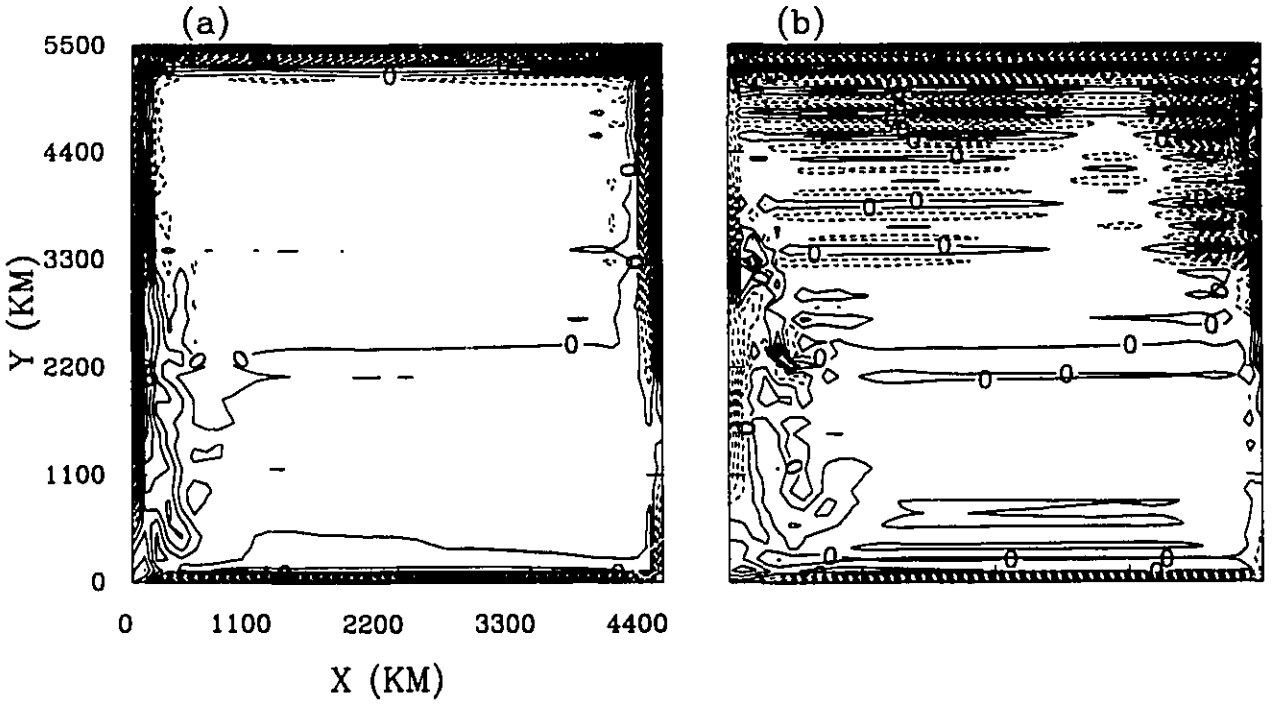

Figure 2.12: The horizontal distribution of the vertical velocity (cm s^{-1}, C.I.= 10^{-4}) at the bottom of the first layer for (a) Case 4; (b) Case 5.

Chapter 3

Effects of Lateral Boundary Conditions

3.1 Introduction

The effects of lateral boundary conditions in ocean circulation models have been studied using barotropic models or quasi-geostrophic (QG) models. Blandford (1971) showed using a wind-driven homogeneous ocean model with constant depth, that a steady flow with western, northern, and eastern boundary currents with free slip (FRS) condition changed to an unsteady flow with a western boundary layer and eddies in the northwest corner of the model domain for no slip (NOS) condition, if the Reynolds number is large enough. Dengg (1993) investigated the inertial separation of the western boundary current (WBC) from an idealized continent in a barotropic model, and found that the WBC can separate from the coast only if the NOS condition is used.

Marshall and Marshall (1992) showed that NOS condition tends to produce a recirculation gyre and weaker eastward free jet than FRS condition in a QG model. Haidvogel et al. (1992) showed, using a QG model, that both the mean and eddy kinetic decrease and the WBC has a premature separation when the boundary condition is changed from FRS to NOS.

Both QG and barotropic models have dynamic and thermodynamic limitations compared to primitive equation (PE) models and cannot be used to examine the thermohaline circulation and northward heat transport. It is thus a natural extension to examine the effects of different boundary conditions in PE models with both wind and thermal forcings. This may help in formulating realistic boundary conditions for PE models. Holland and Lin (1975b) examined the effect of lateral boundary conditions in an adiabatic, two-layer, single gyre wind-driven PE model and found that the flow reaches a steady state with the NOS condition. In multi-level PE models with both wind and thermal forcing, both choices of FRS or NOS conditions have been used. Han (1975) and Robinson et al (1977) used FRS condition and obtained weak instabilities. By including topography, Semtner and Mintz (1977) obtained much stronger baroclinic production of eddy kinetic energy and a more realistic Gulf Stream compared to the earlier study of Han(1975); the latter had no topography. Cox (1985) applied Bryan's (1969) PE model to a basin scale domain of the North Atlantic with NOS condition. This simulation showed flow features as suggested by recent theories of ocean circulation (Rhines and Young, 1982; Luyten et al., 1983). Cox's (1985) study was extended to include random topography (Boning, 1989) and higher horizontal resolution (Boning and Budich, 1992). The NOS condition was also used by Bryan and Holland (1989), Boning et al. (1991), Semtner and Chervin (1988, 1992).

We thus note that Han (1975) and Robinson et al. (1977) simulated a low level of eddy activity with little instabilities using PE models with a flat bottom ocean and FRS conditions. On the other hand Cox (1985) obtained significant eddy activity using a PE model of an idealized North Atlantic Ocean with NOS condition. As mentioned earlier, we examine here the effects of FRS and NOS conditions in a PE model with both wind and thermal forcings.

The NOS condition is based on the observed behaviour of almost all real fluids, and is a consequence of the molecular nature of fluid and the interactions with a solid boundary. The tangential velocity decreases to zero at the boundary in a thin

layer. It might be possible to find a solution for the interior region of the flow which does not satisfy the NOS condition, and a "boundary-layer solution" which matches the interior solution. To obtain the interior solution only, FRS condition can be used, as this means the effects of the boundary do not penetrate into the interior. In numerical ocean circulation models, it is impossible to resolve the molecular boundary layer near solid walls. The correct boundary condition is thus not known. Haidvogel et al. (1992) suggested that a partial slip boundary condition, which is somewhere between free slip and no slip boundary conditions, should be used based on a QG model study.

The organization of this Chapter is as follows: Section 2 decribes the model and the design of experiments. Section 3 describes the basic results of the eddy resolving model using NOS and FRS boundary conditions. Section 4 examines the mean and eddy kinetic and available potential energies and the conversions between them. Section 5 investigates the northward heat transport and the contributions from different components. The sensitivities of eddy energetics and heat transport to vertical resolution is also briefly discussed. Section 6 presents the summary and conclusions.

3.2 Model and experiments

In this Chapter, we use the same model as described in Chapter 2 to examine the effects of lateral boundary conditions in the eddy resolving regime. The semi-implicit scheme is not needed at fine resolution with explicitly resolved eddies. The divergence dissipation is only used in the subpolar gyre to obtain a smooth field where the Rossby radius of deformation is very small (less than 40 km) due to the weak stratification and large Coriolis coefficient. For eddy resolving models with 40 km horizontal resolution, the main resolved motion is still quasi-geostrophic with the divergence being of secondary importance. We thus expect this frictional parameterization to operate in a similar manner as at coarse resolution. Indeed, a similar dissipation of divergence has been successfully used in atmospheric mesoscale studies (Hadley and Yau, 1988)

and ocean convection studies (Brugge et al., 1991; Jones and Marshall, 1993).

The horizontal extent of the rectangular domain is 4000 km and 4800 km in the zonal and meridional directions respectively, centered at 40°N, which is similar to that of the North Atlantic. The depth is 4 km, same as in Chapter 2. The horizontal domain has been reduced from that of Chapter 2 to reduce computational requirement.

The lateral boundary conditions are the same as those in Chapter 2, except both NOS and FRS conditions are used here. As mentioned already, the goal is to examine the effects of these boundary conditions in a PE model with both wind and thermal forcings. A physical interpretation of the NOS and FRS boundary conditions is shown in Figure 3.1. We take the axis of the western boundary current to be the region of maximum velocity. The NOS condition produces a positive vorticity source, which may cause the WBC to separate through positive vorticity advection or diffusion to midlatitudes. We note that the positive vorticity advection can also be provided by the southward flowing branch of the subpolar gyre. This condition also introduces strong horizontal current shear near the western boundary, which can generate barotropic instability. Both effects are absent with the FRS boundary condition.

Figure 3.2 shows the latitudinal distributions of the apparent atmospheric temperature and zonal wind stress, which are used as the surface forcing in the top model layer. The wind stress can be expressed as $\tau^x = 0.25 + 0.75cos((Y - Y_0)\pi/Y_0)$, where Y is between 0 and 4800 km, and Y_0=2400 km.

Figure 3.3 describes the experimental procedure for the NOS and FRS integrations. The number of vertical levels was doubled to examine the effects of increased vertical resolution. Table 3.1 shows the vertical discretization of the model for the low and high vertical resolution cases. Table 3.2 presents the dissipative parameters used in the coarse and fine resolution experiments.

We have used both the NOS and FRS boundary conditions at coarse resolution. The results are quite similar, except that smaller velocities are found in the NOS

experiments compared to the FRS experiments, for the same horizontal diffusivities. Killworth (1985) found that the use of NOS or FRS boundary conditions has little effect on the results at coarse resolution.

For both FRS and NOS eddy resolving experiments, we first used the results from the FRS coarse resolution experiment as initial conditions (Figure 3.3). Little eddy activity was found for a wide range of diffusivities and viscosities with FRS conditions (Further reduction of the latter coefficients does not increase the eddy activity by much, and the solutions become more unrealistic at the same time; for example, the western boundary current overshoots too far north with more noise). We then perform the NOS eddy simulation until statistical steady state is reached after 20 years of integration, using the pressure and temperature fields from the FRS eddy resolving experiment as the initial condition of the NOS experiment, with a motionless initial state.

Our 40 km horizontal resolution can only resolve the first baroclinic mode in the subtropical ocean (Emery et al., 1984). A similar resolution has been used by others in the eddy regime (e.g., Semtner and Mintz, 1977; Cox, 1985; Boning, 1989; Bryan and Holland, 1989; Semtner and Chervin, 1988, 1992). It is of interest to examine the effects of boundary conditions on PE models in the nonlinear regime, even without completely resolving eddies.

We describe several dimensionless parameters to characterize parameter space. Let L be a characteristic horizontal space scale, and U a horizontal velocity scale. The Rossby (R_0), Reynolds (R_e) and Peclet (P_e) numbers are given below, based on the Laplacian frictional parameterization, and a value of the Coriolis parameter f_0 at midlatitudes. The relation of the coefficients of Laplacian eddy diffusion to those of biharmonic diffusion has been given in Equation (2.24).

$$\begin{aligned} R_0 &= U/f_0 L \\ R_e &= UL/A_{MH} \\ P_e &= UL/A_{HH} \end{aligned}$$

Table 3.3 shows typical values of the length and velocity scales and values of R_0,

R_e and P_e. The Rossby number remains small compared to unity in both the coarse and fine resolution results, so the interior ocean is still quasi-geostrophic. The fine resolution results have Reynolds numbers about 1000 times larger than those of coarse resolution, indicating a more nonlinear flow.

3.3 Horizontal and vertical flow structure

We now compare the results of the flow structure simulated using the NOS and FRS boundary conditions, corresponding to Cases 3-4 of Table 3.2. As the FRS coarse resolution model results (Case 2) have been discussed extensively in Chapter 2, we focus mainly on the eddy resolving results in all the subsequent discussion unless otherwise stated. All the time averaged fields were calculated over a 5-year period.

Figure 3.4 shows the equivalent surface topography using coarse and fine resolution, with both NOS and FRS boundary conditions (Cases 1-4). In subsequent plots, comparison of the two conditions have the NOS results as left panels, and FRS results as right panels. The results of the coarse resolution models (Figures 3.4(a), (b)) are quite similar. At fine resolution, the wind stress generates two gyres with concentrated outflow near midlatitudes (Figures 3.4(c), (d)). There is a recirculation near the western boundary of the subtropical gyres. The net circulation is more concentrated near the western boundary and midlatitudes in the fine resolution cases, resulting in stronger western boundary and North Atlantic currents. An obvious difference between the NOS and FRS cases is a significant overshooting of the western boundary current in the latter.

Figure 3.5 shows the horizontal distribution of the top layer eddy kinetic energy (K'), which corresponds to the time varying component of the flow over the averaging period. The definitions of the various forms of eddy energy are shown in Appendix C. Two regions of enhanced variability can be identified. The largest eddy activity is associated with the western boundary current and its separation region, a smaller secondary maximum of K' is located near the North Equatorial current, with very

weak energies in the eastern subtropical gyre. The general pattern of K' is similar to that of Cox's (1985), and Boning and Budich's (1992) B-grid model with NOS conditions. For the NOS case (Figure 3.5(a)), the maximum level of K' is larger than that of Cox (1985). This is due to our use of the C-grid, with meridional velocity points located half a grid away from the western wall. This results in stronger boundary current shear and more barotropic instability. Indeed, by doubling the horizontal resolution, Boning and Budich obtained a stronger K' maximum of more than 2000 $cm^2\ s^{-2}$. The region of strong K' extends farther eastward in Cox's and Boning and Budich's results; this may be due to the absence of shelf topography (Semtner and Mintz, 1977) and the weaker wind stress used in our study. The K' level is much smaller than that observed along the North Atlantic current (Wyrtki et al., 1976; Richardson, 1983; Le Traon et al., 1990), a common difficulty with eddy resolving PE models (Cox, 1985; Boning, 1989; Bryan and Holland, 1989; Boning and Budich, 1992; Treguier, 1992). This may in part be due to the insufficient spatial resolution of the mesoscale band in the models. This suggests that an even higher horizontal resolution than that used here, with correspondingly reduced horizontal diffusivities, is needed to better reproduce K' and P' levels (Boning and Budich, 1992; Stammer and Boning, 1992; Treguier, 1992). Topography and seasonal variability may also have important effects; they are not included in this study.

The results for FRS boundary conditions (Figure 3.5(b)) are quite different from those of NOS conditions. The maximum level of K' in the western boundary region is only 400 $cm^2\ s^{-2}$ for the former compared to 2000 $cm^2\ s^{-2}$ for the latter. The use of NOS conditions creates larger horizontal shears near the western wall, as the velocity is forced to vanish at the wall.

We next examine the latitude/depth distribution of the zonally averaged K' and P' fields (Figure 3.6). There are two K' maxima (Figures 3.6(a), (b)), corresponding to the midlatitude jet and the North Equatorial current. The former much exceeds the latter for the NOS case, but they are of comparable magnitudes for the FRS case. The K' distribution decreases with depth. The P' distributions (Figure 3.6(c),

(d)) shows more structure on the vertical plane. There are maxima centers associated with thermoclines. The maximum magnitudes of about 5000 $cm^2\ s^{-2}$ near the western boundary layer (figures not shown) for P', corresponding to a temperature variance of about 6 $°C^2$, are quite comparable to those found in the coarse resolution (0.33° × 0.4°) experiments of Boning and Budich (1992). In contrast to K', the maxima of P' are found at subsurface levels. Both K' and P' are stronger for the NOS case than the FRS case. This indicates that the larger K' due to the stronger barotropic instability in the NOS case induces larger P'. This may in turn generate stronger baroclinic instability, as we shall see later.

Figure 3.7 shows the instantaneous and time mean top layer flows for NOS and FRS boundary conditions. The strongest mean currents are found near the southern boundary corresponding to the North Equatorial current, and at the western boundary. In the NOS case, eddy activity is strongest near the midlatitude jet, in agreement with the results of Figure 3.5. There is also a signature of the thermohaline circulation driven by the prescribed surface thermal forcing, resulting in a northward flow along the subpolar extent of the western boundary. The results are different for the FRS case. The eddy activity is much weaker, and the western boundary current overshoots in both the instantaneous and time mean flows. Results from perturbation analysis (Munk et al., 1956) and inertial models (Charney, 1955; Morgan, 1956) show that a western boundary current can extend beyond the latitude of the zero wind stress curl. Blandford (1971) showed that the use of lateral boundary conditions is important in determining the separation and stability of the western boundary current in barotropic models. Dengg (1993) investigated the inertial separation of WBC from an idealized continent in a barotropic model and found similar conclusions. Our PE model results with both wind and thermal forcings also show that boundary conditions are important in determining the latitude of separation of the western boundary current. The excess inertia of the fluid particles in FRS models causes the current to overshoot their original interior latitudes. There must thus be a region where inertial

processes and friction restore the particles southward to their starting points. The effect is to spread the region of inertial and frictional control northward and eventually eastward, starting from the northwest corner of the basin.

Further examination of the horizontal eddy structure (figures not shown) for both the NOS and FRS cases shows that the scale of the eddies are smaller in the subpolar latitudes compared to the subtropical latitudes, due to the reduced Rossby radius of deformation at higher latitudes (Stammer and Boning, 1992).

Figure 3.8 shows the time mean temperature field and the deviation from the time mean, for the NOS and FRS cases. The largest temperature deviations are found near the western (Figures 3.8(c), (d)) and southern boundaries (figures not shown), consistent with our earlier results that eddies are concentrated in these regions (Figures 3.5 and 3.6). In the midlatitude interior of the NOS case, there is also significant deviation associated with midlatitude eddies. However, these signatures are generally much weaker in FRS than in NOS conditions. A comparison of the time mean fields reveals the overshooting of the western boundary current in the FRS case.

Figure 3.9 shows the instantaneous thermocline structure along the western boundary as well as its zonal mean, for the NOS and FRS cases. There is clear evidence of eddies in the section along the western boundary in both cases, but the eddies are shifted further north in the FRS case due to the overshooting western boundary current. In both cases, the eddy signature is smoothed out in the zonal mean thermocline.

3.4 Eddy energetics

In this section, we continue the comparison of results obtained with the NOS and FRS boundary conditions, focusing on the eddy energetics. In Appendix C, we show the definitions of the mean ($\overline{P}$) and eddy (P') available potential energy, mean ($\overline{K}$) and eddy (K') kinetic energy. The corresponding conversion terms are also defined there: ($\overline{P}$, $\overline{K}$), ($\overline{P}$, P'), (P', K') and ($\overline{K}$, K'). The formulation is standard and

follows that of Boning and Budich (1992).

Figure 3.10 shows the 4-box Lorenz energy diagram for the entire basin, for NOS (Case 3), FRS (Case 4). The mean energies $\overline{P}$, $\overline{K}$ and the conversion between them ($\overline{P}$, $\overline{K}$) are comparable in all cases. The surface thermal forcing generates $\overline{P}$, which is then converted to $\overline{K}$ through the sinking of cold water and the rising of warm water at different latitudes. The direction of this conversion is determined by the relative importance of buoyancy forcing and wind stress (Bryan, 1986). In our experiments, thermal forcing is more important and results in a conversion of $\overline{P}$ to $\overline{K}$. The eddy energies P' and K' are much larger for the NOS case, consistent with the results of Section 3.3. For this case, K' is maintained by both baroclinic and barotropic instabilities. The magnitude of the basin mean K' is comparable to that of Boning and Budich's (1992) with a resolution of $0.33^o \times 0.4^o$. The baroclinic conversion (P', K') is comparable to the barotropic conversion ($\overline{K}$, K') for the NOS case. For the FRS case, the baroclinic conversion is dominant; the small ($\overline{K}$, K') conversion is in fact negligible. The mean kinetic energy $\overline{K}$ is almost a factor of two larger for FRS compared to NOS conditions, due to the smaller eddy dissipation in the former.

Haidvogel et al. (1992) investigated the effect of different boundary conditions in QG models, and found that both mean and eddy kinetic energy decrease when the lateral boundary conditions were changed from FRS to NOS. However, NOS is the commonly used boundary condition in PE models, and strong eddy kinetic energies are obtained, as we have shown here. The reason is because the eddy kinetic energy is mainly produced by the midlatitude free jet in QG models, which was effectively weakened by premature separation of western boundary currents in both subtropic and subpolar gyres if NOS condition is used. In the PE models, there is asymmetry between subtropic and subpolar gyres due to more complicated physics (McWilliams et al., 1990) and the northward thermohaline component of the western boundary current (Cox, 1985).

We next examine the distributions of vertically averaged mean kinetic energy, eddy kinetic energy, barotropic instability and baroclinic instability for five sub-domains

which are important regions of eddy activity. We average over each sub-domain as the point values of barotropic and baroclinic instability are noisy (Treguier, 1992). The boundaries of these regions are shown in Figure 3.11. The five sub-domains correspond to the north (R1) and south (R2) of the midlatitude free jet, outflow region (R3), western boundary current (R4) and the North Equatorial Current (R5).

We first discuss the five sub-regions obtained with NOS conditions (Table 3.4). North of the midlatitude free jet (R1), there is weak baroclinic instability. The barotropic conversion shows that eddy viscosity actually maintains the mean flow through momentum flux convergence. This has been found in the fine resolution study by Boning and Budich (1992), and is also consistent with observations of the Gulf Stream and Kuroshio extensions (Schmitz, 1977, 1982; Hishida and White, 1982; Tai and White, 1990). There is weak barotropic instability south of the midlatitude free jet (R2). The baroclinic conversion is negative, indicating some eddies are reabsorbed into the mean flow (Semtner and Mintz, 1977; Treguier, 1992).

Turning to the outflow region (R3), we see that the barotropic ($\overline{K}$, K') and baroclinic conversions (P', K') are much stronger than in the R1 and R2 regions. As noted earlier, this is because the NOS condition creates a strong horizontal current shear which produces stronger barotropic instability. This in turn produces enhanced temperature correlations, which is a source of baroclinic instability. Note that both mean and eddy kinetic energies are much larger than in the R1 and R2 regions.

In the western boundary current region (R4), $\overline{K}$ is larger, but K' is smaller than those in the outflow region (R3). The barotropic and baroclinic conversions (P', K') and ($\overline{K}$, K') are comparable to each other, but both are smaller than in R3. Near the North Equatorial Current at the southern boundary, the unstable mechanism is mainly baroclinic instability (R5). The barotropic conversion ($\overline{K}$, K') is small and negative, indicating a weak conversion from K' to $\overline{K}$.

In summary, our results for the NOS case show that a mixed barotropic and baroclinic instability is important in the western boundary current and outflow regions. In the free jet north (Gulf Stream extension or R1) and North Equatorial current

regions, there is modest baroclinic instability, with almost no signature of barotropic instability or negative eddy viscosity.

We now turn to the results obtained with FRS boundary conditions. The eddy (mean) kinetic energy levels in the free jet region (R1 and R2) are smaller (larger) than those obtained with NOS conditions. The barotropic and baroclinic conversions are very weak, as for NOS. Therefore the eddy energy transport is important in maintaining the stronger eddy kinetic energy of the NOS case. The weak barotropic and baroclinic instabilities in both the NOS and FRS cases are due to low horizontal resolutions (Barnier et al., 1991; Boning and Budich, 1992; Treguier, 1992). The increase in the mean kinetic energy may be due to stronger inertia in western boundary currents obtained with FRS. In regions R3 and R4, there are weak barotropic and baroclinic instabilities in contrast with the NOS case. $\overline{K}$ in R3 is much larger than in R4, a different behaviour from NOS. Observation indicates that $\overline{K}$ is larger in Gulf Stream extension than in Gulf Stream (Richardson, 1983). The conversions of barotropic and baroclinic instabilities in the North Equatorial current region have the same directions in the FRS as in the NOS.

The baroclinic conversions ($\overline{P}$, P') and (P', K') are accomplished by the horizontal and vertical eddy heat transports, which are in turn correlations between the meridional (v') and vertical velocity (w'), and temperature (T') perturbations. In Figure 3.12, we show the zonally averaged latitude/depth distribution of these transports for the NOS and FRS conditions. The transports are more confined in the latter case, having significant amplitude only near the North Equatorial current and western boundary current outflow regions. The zonally averaged mean temperature are also shown as dashed contoures in Figures 3.12(c), and (d); they are similar to the zonally averaged instantaneous temperature field (Figures 3.9(c), (d)). Charney and Stern (1962) showed that a necessary condition for baroclinic instability of a zonal flow in a stratified fluid is the vanishing of the potential vorticity gradient on isentropic surfaces. As we have only temperature as the state variable, the latter surfaces are essentially isothermal surfaces. Examination of the distributions of temperature

and potential vorticity (figures not shown) indicates that the regions of baroclinic instability are consistent with the Charney-Stern criteria.

There is a significant difference in the level of baroclinic instability between the NOS and FRS cases in our model. The baroclinic conversions are determined by both the mean temperature gradient and the eddy heat transports (Appendix C). The mean temperature distributions for the NOS and FRS cases are similar (Figures 3.12(c), (d)). The much stronger eddy heat transports for NOS (Case 4) shown in Figure 3.12 are thus responsible for the enhanced baroclinic conversions.

Earlier studies using a wind-driven homogeneous constant depth ocean (Bryan, 1963; Veronis, 1966) have shown that the currents are quite different for FRS and NOS conditions if the Reynolds number is sufficiently large. Veronis (1966) obtained both stable western and northern boundary currents by using of FRS conditions. However, Bryan (1963) obtained unstable western boundary currents for NOS conditions. Blandford (1971) used barotropic ocean models to show that the difference between the results of Bryan (1963) and Veronis (1966) is due to the use of different boundary conditions. Analytical studies of two-layer baroclinic instability by Mysak et al. (1981) showed that the NOS boundary condition can generate barotropic as well as baroclinic instability in coastal currents due to the horizontal shear. Our results show, in a multi-level PE model, that both baroclinic and barotropic instabilities are enhanced with NOS conditions.

As discussed earlier, the local barotropic and baroclinic instabilities are weak in the open ocean, but the NOS case has a much larger eddy kinetic energy (K') than the FRS case. This suggests that K' can propagate effectively from the boundary to the interior of the domain. This may be an important mechanism for the generation of mesoscale activity in the open ocean as suggested by observational studies (Richardson, 1983; Wunsch, 1983).

Seaver (1987) used satellite-derived sea surface temperature anomalies over a period of several years in the North Atlantic to derive eddy statistics. The location and timing of the enhanced warm core eddy formation is associated with the recirculation

which coincides with regions of strongest horizontal current shear, thus suggesting that barotropic instability is one of the possible sources of Gulf Stream rings. Our results show that mixed barotropic and baroclinic instabilities are important in the western boundary current and its outflow regions. This is consistent with Seaver's results, theoretical study of Haidvogel and Holland (1978) and previous numerical results (Holland et al., 1983). As already noted, in the free jet (Gulf Stream extension) and North Equatorial Current regions, baroclinic instability dominates barotropic instability.

Han (1975) found little eddy activity with a flat bottom ocean PE model using FRS conditions; the western boundary current also overshot in the midlatitudes. Holland and Lin (1975a), and Robinson et al. (1977) used a flat bottom primitive equation model with FRS conditions to study single gyre ocean circulations. Both studies obtained western and northern boundary currents, the latter being a result of the single gyre forcing. There is little instability near these two boundary currents except along the northern returning flow; the latter being attributed to either baroclinic or barotropic instability.

It is important to note that topography and a highly scale selective diffusion parameterization may be able to produce instabilities near the western boundary even with FRS conditions. For example, Semtner and Mintz (1977) found the dominant instability occured within the simulated Gulf Stream over the continental rise. Over the flat abyssal plain, energy was transferred from eddies to the mean flow.

3.5 Northward heat transport

A quantity of primary interest in studies of the ocean's role in the global climate system is the northward heat transport. A number of techniques has been developed for obtaining the oceanic transport as residuals from the atmospheric transports and the requirement for a global heat balance (e.g., Oort and Vonder Haar, 1976).

Numerical models provide an alternative method for estimating the ocean heat

transport. However, there are considerable discrepancies between the estimates obtained from similar models. The sensitivity of the computed transports to the various modelling assumptions is not well known (Bryan, 1986). An important question is the effect of eddies on the northward heat transport. In the midlatitude atmosphere, eddies play a key role in the northward heat transport. Previous eddy resolving ocean circulation models (Mintz, 1979; Cox, 1985; Bryan and Holland, 1989; Bryan, 1991; Boning and Budich, 1992) indicated that eddies do not play a significant role in the northward heat transport as their effects are almost offset by the mean currents.

At a given latitude, the northward heat transport may be evaluated as

$$HT = \int_{-H}^{0} \int_{0}^{L_X} C_p \rho_0 v T dx dz \tag{3.1}$$

where H, L_X are the depth and width of the ocean domain at a given latitude respectively. The mean northward heat transport may be further divided into its time mean and time variant components by

$$\overline{HT} = \int_{-H}^{0} \int_{0}^{L_X} C_p \rho_0 \overline{v}\,\overline{T} dx dz + \int_{-H}^{0} \int_{0}^{L_X} C_p \rho_0 \overline{v'T'} dx dz \tag{3.2}$$

where the bar and prime indicate time mean and variation about the time mean respectively.

The vertical distribution of $\overline{v'T'}$ for NOS and FRS conditions are shown in Figures 3.12(a) and (b). The eddy heat transport by the time variant flow is concentrated in the upper 1000 m, with southward transport near the North Equatorial Current and northward transport near midlatitudes. The northward eddy heat transport by the time variant flow is much stronger for the NOS than for FRS case.

Figure 3.13(a) shows the northward heat transport and its time mean and time variant components for NOS conditions. The total heat transport is everywhere northward with a peak near midlatitudes. This is in general agreement with previous estimates of the heat transport using idealized models of the North Atlantic (Weaver and Sarachik, 1990; Gough and Lin, 1992). The time variant flow component is small except near the southern boundary where southward transport occurs. The down gradient southward heat transport across the upward sloping isotherms near the North

Equatorial Current is compensated by the enhanced mean flow transport. There is a small northward eddy heat transport by the time variant flow in the midlatitudes and the subpolar gyre. The total heat transport is similar to that obtained at coarse resolution (Cox, 1985; Bryan, 1986, 1987, 1991; Bryan and Holland, 1989; Boning and Budich, 1992).

The situation is however different for FRS conditions (Figure 3.13(b)). The transport of the fine grid FRS solution (Case 4) is larger than that of the coarse grid solution, even though the eddies are not important. The mean meridional circulations of NOS and FRS are shown in Figures 3.14 and 3.15 respectively. The main reason for the increase in heat transport at midlatitudes and in the subpolar gyre is because of an enhanced thermohaline circulation in FRS and more concentrated in the subpolar gyre.

We next decompose the mean heat transport into six components: barotropic gyre transport, baroclinic overturning transport, baroclinic gyre transport, Ekman overturning transport, Ekman gyre transport (zero for the purely zonal wind stress shown in Figure 3.2(b)), and explicit diffusion. Their definitions are given in Appendix D.

Figure 3.16 shows the components obtained for the fine resolution FRS conditions (Case 4). The transport by the barotropic gyre and explicit diffusion are negligible. The biggest contributions are from the opposing Ekman and baroclinic overturning transports. The northward transport is mainly accomplished by the Ekman current in subtropical regions, and by the baroclinic overturning gyre at midlatitudes. Note that the temperature gradient in the North Equatorial Current is southward, but the Ekman current still transports heat northward. Assuming the local temperature change is due only to heat flux convergence, we have

$$\begin{aligned} \frac{\partial T}{\partial t} &= -\frac{\partial (vT)}{\partial y} \\ &= -v\frac{\partial T}{\partial y} - T\frac{\partial v}{\partial y} \end{aligned}$$

The first term on the right hand side is negative for northward motion near the North

Equatorial Current, but the second term is positive and dominates the first term. It is thus the convergence of velocity due to the Ekman transport which constitutes the heat transport in this region. Away from the North Equatorial Current, both terms may be important (Sarmiento, 1986).

The baroclinic gyre transport is generally northward (Figure 3.16). Physically, this transport is due to warm water move northward at one location at one level and cold water returning southward at a deeper level and different location. It is smaller than the Ekman and baroclinic overturning components, but much bigger than those due to the barotropic gyre and explicit diffusion.

All components of the heat transport obtained with FRS are similar to those obtained with NOS conditions, except for the baroclinic gyre component and baroclinic overturning component. Figure 3.17 shows that the FRS case has stronger baroclinic gyre and overturning transports in both midlatitudes and in the subpolar gyre. The difference is mainly due to a stronger western boundary mean current in the FRS case, carrying more warm water northward. Bryan (1986) showed that a higher vertical diffusivity induces stronger northward heat transport and a northward shift of its peak. The northward shift of the maximum heat transport is again due to the stronger western boundary current overshooting further north than at a lower vertical diffusivity.

We close this section by examining the effect of vertical resolution. Both eddy kinetic and eddy available energy are increased when the number of vertical levels is doubled. The enhanced eddy kinetic energy is due to the better resolved vertical stratification, which generates a stronger baroclinic conversion (P', K'). The barotropic conversion ($\overline{K}$, K') is a little weaker than at low vertical resolution, but the general spatial pattern remains similar. The midlatitude free jet and its eastward extension are also enhanced. These results are similar to those of Semtner and Holland (1978), Holland and Schimtz (1985). However, there is no clear effect of vertical resolution on the northward heat transport in the eddy regime, a result similar to coarse resolution studies (Weaver and Sarachik, 1990).

3.6 Summary and conclusions

A C-grid primitive equation model has been used to study the eddy energetics and its effect on the northward heat transport. We have focused on the effect of no slip (NOS) and free slip (FRS) boundary conditions. The main conclusions can be summarized as follows.

Boundary conditions play a very important role in the eddy resolving regime. FRS conditions tend to constrain western boundary currents near the coast to give an intense mean boundary current which overshoots north of the latitude of zero wind stress curl. NOS conditions tend to produce an unstable western boundary current due to the strong horizontal current shear induced by forcing the velocity to vanish at the coast. The basin averaged eddy energetics for NOS are more intense than for FRS conditions, with enhanced baroclinic and barotropic instabilities in the former case. The mean kinetic energy is however about twice as large for the FRS case. In contrast, QG models show both eddy and mean kinetic energies are much larger for FRS than for NOS conditions.

Although the basin averaged energetic analysis shows stronger baroclinic and barotropic instabilities for NOS conditions (Cases 3, 5), their horizontal distribution reveals regional differences. Indeed, there is only significant difference in the western boundary current and its outflow regions between the NOS and FRS cases, with the latter having much weaker baroclinic and barotropic instabilities. The general pattern of eddy kinetic energy for NOS in the top layer is very similar to that of Cox (1985), and Boning and Budich (1992), both are based on the B-grid model of Bryan (1969). Detailed comparison is difficult due to the use of stronger wind stress amplitude and the presence of a continental shelf along the western boundary in the latter two studies. Barnier's group (personal communication, 1993) is running the C-grid model of Haidvogel et al. (1991) in eddy resolving regime with basin scale geometry and will compare the results with the corresponding B-grid simulations.

The total heat transport for NOS conditions in the eddy regime (Case 3) is similar to that obtained at coarse resolution. The heat transport by the time variant flow

is almost compensated by the enhancement in the mean flow heat transport. The FRS case has almost no heat transport by the time variant flow, but the transport in the eddy regime (Case 4) is larger than at coarse resolution near the midlatitude and the subpolar gyre. By decomposing the mean heat transport into six different components for both NOS (Case 3) and FRS conditions (Case 4), we find that the extra heat transport in the latter case is produced by baroclinic gyre and overturning transports, both of which are components of thermohaline circulations.

The Community Modelling Effort (CME) model (Bryan and Holland, 1989) is intended to address the role of eddies in the North Atlantic general circulation, and to provide a benchmark for the development of the basin scale numerical models. Treguier (1992) compared the CME model results with both observations and QG models, and found that the CME model greatly underestimates the K' level. She attributed the discrepancy to the lack of inertia in the western boundary currents due to insufficient spatial resolution and excessive lateral friction. As in Haidvogel et al. (1992), our results suggest that the use of an intermediate boundary condition between FRS and NOS (the "slip" condition) can increase the western boundary current inertial, and the northward heat transport.

Table 3.1: The vertical discretization of the model for low and high vertical resolutions. The level depth is in the mid-point of each layer.

level	level depth (m)	layer thickness (m)	level depth (m)	layer thickness (m)
1	25	50	12.5	25
2	75	50	37.5	25
3	150	100	62.5	25
4	250	100	87.5	25
5	400	200	125	50
6	600	200	175	50
7	850	300	225	50
8	1200	400	275	50
9	1600	400	350	100
10	2000	400	450	100
11	2400	400	550	100
12	2800	400	650	100
13	3250	500	775	150
14	3750	500	925	150
15			1100	200
16			1300	200
17			1500	200
18			1700	200
19			1900	200
20			2100	200
21			2300	200
22			2500	200
23			2700	200
24			2900	200
25			3125	250
26			3375	250
27			3625	250
28			3875	250

Table 3.2: A summary of the dissipative parameters used in the numerical experiments. Negative values of A_{MH} and A_{HH} refer to biharmonic diffusion, with units of $cm^4\ s^{-1}$; all other parameters have units of $cm^2\ s^{-1}$.

Case	levels	A_{MH}	A_{HH}	A_{MV}	A_{HV}	λ
	Coarse resolution $\Delta x = \Delta y$=100 km					
1. no slip	14	1×10^8	10^7	20	1	2×10^9
2. free slip	14	1×10^8	10^7	20	1	2×10^9
	Fine resolution $\Delta x = \Delta y$=40 km					
3. no slip	14	-10^{19}	-2.5×10^{19}	20	0.5	5×10^8
4. free slip	14	-10^{19}	-2.5×10^{19}	20	0.5	5×10^8
5. no slip	28	-10^{19}	-2.5×10^{19}	20	0.5	5×10^8

Table 3.3: Typical horizontal length (L) and velocity (U) scales, and Rossby (R_0), Reynolds (R_e) and Peclet (P_e) numbers for various experiments. WBL denotes the western boundary layer.

Domain	L (cm)	U (cm s^{-1})	R_0	R_e	P_e
	coarse resolution, 14 levels				
interior	10^8	1	10^{-4}	2.5×10^{-1}	2.5
WBL	10^7	10	10^{-2}	2.5×10^{-1}	2.5
	fine resolution, 14 and 28 levels				
interior	10^8	10	10^{-3}	1.6×10^3	6.4×10^2
WBL	10^7	100	10^{-1}	1.6×10^3	6.4×10^2

Table 3.4: The vertically averaged distributions of $\overline{K}$, K', and the conversions ($\overline{K}$, K'), (P', K'). The locations of R1, R2, R3, R4, R5 are indicated in Figure 3.11.

Domain	$\overline{K}$	K'	($\overline{K}$, K')	(P', K')
	no slip boundary condition			
R_1	0.9	18.1	-0.1	0.2
R_2	1.2	39.1	0.1	-0.1
R_3	37.8	130.0	42.2	56.0
R_4	69.0	74.0	23.4	16.8
R_5	3.9	10.2	-0.1	1.0
	free slip boundary condition			
R_1	1.7	6.9	-0.0	0.1
R_2	1.6	6.2	-0.1	0.4
R_3	114.4	21.3	1.1	5.2
R_4	59.0	3.0	0.3	1.2
R_5	3.8	5.6	-0.1	0.3

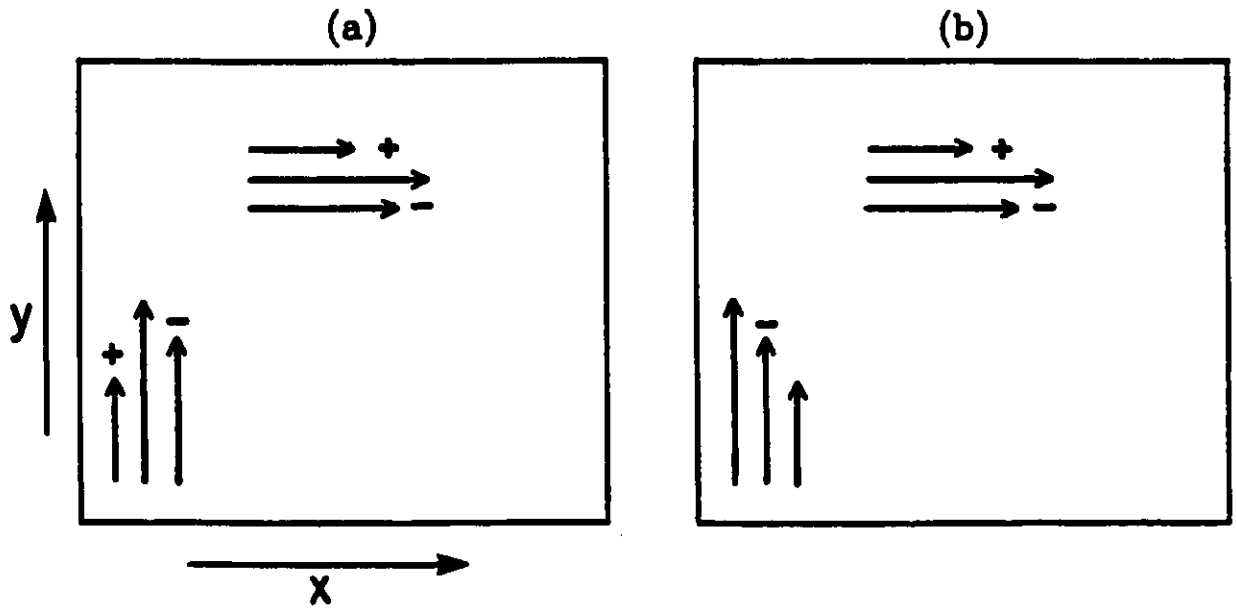

Figure 3.1: A schematic representation of the flow field near the western boundary with (a) no slip;, and (b) free slip boundary conditions. Positive and negative signs indicate the sign of the relative vorticity.

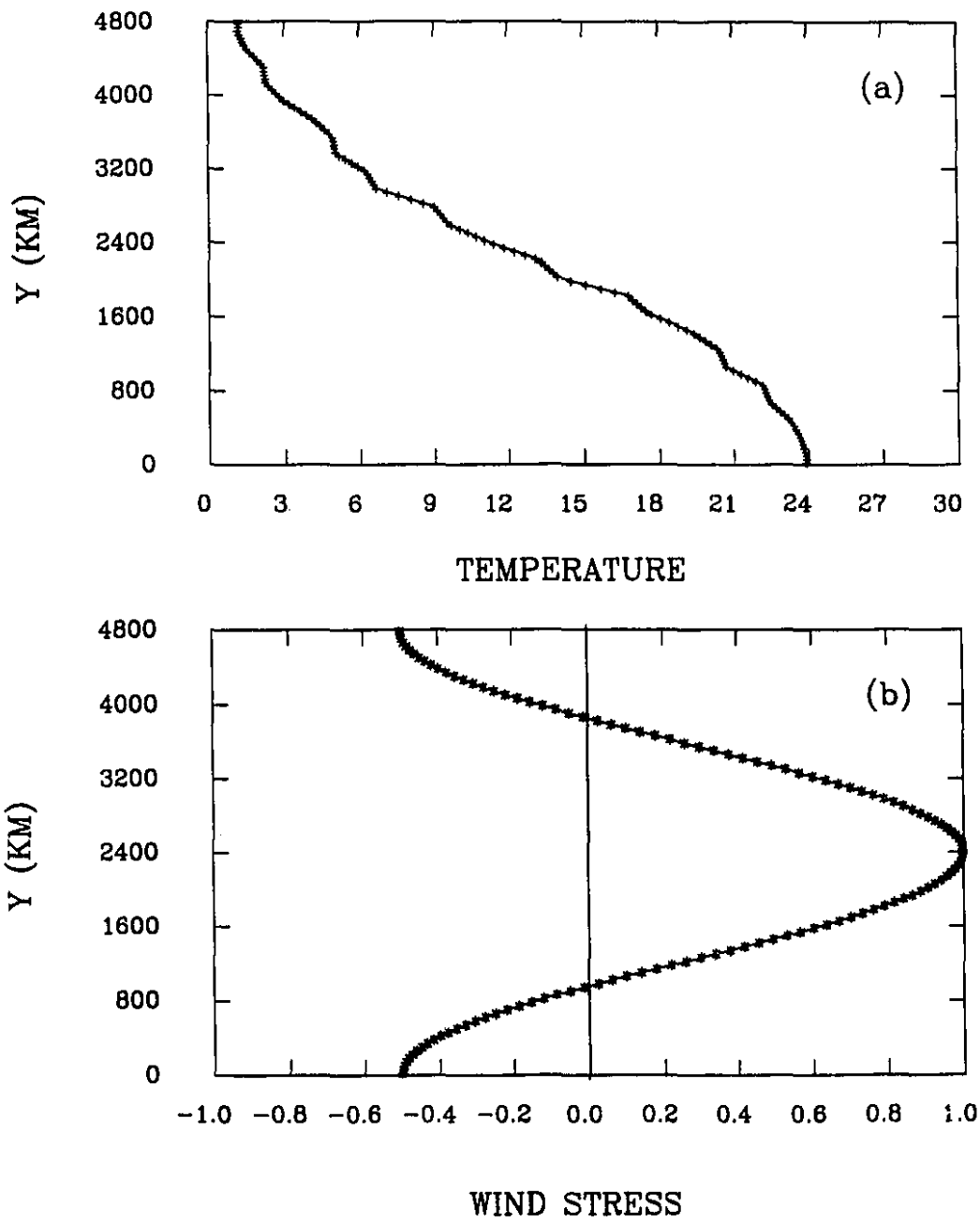

Figure 3.2: The latitudinal distribution of the (a) apparent atmospheric temperature (°C), and (b) zonal wind stress (dyne cm^{-2}), used as surface forcings. There is no variation with longitude.

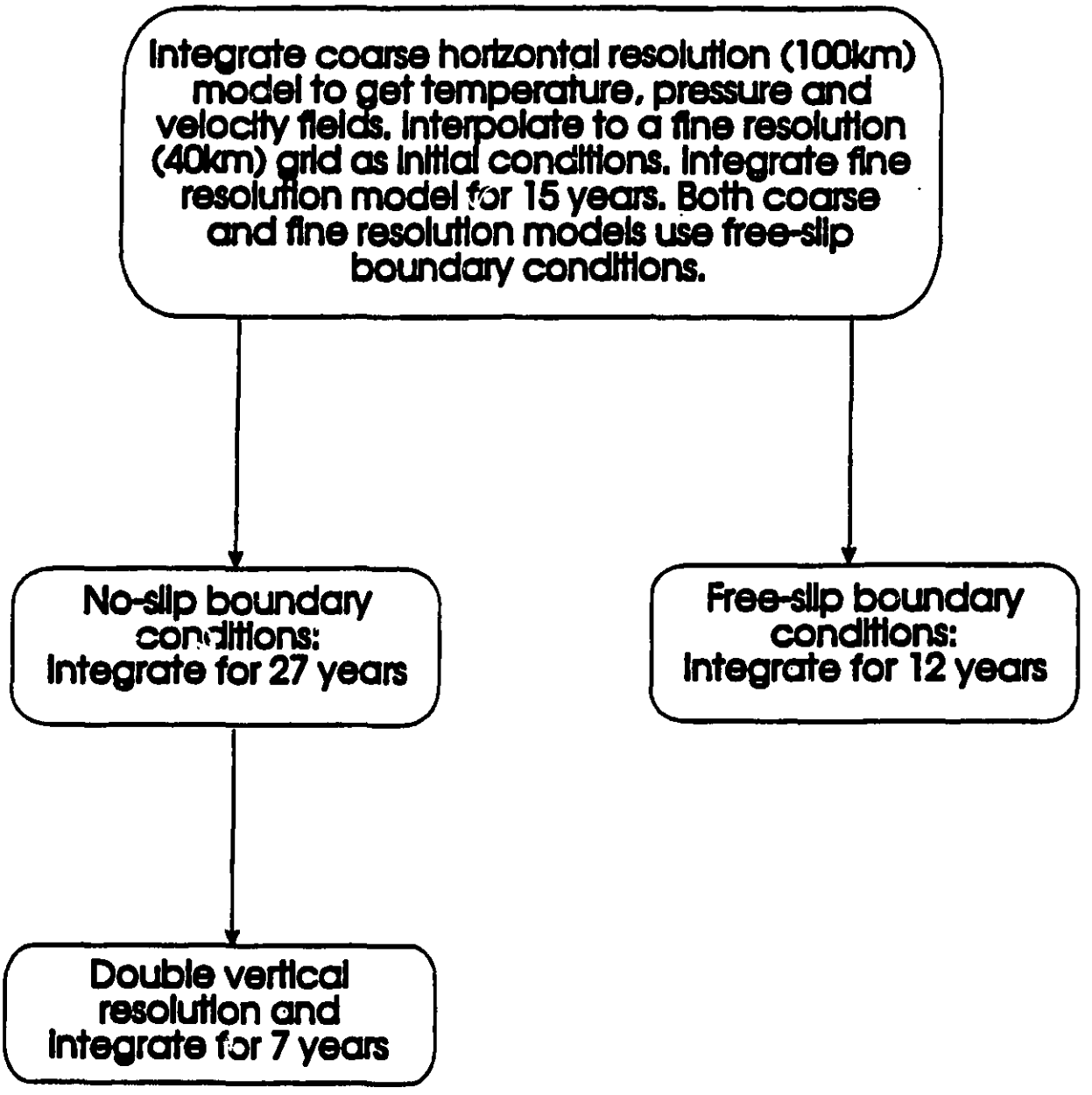

Figure 3.3: A flow chart describing the model experiments.

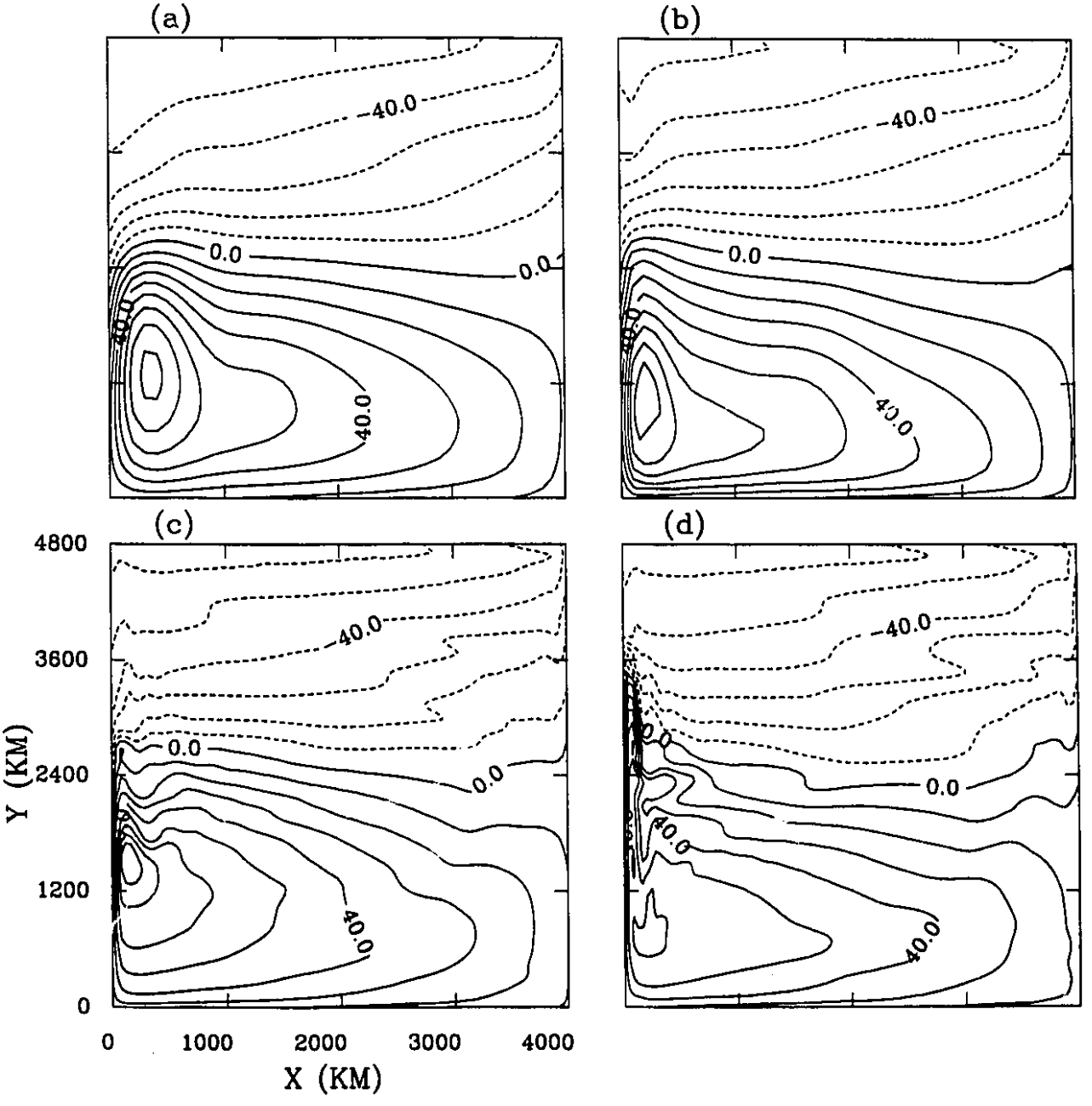

Figure 3.4: The equivalent surface topography (cm) for: (a) NOS coarse resolution (Case 1); (b) FRS coarse resolution (Case 2); the corresponding 5-year mean for (c) NOS fine resolution (Case 3); (d) FRS fine resolution (Case 4).

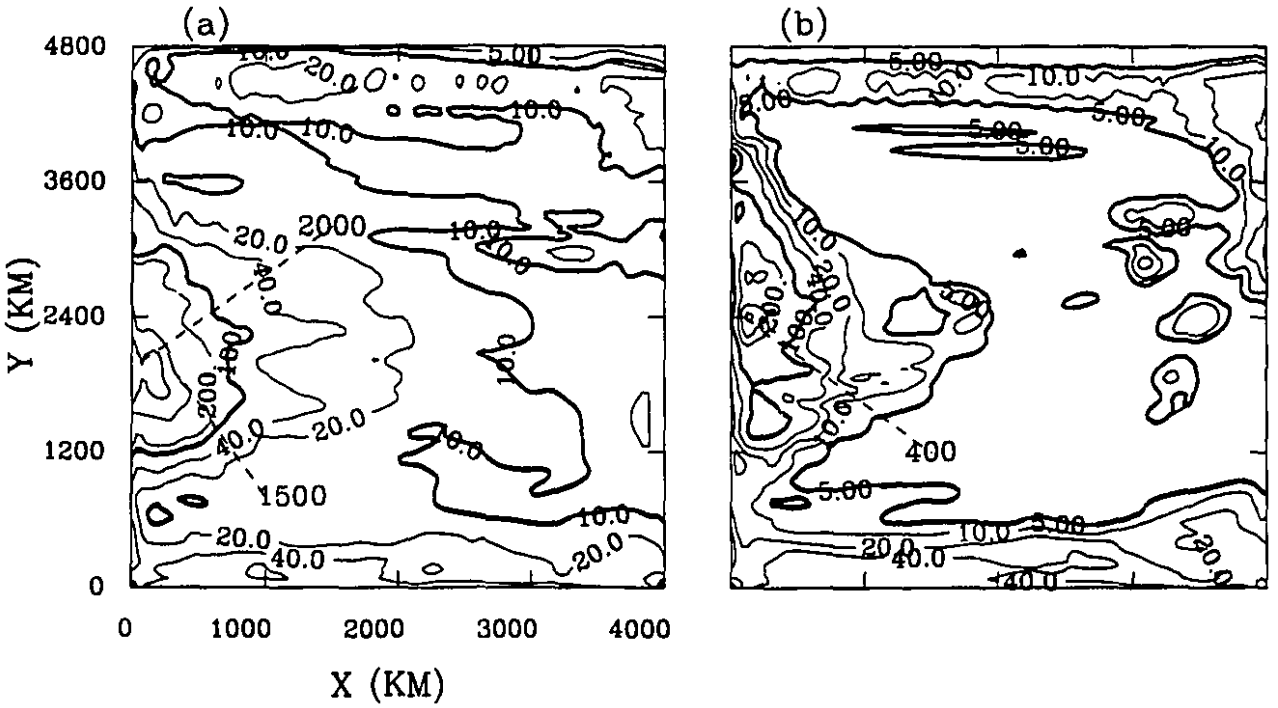

Figure 3.5: The horizontal distribution of 5-year mean K' ($cm^2\ s^{-2}$) at the top model layer for: (a) NOS (Case 3); (b) FRS (Case 4). The dashed lines are used to indicate the magnitudes of K'.

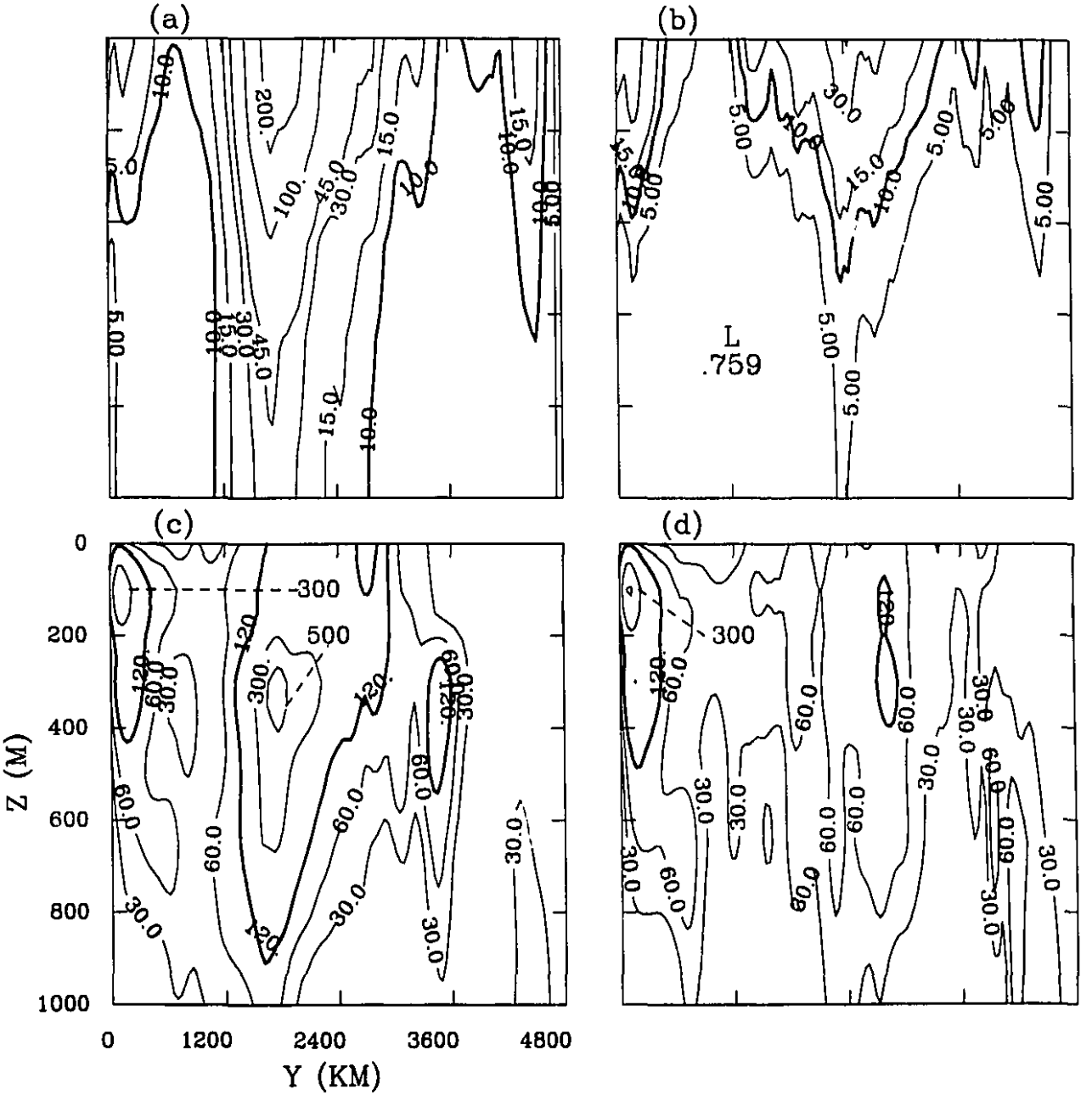

Figure 3.6: The zonally averaged distribution for 5-year mean K' ($cm^2\ s^{-2}$) on a vertical plane for (a) NOS (Case 3), (b) FRS (Case 4); the corresponding distributions of P' ($cm^2\ s^{-2}$) for (c) NOS (Case 3), and (d) FRS (Case 4). The dashed lines are used to indicate the magnitudes of K'.

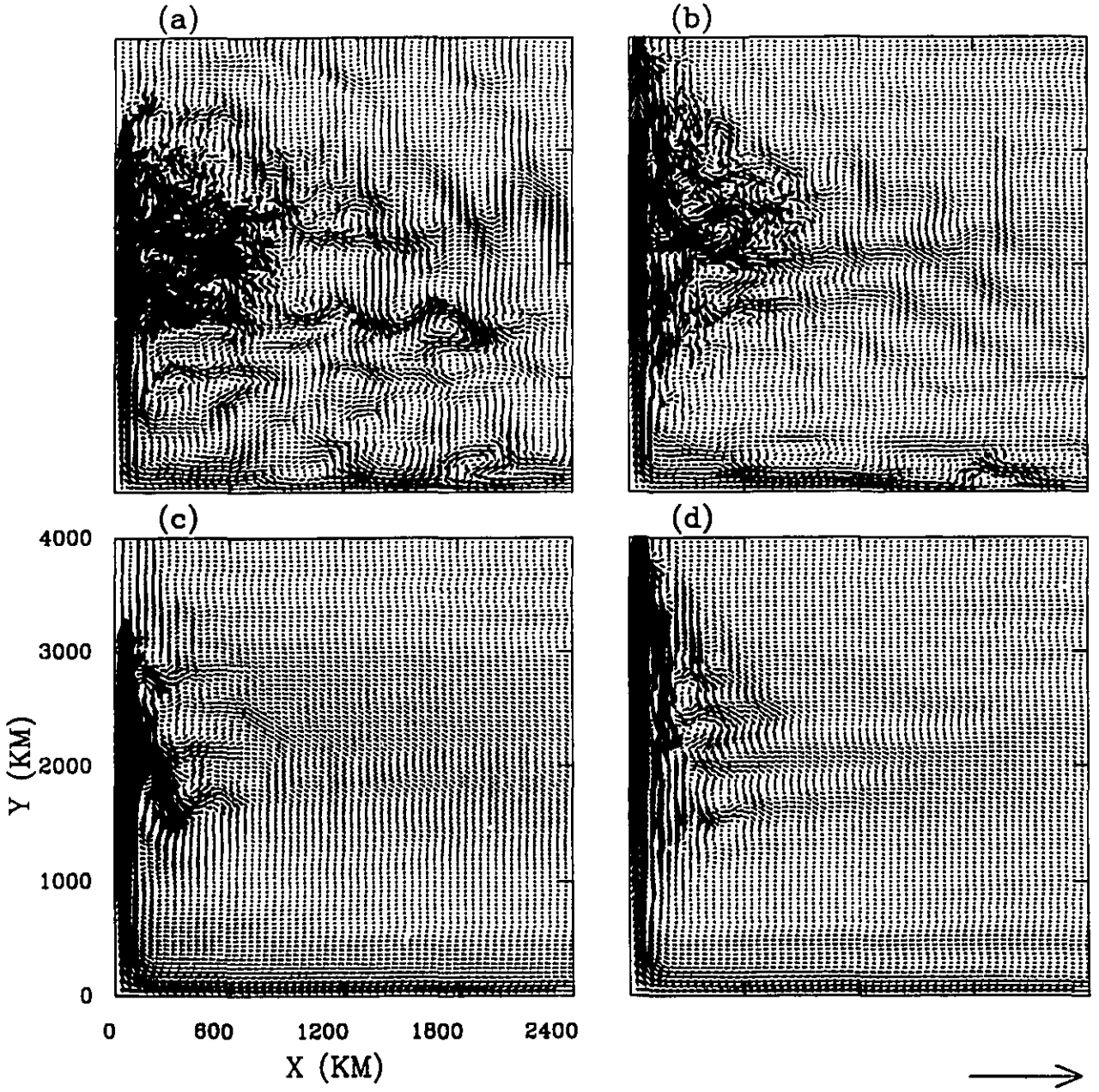

Figure 3.7: The distributions of horizontal velocities (cm s^{-1}). The magnitudes corresponding to the vector shown at the bottom right is given between parentheses. The instantaneous flow is obtained with (a) NOS (Case 3; 200.0), and (b) FRS (Case 4; 189.0) conditions; the 5-year time-mean flow for (c) NOS (Case 3; 152.0), and (d) FRS (Case 4; 181.1). Note the reduced north-south and east-west domain scale to focus on the western boundary.

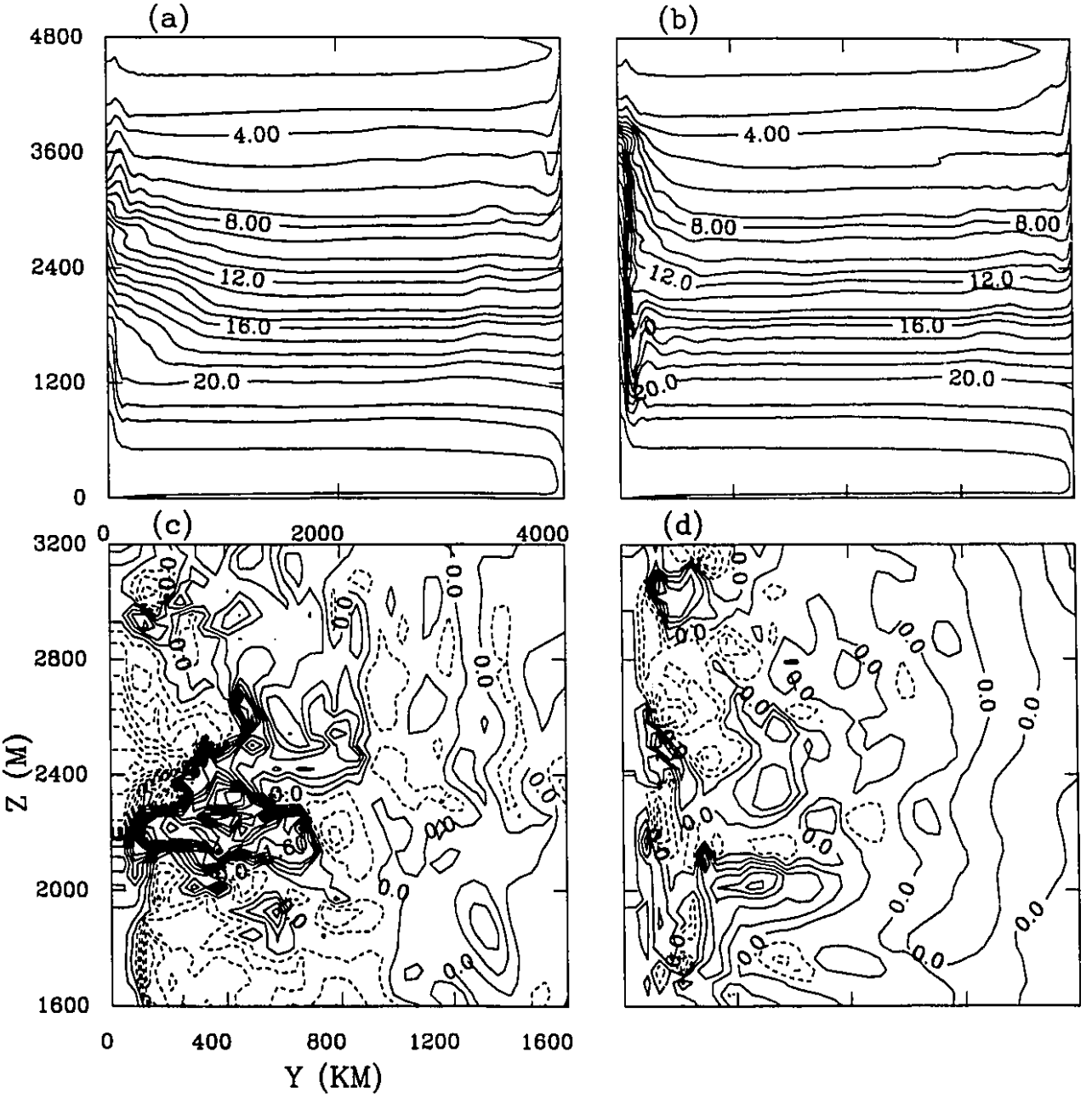

Figure 3.8: The top model layer horizontal distribution of 5-year time-mean temperature (°C) for (a) NOS (Case 3); and (b) FRS (Case 4). The deviation from the time mean temperature (°C) are shown in (c) NOS (Case 3; C.I.= 0.4); and (d) FRS (Case 4; C.I.= 0.4). Note the reduced north-south and east-west domain scale to focus on the western boundary for Figures (c) and (d).

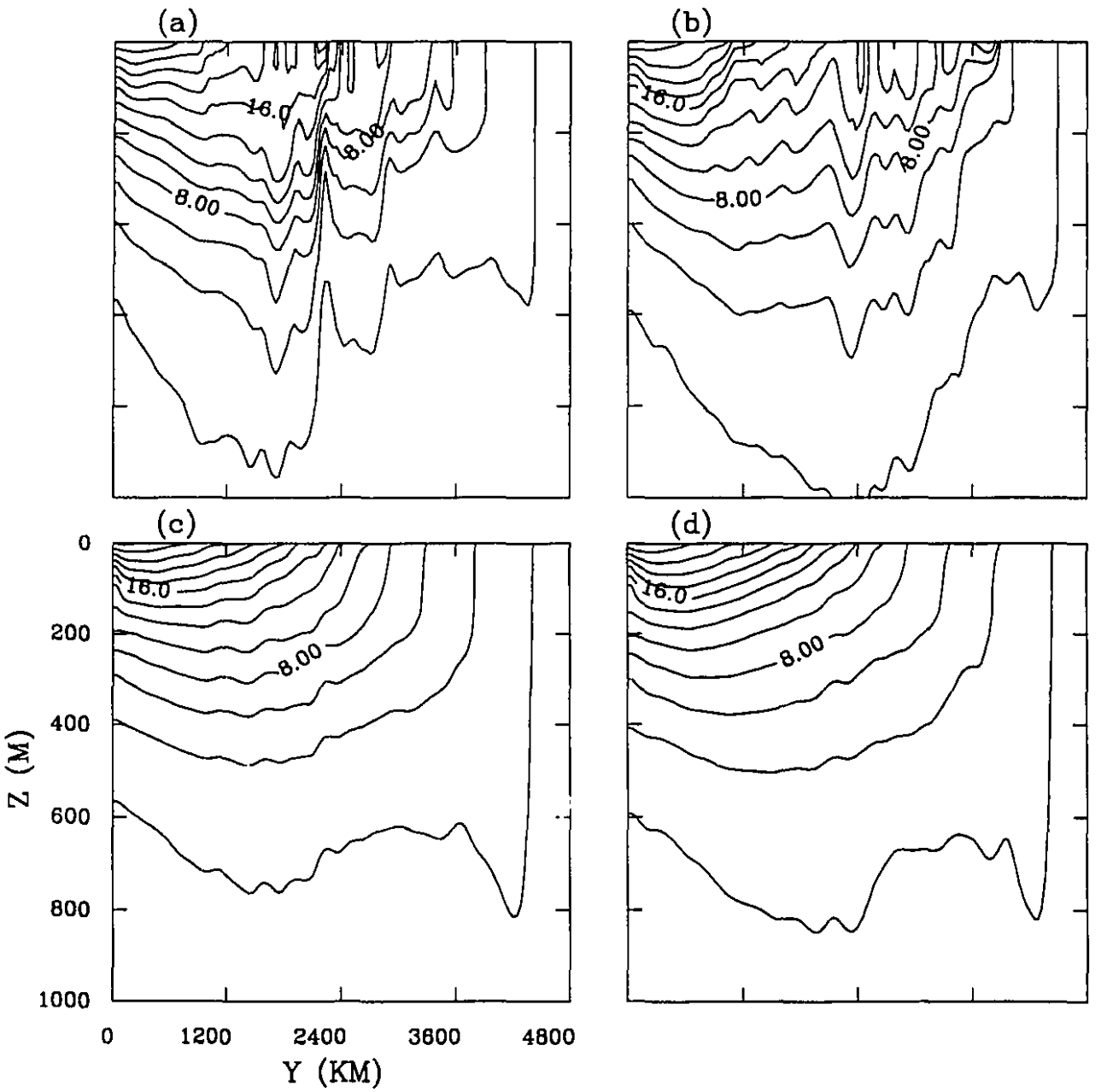

Figure 3.9: Meridional sections of the instantaneous temperature field (°C) along $X = 200$ km for (a) NOS (Case 3), and (b) FRS (Case 4); and the zonally averaged temperature field (°C) for (c) NOS (Case 3), and (d) FRS (Case 4).

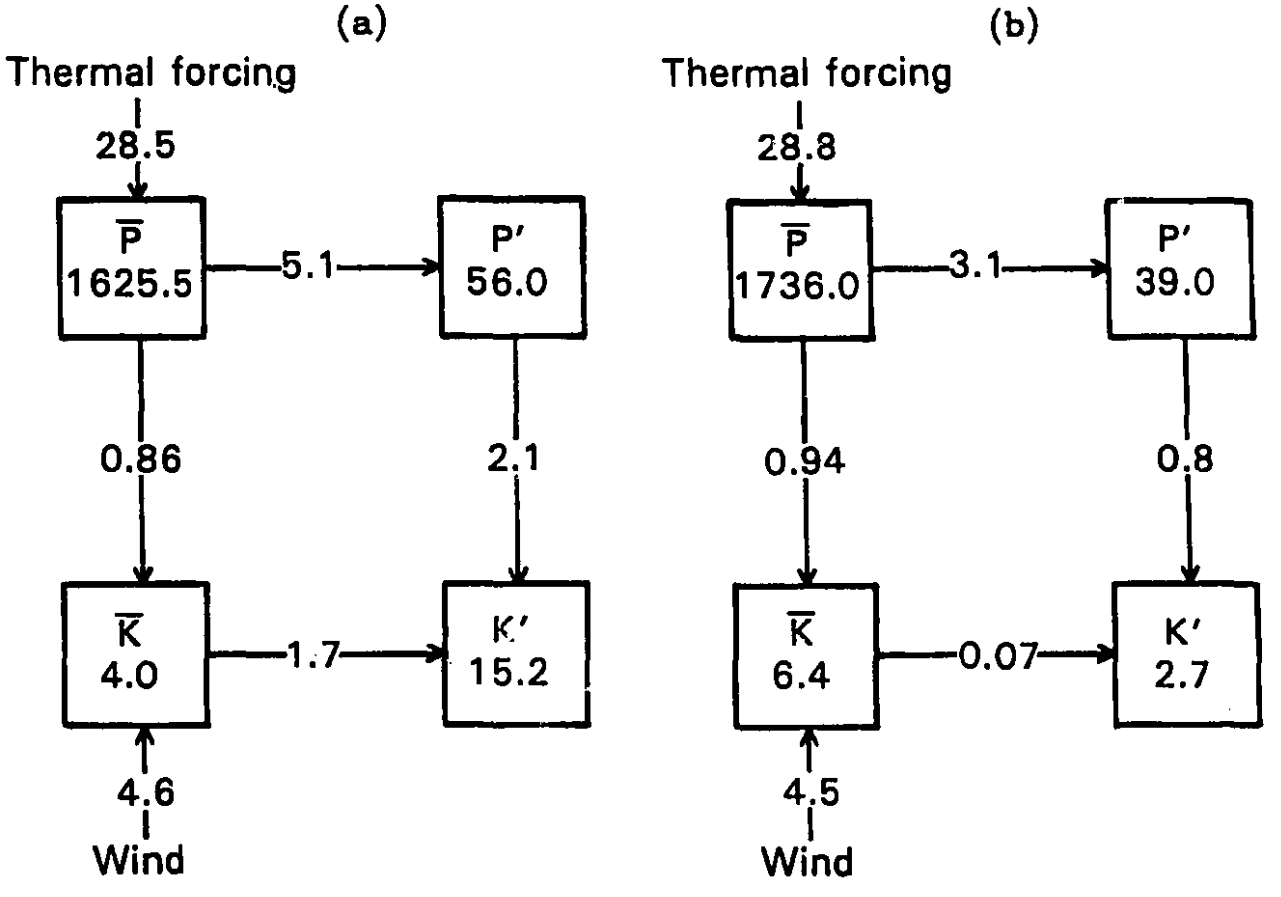

Figure 3.10: The 5-year mean basin averaged engertics of the eddy resolving flow: (a) NOS (Case 3); (b) FRS (Case 4); The units of the energy are in $cm^2\ s^{-2}$, and the conversion terms are in $10^{-6}\ cm^2\ s^{-3}$.

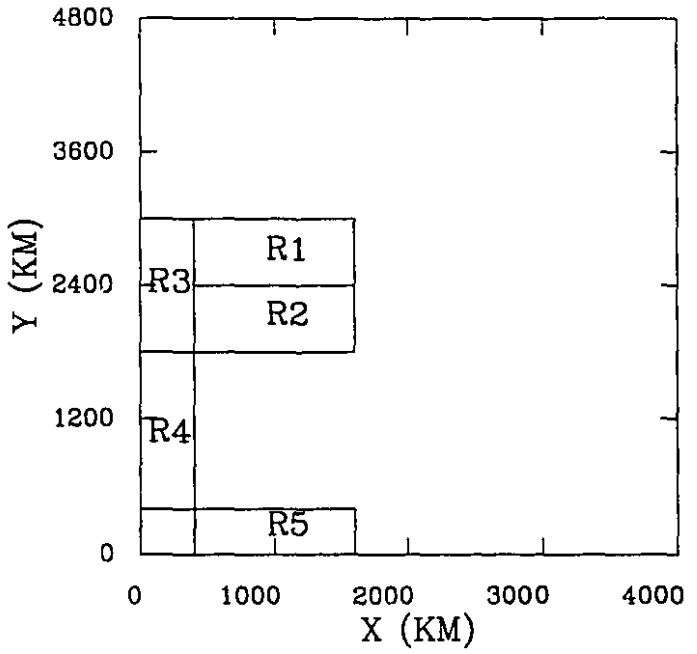

Figure 3.11: The locations of sub-regions R1, R2, R3, R4, R5 used in Table 3.4.

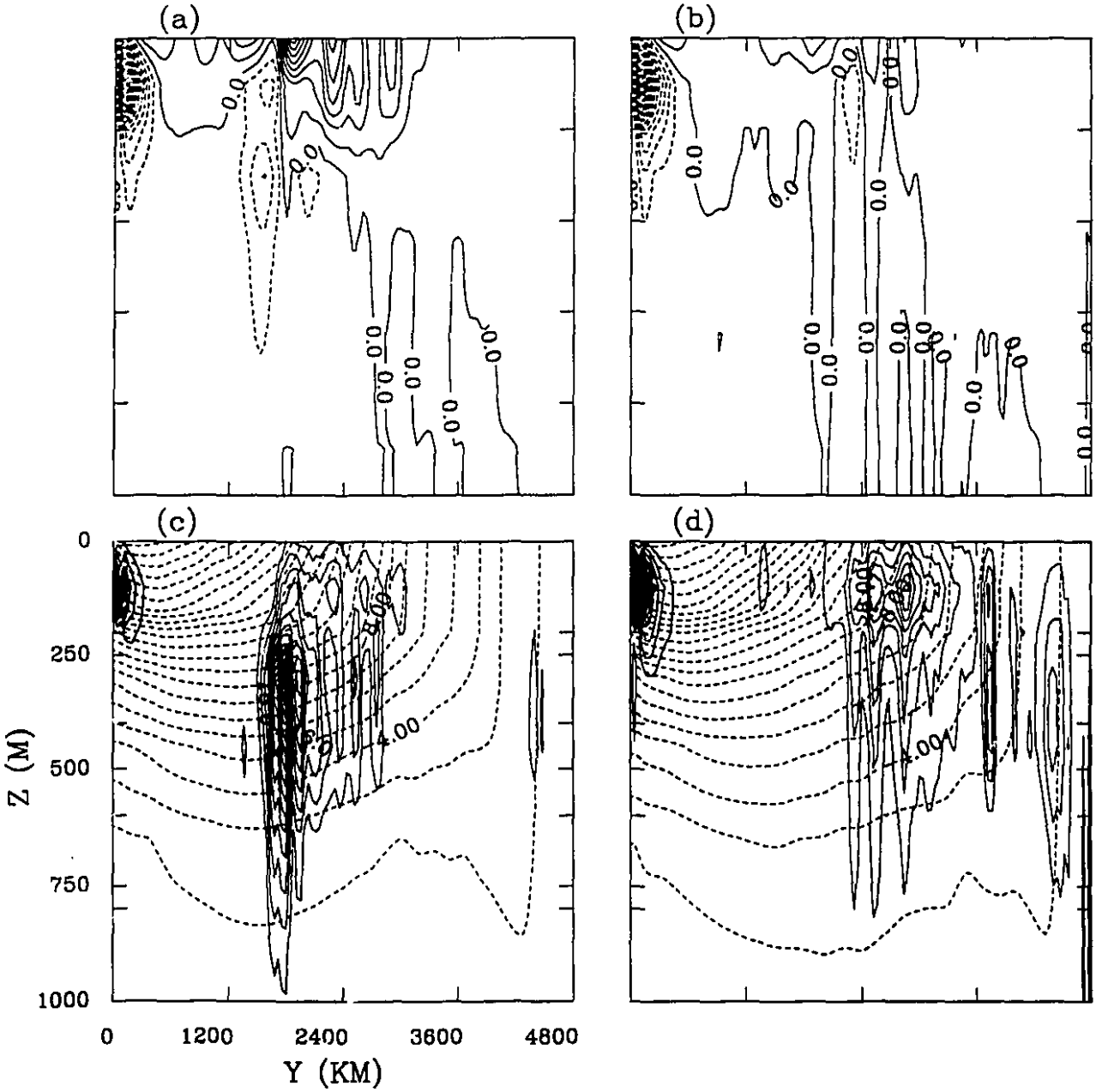

Figure 3.12: The distribution on a vertical plane of the horizontal heat transport $\overline{v'T'}$ (cm °C s^{-1}) for (a) NOS (Case 3, C.I.=0.2), and (b) FRS (Case 4, C.I.=0.2). The distribution of the vertical heat transport $\overline{w'T'}$ (cm °C s^{-1}) is shown by the solid lines for (c) NOS (Case 3, C.I.=4.$\times 10^{-5}$), and (d) FRS (Case 4, C.I.=2×10^{-5}). The dashed contours imposed in (c) and (d) are the zonally averaged mean temperature field.

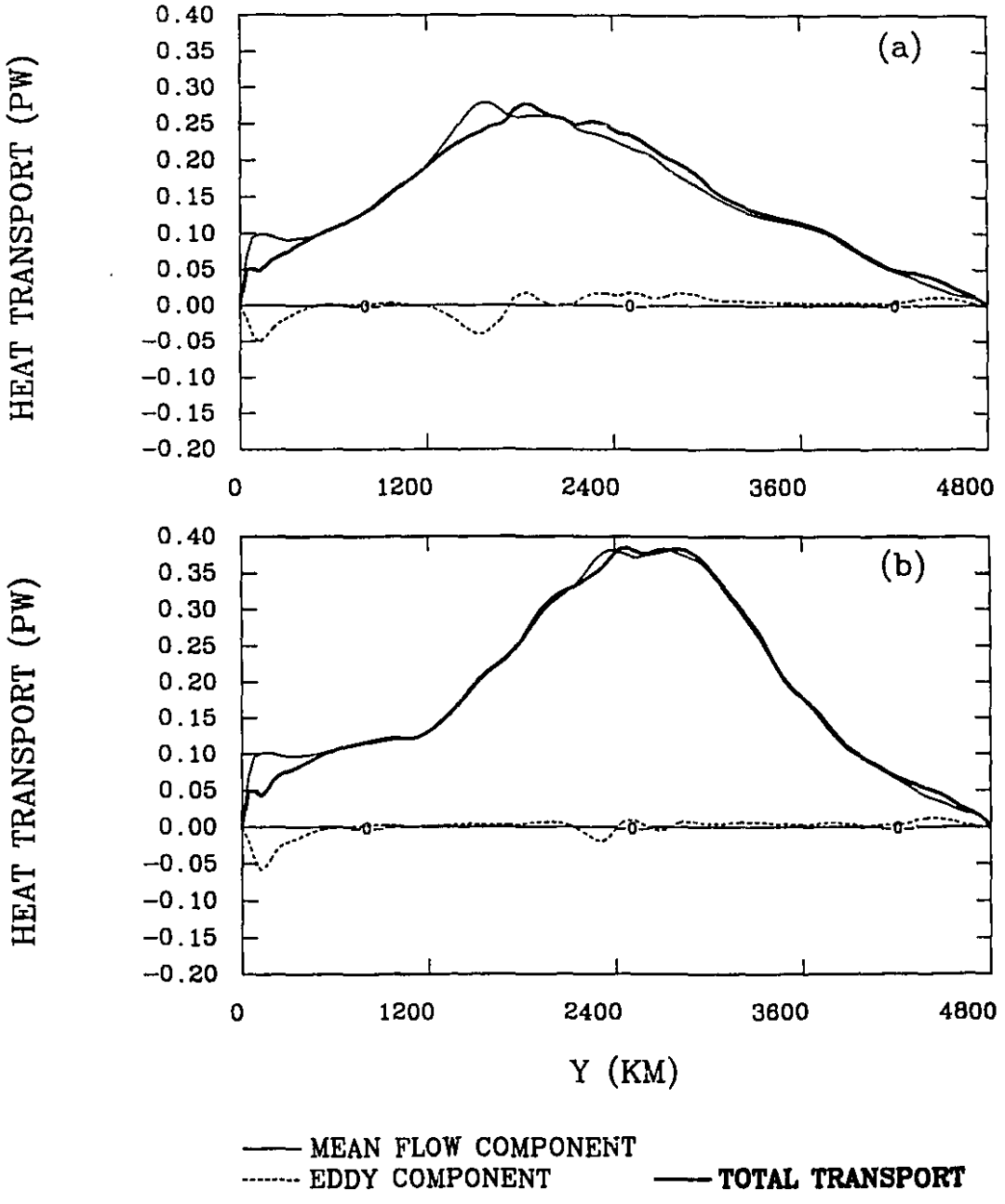

Figure 3.13: The 5-year mean northward heat transport (PW= 10^{15} watts) for: (a) NOS (Case 3); (b) FRS (Case 4).

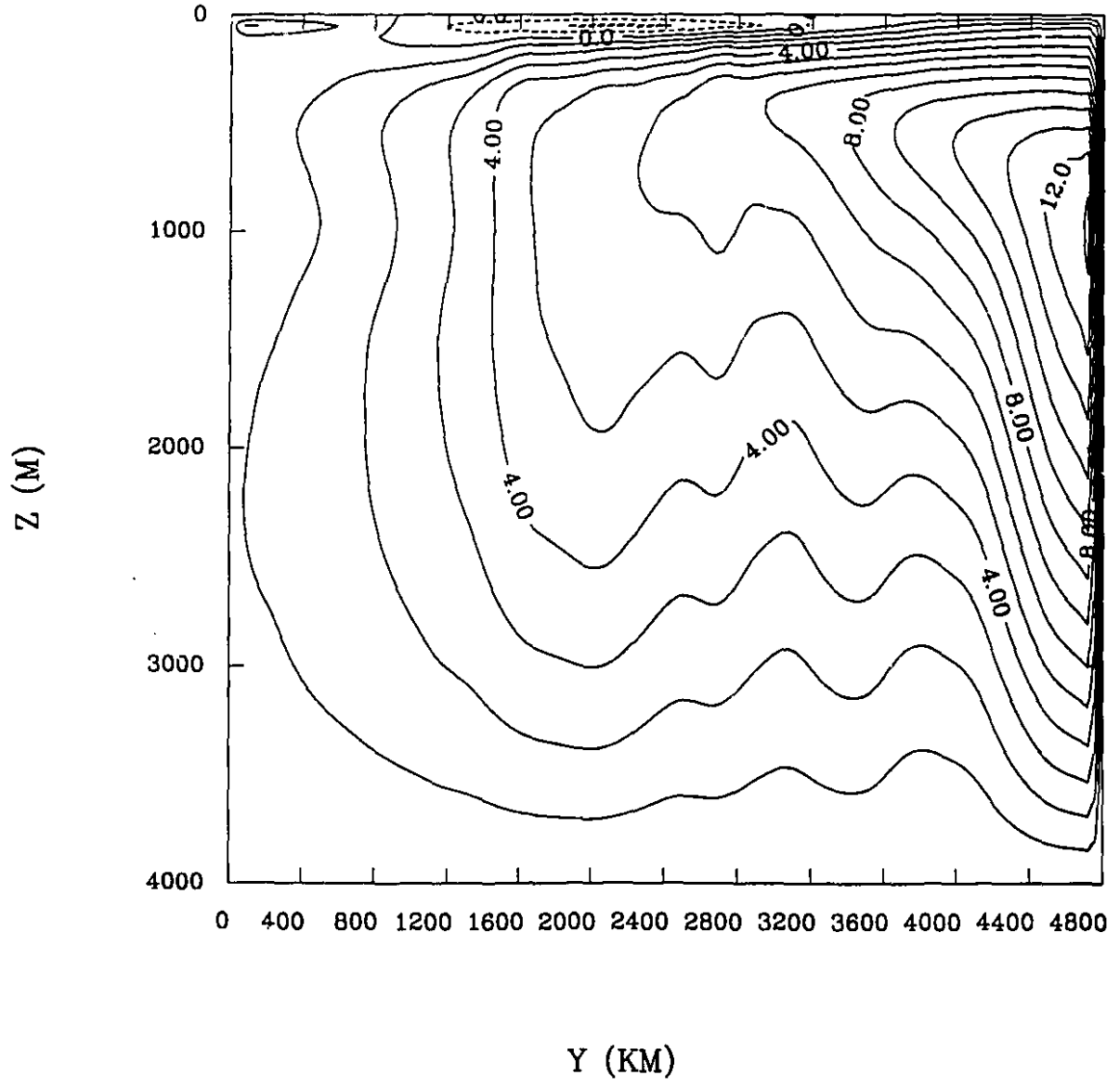

Figure 3.14: The mean meridional circulation, i.e., the thermohaline circulation (Sv) for NOS, with dashed lines indicating anticyclonic circulation, and solid lines indicating cyclonic circulation.

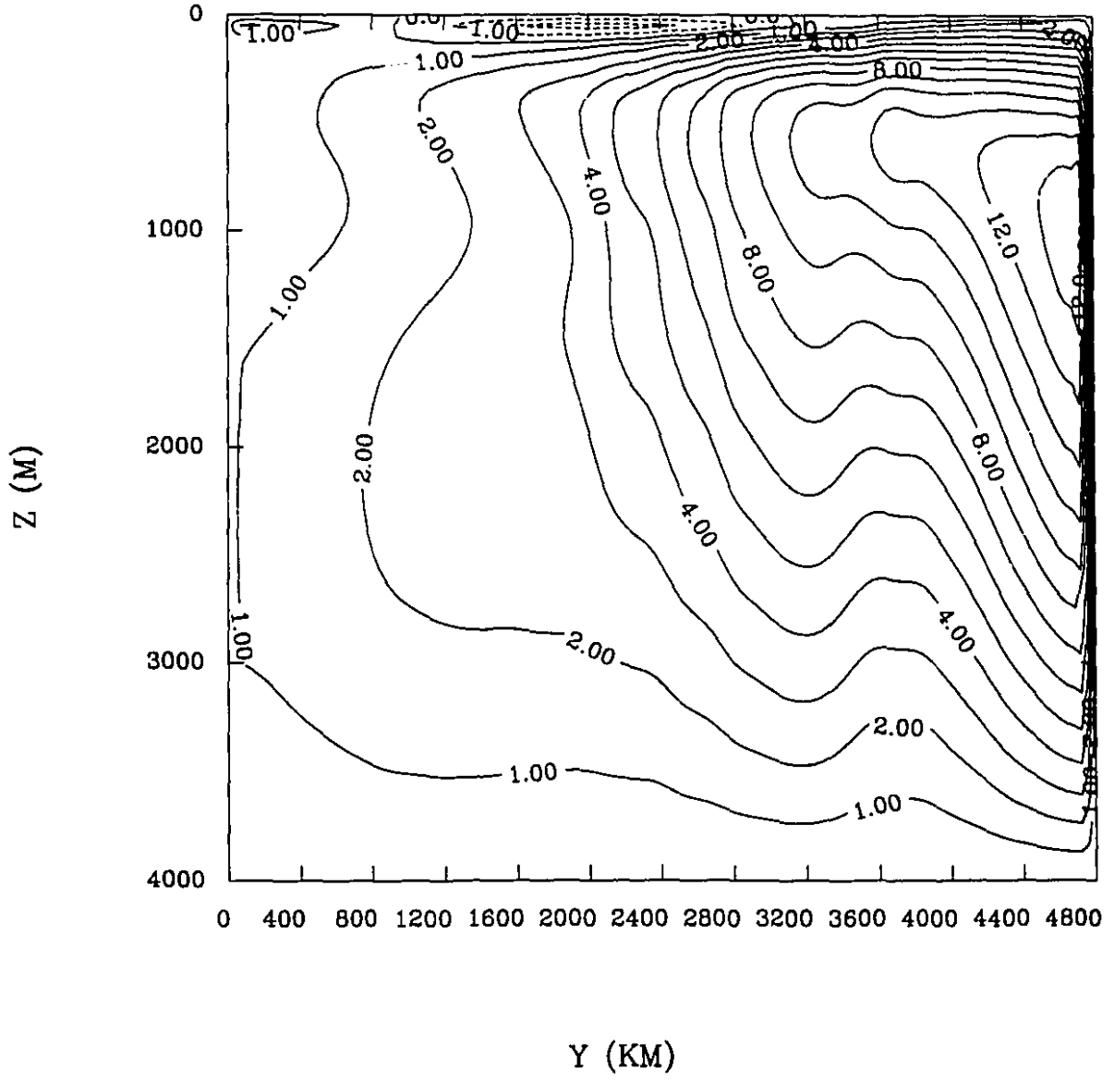

Figure 3.15: The mean meridional circulation, i.e., the thermohaline circulation (Sv) for FRS, with dashed lines indicating anticyclonic circulation, and solid lines indicating cyclonic circulation.

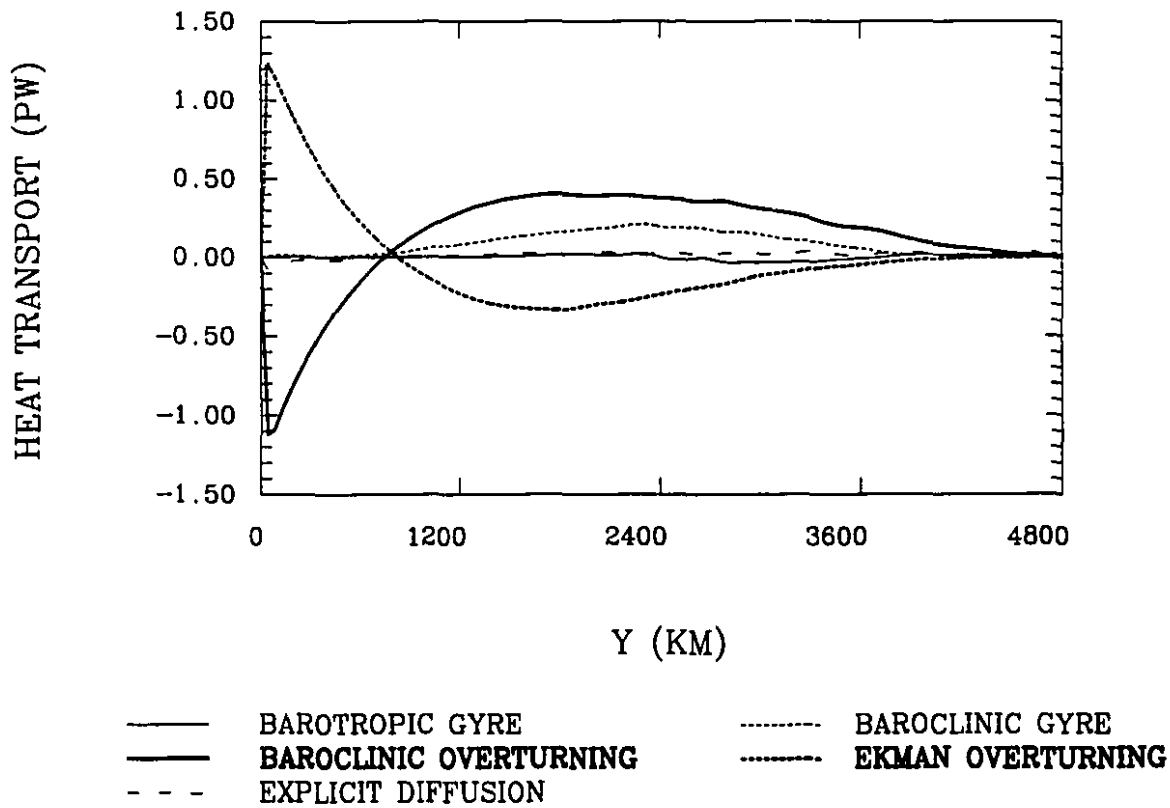

Figure 3.16: Components of the northward heat transport (PW= 10^{15} watts) by the time-mean flow for FRS (Case 4).

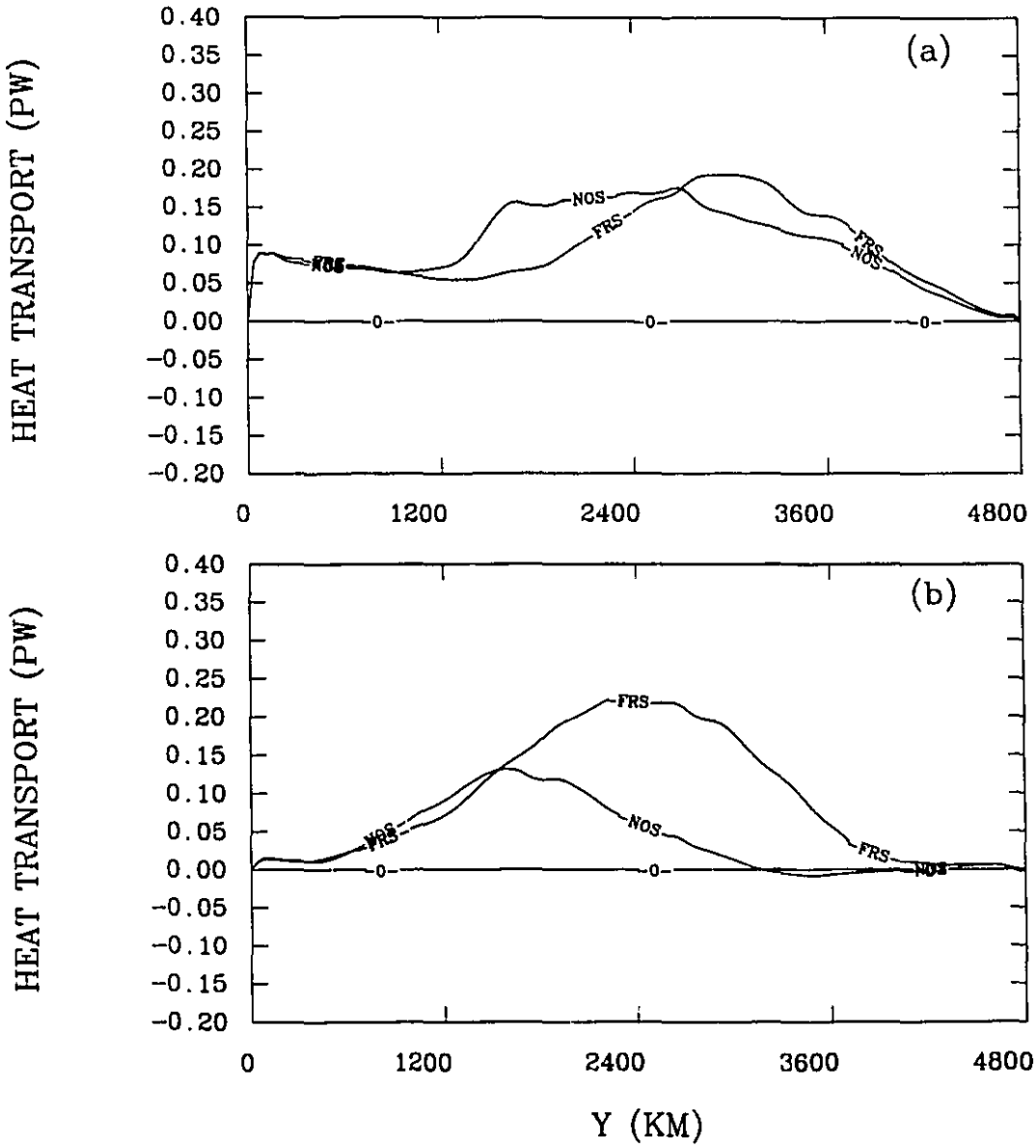

Figure 3.17: Comparison of the heat transport (a) the baroclinic overturning, and (b) the baroclinic gyre heat transport for NOS (Case 3) and FRS (Case 4).

Chapter 4

Effects of Surface Boundary Conditions

4.1 Introduction

Ocean models are forced at the surface by momentum and buoyancy sources from the atmosphere, through the wind stress, heat and freshwater fluxes respectively. Most eddy modelling studies have been carried out using a restoring condition for temperature as the surface boundary condition (e.g., Semtner and Mintz, 1977; Robinson et al., 1977; Cox, 1985; Bryan and Holland, 1989; Boning and Budich, 1992; Semtner and Chervin, 1988, 1992); some studies allow for a time and space dependent restoring coefficient (Han, 1984; Bryan and Holland, 1989). With the restoring condition on surface temperature, the model top layer temperature is restored to a specified equivalent atmospheric temperature on a time scale of 30 to 60 days. This condition is obtained by a linearization of the heat budget terms at the air-sea interface (Haney, 1971). Han (1984) gives empirical formulae to compute the spatially dependent distributions of the relaxation coefficient and the equivalent atmospheric temperature.

In this chapter, we examine an alternative treatment of the surface boundary condition, through the use of a zero heat capacity atmosphere. This is of potential

significance to eddy modelling, as the surface heat flux is important for the maintenance of midlatitude free jets (Huang, 1990; Ezer and Mellor, 1990).

Bretherton (1982) noted the mechanisms for damping sea surface temperature (SST) anomalies depend on the horizontal scale of these anomalies. For anomalies of scale of a few tens of kilometers or less, atmospheric heat transport plays a major role; the heat removed by the wind is returned to the ocean elsewhere on the surface of the earth. This mechanism damps SST anomalies on time scale of tens of days, as through the restoring condition. However, the damping for larger scale anomalies is likely to be radiative relaxation to space, as there is nowhere for heat to be advected and reabsorbed by the ocean. The loss to space occurs on the much longer time scale of hundreds of days.

A simple way to include a thermally interactive atmosphere is through a zero heat capacity atmosphere. This is based on the observation that the heat capacity of the atmosphere is much less than that of the ocean mixed layer (Dickinson, 1981). As an example, Schopf (1983) noted that the air-sea temperature difference in the tropics rarely exceeds 1 ^{0}C, even in areas with significant upwelling of cold water. He thus suggested the use of a zero heat capacity atmosphere to model heat exchanges between the atmosphere and the ocean. Recently, Deser and Blackmon (1993) show that surface air temperature is closely tied to sea surface temperature at midlatitude.

Zhang et al. (1993) coupled the zero heat capacity atmosphere of Schopf to their planetary geostrophic ocean model at non-eddy resolving horizontal resolution to re-examine the polar halocline catastrophe. The latter has previously been obtained using the restoring surface condition for temperature (Bryan, 1986; Weaver and Sarachik, 1991). Zhang et al. showed that allowing for the radiative damping to space of SST anomalies weakens considerably the feedback responsible for the catastrophe. They also noted that in reality, the atmospheric boundary condition seen by the ocean lies somewhere in between the two extremes of restoring condition and the zero heat capacity atmosphere. Cai et al. (1993) coupled the zero heat capacity atmosphere to a global ocean model to study interdecadal variability. The studies

of both Zhang et al and Cai et al are in the coarse resolution, non-eddy resolving regime.

A consideration of the surface temperature boundary condition relevant to eddy simulation is the possible over-restrictive nature of the restoring condition on the simulated surface temperature. The strict constraint of this surface boundary condition effectively removes eddy available potential energy near the sea surface, thus preventing the concentration of isotherms. This could reduce the midlatitude flow and damp baroclinic instability. It is thus of great interest to examine the effect of a zero heat capacity atmosphere on eddy simulation. By allowing for damping on the longer radiative time scales, the use of a zero heat capacity atmosphere could enhance surface temperature gradients, leading to a more realistic mid-latitude jet and eddy field.

4.2 A zero heat capacity atmosphere (ZHCA) model

The zero heat capacity atmospheric (ZHCA) model is taken from Schopf (1983), and it has been used by Zhang et al. (1993) and Cai et al. (1993) at coarse horizontal resolution to examine ocean-climate interaction. The governing equations of the model are

$$0 = -K(T_a - T_o) - K_r' T_a + Q_a \tag{4.1}$$

$$C_o \frac{\partial T_o}{\partial t} = K(T_a - T_o) + Q_o \tag{4.2}$$

Equation (4.1) represents the heat balance for the zero heat capacity atmosphere. T_o is the sea surface temperature, taken to be the same as the top model layer temperature, and T_a is the equivalent atmospheric temperature. The heat capacity of the ocean mixed layer is C_o; K is the heat exchange coefficient across the air-sea interface; K_r' is the atmospheric radiative feedback constant, and Q_a and Q_o denote atmospheric and

oceanic heat sources not explicitly represented in the equations, such as advection. The above equations can be combined as (Zhang et al., 1993),

$$C_o \frac{\partial T_o}{\partial t} = K_r(T_r - T_o) + Q_o \tag{4.3}$$

where

$$T_r = \frac{Q_a}{K_r'} \tag{4.4}$$

$$K_r = \frac{K K_r'}{K + K_r'} \tag{4.5}$$

To compare with the results of Chapter 3 obtained using a restoring condition, we identify the 5-year mean heat flux (FLUX) as one component of the surface forcing in the ZHCA model, the other component being given by a relaxation on the radiative time scale to the 5-year mean surface temperature T_1, as follows:

$$\begin{aligned} K_r(T_r - T_o) &= K_r(T_r - T_1) + K_r(T_1 - T_o) \\ &= K(T_A - T_1) + K_r(T_1 - T_o) \\ &= FLUX + \frac{(T_1 - T_o)}{\tau_R} \end{aligned} \tag{4.6}$$

Note that the restoring term in Equation (4.6) has the same form as the conventional restoring boundary condition. However, the restoring time scale $\tau_R = K_r^{-1}$ here is several hundred days, and is much longer than the several tens of days typical of the conventional restoring condition.

4.3 Results with $\Delta x = \Delta y$=40 km horizontal resolution

A number of experiments have been performed at a horizontal resolution of $\Delta x = \Delta y$=40 km, in order to determine the effects of different surface temperature boundary conditions. The surface forcings are same as in Chapter 3. The lateral boundary

conditions used are no slip. A preliminary experiment with the restoring boundary condition has the restoring time scale doubled from 30 to 60 days. An overall increase in the temperature variance $\overline{T'^2}$ is obtained, but its vertical distribution is largely unchanged, with the maximum amplitude at subsurface levels near the thermocline. This is consistent with the results of Boning and Budich (1992), who used a restoring time scale of 50 days and obtained a similar vertical distribution.

For the rest of the experiments, we switch to the ZHCA model by diagnosing the 5-year mean surface heat flux and surface temperature distributions as surface forcing in Equation (4.6). The vertical distributions of temperature variance can now have maxima at the surface, subsurface levels, or both, depending on geographical location. This is more consistent with observations (Wunsch, 1983). However, K' (eddy kinetic energy) magnitude at the surface does not increase, despite the less constraining nature of the ZHCA model compared to the restoring condition. This is because there is now more energy in the small scale eddies, which are in turn dissipated by the highly scale selective biharmonic friction. The horizontal biharmonic diffusivity coefficients are then reduced by a factor of 2.5, resulting in an enhanced level of K', compared to that of the restoring condition. However, the fields appear more noisy at the same time. The horizontal resolution is thus increased to $\Delta x = \Delta y$=30 km. Limitations of computing resources do not permit higher resolutions.

In the rest of this chapter, we compare results obtained with the ZHCA model and the restoring condition, at a horizontal resolution of 30 km. Horizontal and vertical distributions of eddy quantities are examined. Before proceeding to the results, we note that the use of a pure flux condition, i.e., without the restoring term in Equation (4.6), produces the largest temperature variance. It also gives large amplitude oscillations. This pure heat flux boundary condition has been used by Zhang et al (1993) and Greatbatch and Zhang (1993) at non-eddy resolving scales. Further investigation of this phenomenon is beyond the scope of this thesis. We also note that even though the eddy scale is much smaller than the basin scale, it is the baroclinic instability of the midlatitude jet that gives rise to eddies. The latter has a scale comparable to the

basin, and it is thus of great interest to examine the effect of the ZHCA model on the jet and the resulting eddies.

The model is first run to statistical steady state using a 40 km resolution with a restoring surface boundary condition on temperature. The variables are then interpolated to the higher resolution (30 km) points; the latter model is run for 10 years using the restoring condition to statistical equilibrium. The mean surface heat flux for the last 5 years, with a sampling interval of 3 days, is diagnosed for use in the ZHCA model. The diffusive coefficients are shown in Table 4.1.

4.4 Results with $\Delta x = \Delta y$=30 km: Horizontal distributions

Figure 4.1 shows the surface heat flux and temperature distributions for use in the ZHCA model, and the simulated surface temperature distribution. The latter is not as constrained by the prescribed surface temperature as in the case of restoring condition. Indeed, the mean temperature in the ZHCA model has more longitudinal variation.

Figure 4.2 shows the temperature variance at the surface (25 m) and subsurface (250 m) levels, for both the restoring condition and ZHCA model. The latter consistently yields a larger variance at the surface with enhanced eastward extension of the high variance region from the western boundary current into the open ocean. This is an important diagnostic as the eddy available potential energy is equal to the temperature variance normalized by the mean stratification. Both cases show a comparable maximum temperature variance of 9.6 $^{\circ}C^2$ at the the 250 m level, but the larger eastward extension is still evident for the ZHCA model. This simulated maximum variance is comparable to observations (Emery, 1983). Both cases underestimate the variability downstream of the current in the northeastern part of the domain compared to observations (Emery, 1983), but the ZHCA model does have stronger variability. This suggests that a higher horizontal resolution is needed with

lower diffusivities to get better quantitative agreement.

Stammer and Boning (1992) compared the surface elevation anomalies simulated by the CME model (Bryan and Holland, 1989) with GEOSAT analyses of surface variability. There is good agreement near the Gulf Stream, but the model elevations are small downstream of the Gulf Stream and in the subpolar gyre. As the radius of deformation decreases poleward, the underestimation of mesoscale variability in the subpolar gyre is mainly due to insufficient horizontal resolution. Indeed, a doubling of the resolution leads to more eddy variability enhancement in the subpolar gyre than in the subtropical gyre (Boning and Budich, 1992).

Figure 4.3 shows the eddy kinetic energy K' at surface and subsurface levels, for restoring condition and the ZHCA model. The distributions obtained with the former are generally similar to the simulations of Cox (1985), and Boning and Budich (1992). The current observational estimates of K' are based on ship drift measurements (Wyrtki et al., 1976), drifting buoys (Richardson, 1983) and GEOSAT altimetry (Le Traon et al., 1990; Stammer and Boning, 1992). These estimates generally agree on the overall K' pattern, but not on the magnitudes due to the different smoothing used in the studies. Treguier (1992) and Stammer and Boning (1992) found the CME model underestimates K' at midlatitude near the axis of maximum K', and in the eastern Northern Atlantic. Our results show that a larger K' in the northeastern part of the basin is simulated using the ZHCA model compared to restoring condition. This increase is due to resolved baroclinic instability, which in turn is due to the less constraining surface condition of the ZHCA model. In the western boundary current region, the magnitudes for the two cases are about the same. The increase in K' is not as pronounced as the increase in temperature variance examined in Figure 4.2 as the horizontal resolution is still not high enough; the small scale eddies are thus still effectively dissipated by the highly scale selective frictions. However, we also note that there is an increased conversion of K' to $\overline{K}$ (mean kinetic energy) for the ZHCA model; this aspect will be examined in more detail in the next chapter.

Figure 4.4 shows the distribution of $\overline{K}$. The ZHCA model gives larger values

of $\overline{K}$ in the midlatitude open ocean and the subpolar gyre, as well as an increased eastward extension of the zonal bands. The simulated mean flow has a maximum $\overline{K}$ of about 100 cm^2s^{-2} near the north equatorial current, 4000 cm^2s^{-2} near the western boundary current, and 20 cm^2s^{-2} in the open ocean free jet. A minimum is found in the centre of the subtropical gyre. This overall pattern agrees with the observational estimates of Wyrtki et al. (1976). The $\overline{K}$ is however underestimated in the separation region; this is not surprising as topography is not included in our model, and primitive equation models are known to have difficulties in this area (Bryan and Holland, 1989; Treguier, 1992; Boning and Budich, 1992). Our main point here is that the use of the ZHCA model provides a mechanism to increase both $\overline{K}$ and K' levels, and an enhanced eastward extension of mesoscale variability and mean flow into the eastern North Atlantic. Boning and Budich (1992) found that the eastward extension of K' and $\overline{K}$ have different responses to the increase of horizontal resolutions; the eastward extension of K' was increased substantially for the finer resolution, while the eastward extension of $\overline{K}$ did not change correspondingly. This is in contrast to the QG model result of Barnier et al. (1991). One of the possible reasons is the strong damping effect of diffusion in PE models (Holland and Batteen, 1986). Indeed, our results suggest that the eastward extension of $\overline{K}$ and K' can be increased by relaxing the surface temperature condition through the ZHCA model.

4.5 Results with $\Delta x = \Delta y$=30 km: Vertical distributions

Figure 4.5 shows the domain averaged temperature and mean kinetic energy distributions. There is little change between the ZHCA model and the restoring condition for the temperature field. This means any difference in the temperature variance reflects differences in the eddy available potential energy, as the latter is the temperature variance normalized by the mean stratification. The domain averaged $\overline{K}$ is slightly larger near the surface in the ZHCA case, as an increased amount of mean potential energy

is converted into mean kinetic energy, and the negative viscosity (energy conversion from $\overline{K}$ to K') is also stronger in the ZHCA model. A more detailed discussion of the mean momentum balance will be presented in the next chapter.

Figure 4.6 shows the variation of the temperature variance with depth for the subtropic and subpolar gyres. The main difference between the restoring condition and ZHCA model results is in the upper several hundred metres of the ocean, with the latter giving much larger values. The profiles do not differ much below this level.

The temperature variance shows a maximum at about 400 m in the subtropic gyre for both restoring and ZHCA cases, which is associated with the thermocline. This is expected for eddy resolving models with the restoring condition (Boning and Budich, 1992), but the ZHCA model also gives a subsurface maximum due to mesoscale displacement of the thermocline. For the latter, a weaker secondary maximum is also found at the surface, consistent with some observational studies of POLYMODE moorings in the subtropical regions (Fu et al., 1982). Three different profiles of temperature variance are possible in the North Atlantic, depending on the location (Fu et al., 1982; Wunsch, 1983). The maxima can be found at the surface, subsurface levels, or both. Emery et al. (1980) analysed the multiship surveys in the area between 29 and 42^{0}N in the North Pacific and North Atlantic oceans, and found many eddy signatures in the sea surface temperature field. For the subpolar gyre, the ZHCA model gives a maximum temperature variance at the surface, while the restoring condition has the maximum at subsurface levels. The ZHCA model results may be more consistent with the fact that the meridional temperature distribution shows no clear thermocline in the subpolar gyre of the model.

Figures 4.7 and 4.8 show the vertical distributions of K' and the baroclinic conversion $\overline{w'T'}$ for both gyres. K' is larger in the ZHCA case than in the restoring case in both gyres. The increase is most pronounced near the surface, as for the temperature variance examined earlier. The higher K' in the ZHCA case is due to enhanced baroclinic instability, as shown by the distribution of the vertical heat transport by the time varying flow (Figure 4.8). As measured by this diagnostic, the baroclinic

instability of the subpolar gyre is enhanced in the upper ocean through the use of the ZHCA model, but the maximum remains at a subsurface level. This is unlike the case for the temperature variance, where the maximum in the subpolar gyre is located at the surface for the ZHCA case. A possible reason is the use of the rigid top boundary condition, which sets the vertical velocity to zero at the surface (Note the top level in Figure 4.8 is 25 m, i.e., the mid-point of the first model layer).

As mentioned earlier, Treguier (1992), Stammer and Boning (1992) compared the mesoscale variability in the CME model (Bryan and Holland, 1989) with estimates from GEOSAT altimetry. They found that the model systematically underestimates the amplitude of the variability; they also note that the leading mechanism in generating eddy variability is baroclinic instability. Our results show that the use of the ZHCA model, instead of the more conventional restoring condition, can produce stronger eddies when sufficient horizontal resolution is used.

The general increase in the eddy kinetic and available potential energies obtained through the use of the ZHCA model can be summarized in Figure 4.9, which shows the zonally averaged distributions. We see a clear increase in the eddy energies in the upper ocean in midlatitudes and in the subpolar gyre. The zonally averaged meridional heat tranports for the ZHCA model and restoring condition have also been evaluated (Figure 4.10). The transports by the mean flow and the eddies, and hence the total transport, are not much affected by the ZHCA model.

4.6 Summary

The effects of the ZHCA model have been compared to the more conventional restoring condition. The former, being less constraining than the latter in terms of the surface temperature, allows more mesoscale variability and a stronger mean flow near midlatitudes and in the subpolar regions. Our results suggest that the use of the ZHCA model is one way to increase mesoscale variability through a strengthened

midlatitude jet in eddy resolving models. For example, the CME model underestimates such variability in the eastward extension region of the Gulf Stream and in the subpolar gyre (Stammer and Boning, 1992; Treguier, 1992). Another important result is that stronger $\overline{K}$ is found in the eastward extension region of the Gulf Stream in the ZHCA model. This is especially relevant as Boning and Budich (1992) found that the $\overline{K}$ eastward extension is not sensitive to the horizontal resolution.

The vertical distributions of temperature variance obtained with the ZHCA model show maxima at the surface, subsurface level, or both, depending on geographical location. In contrast, the results we have obtained with the restoring condition all show a temperature variance maximum below the surface. The vertical heat transport by the time varying flow, which converts eddy available potential energy (P') to eddy kinetic energy (K'), is also increased in the ZHCA model. The use of a constant heat flux and a restoring time scale appropriate for radiative damping in the ZHCA model permits the simulated sea surface temperature to depart more from the reference temperature, and allows advection to play a larger role in the surface heat balance.

Table 4.1: A summary of the dissipative parameters used in the numerical experiments. Negative values of A_{MH} and A_{HH} refer to biharmonic diffusion, with units of $cm^4\ s^{-1}$; all other parameters have units of $cm^2\ s^{-1}$.

Case	levels	A_{MH}	A_{HH}	A_{MV}	A_{HV}	λ
Fine resolution $\Delta x = \Delta y$=30 km						
1. no slip	14	-2×10^{18}	-1×10^{19}	20	0.5	2×10^8
2. no slip	14	-2×10^{18}	-1×10^{19}	20	0.5	2×10^8

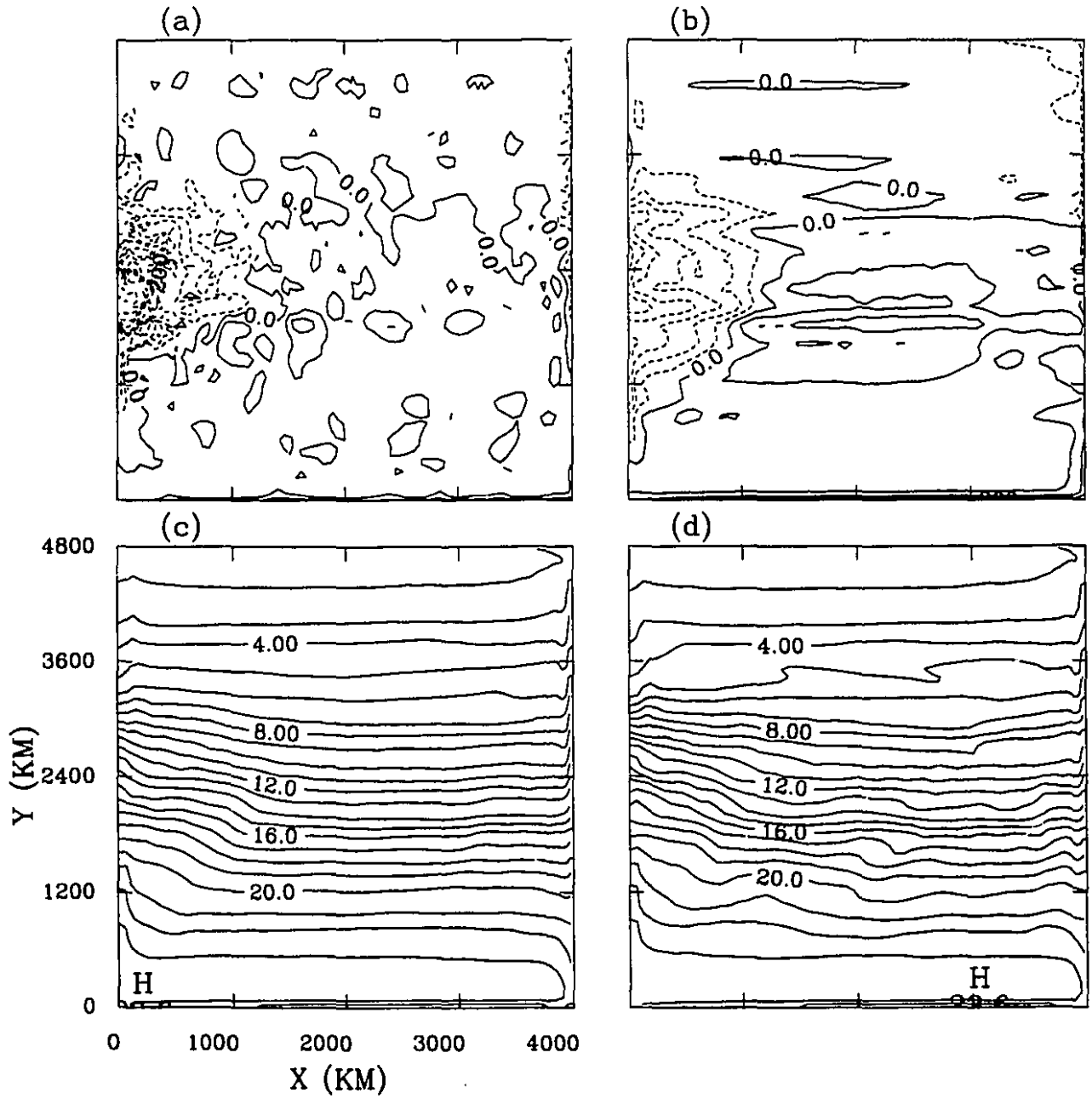

Figure 4.1: The horizontal distribution: a typical surface instantaneous heat flux (a; C.I.= 100 W/m^2), 5-year mean surface heat flux (b; C.I.= 50 W/m^2) and 5-year mean surface temperature (c; °C), all obtained with the restoring condition on surface temperature. 5-year mean surface temperature with a ZHCA model is shown in (d; °C).

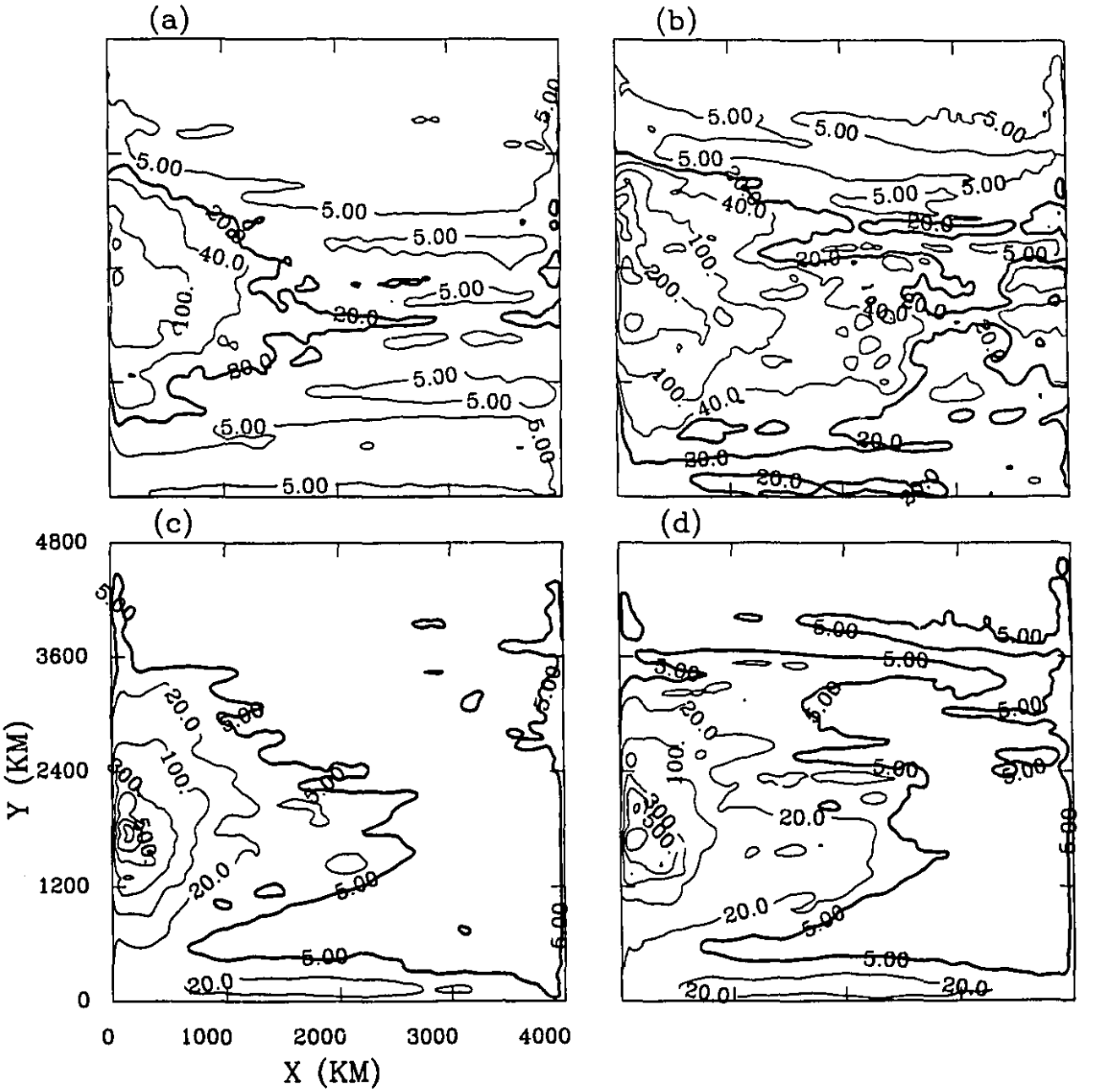

Figure 4.2: The 5-year mean temperature variance ($10^{-2} \times °C^2$) at $Z = 25$ m for the restoring condition (a) and ZHCA model (b). The corresponding distributions at $Z = 250$ m are shown as (c) and (d) respectively. Note the magnitude of the temperature variance in the figures were multiplied by a factor of 100.

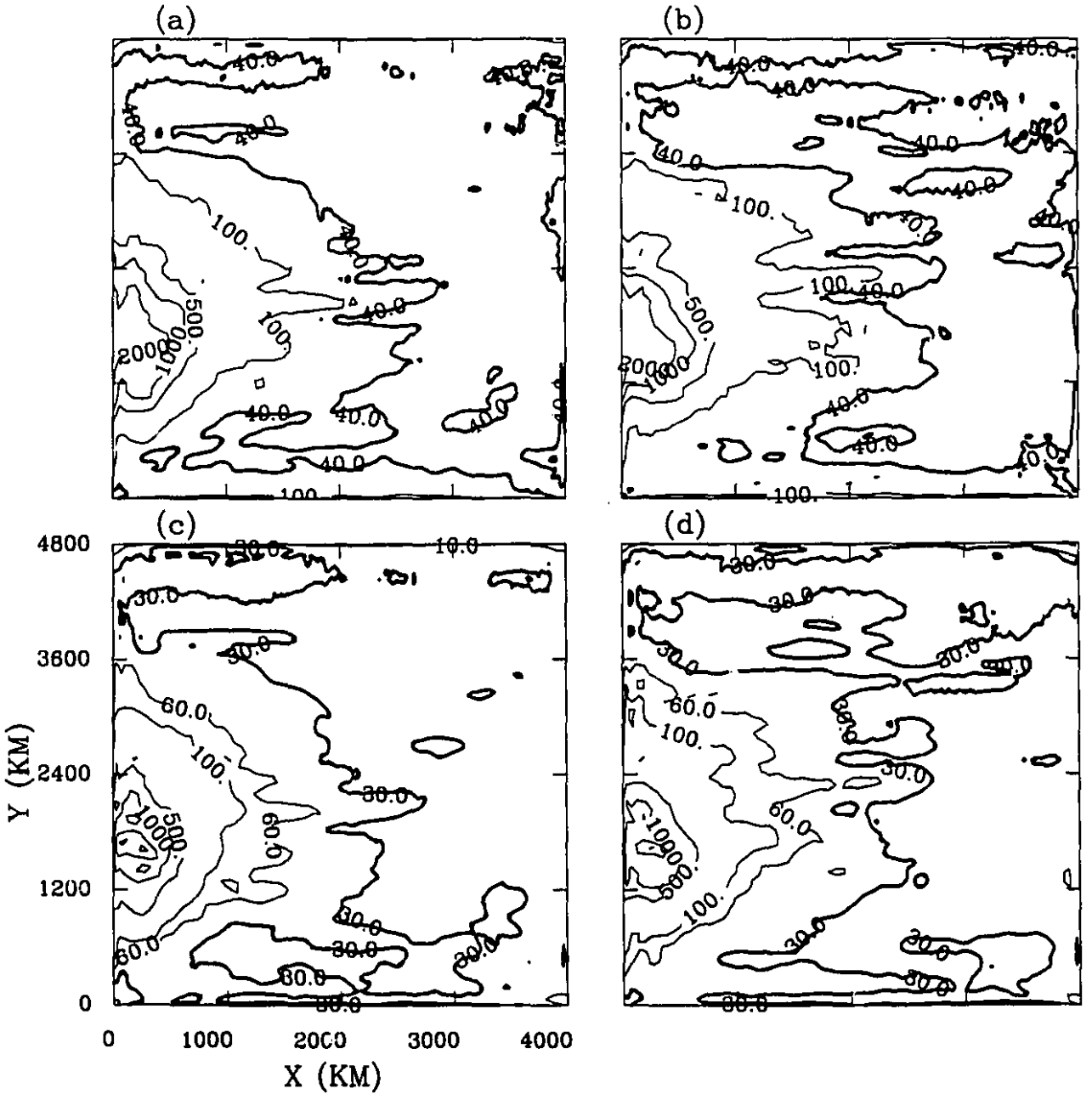

Figure 4.3: The 5-year mean eddy kinetic energy (K'; cm^2 s^{-2}) at Z = 25 m for the restoring condition (a) and ZHCA model (b). The corresponding distributions at Z = 250 m are shown as (c) and (d) respectively.

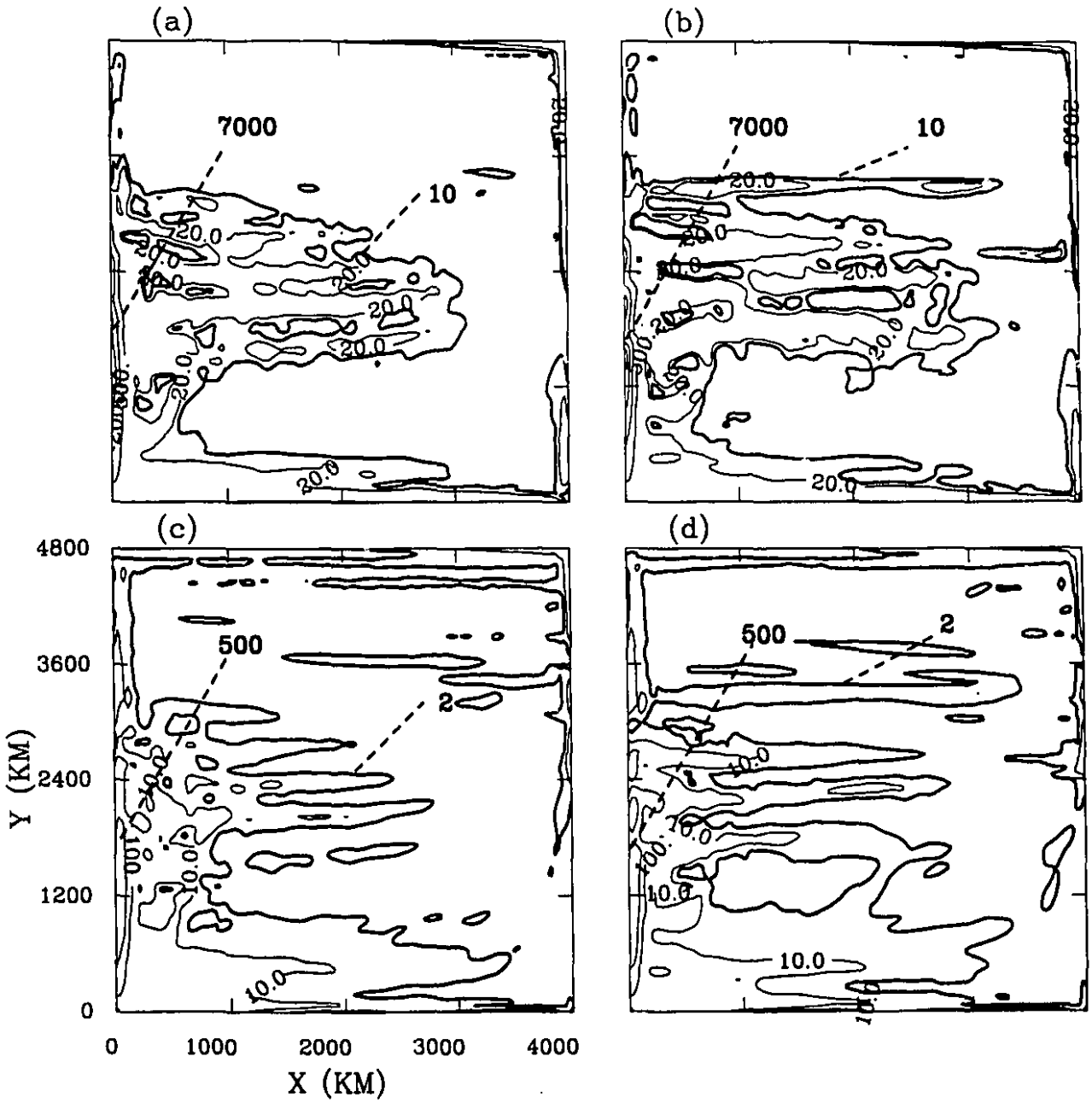

Figure 4.4: The 5-year mean kinetic energy ($\overline{K}$; cm^2 s^{-2}) at $Z = 25$ m for the restoring condition (a) and ZHCA model (b). The corresponding distributions at $Z = 250$ m are shown as (c) and (d) respectively.

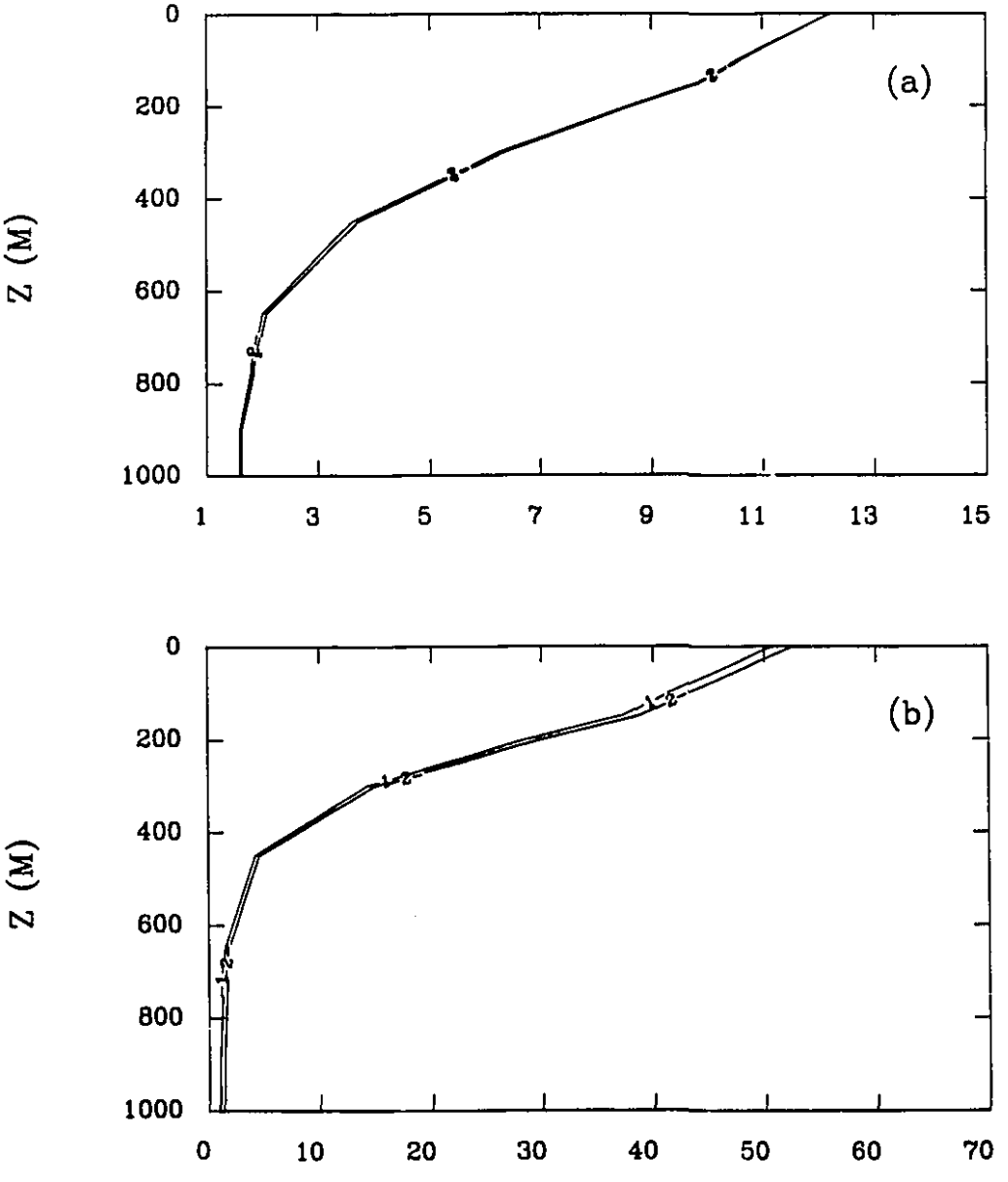

Figure 4.5: The vertical distribution of the domain-averaged 5-year mean temperature (a; °C) and domain-averaged mean kinetic energy ($\overline{K}$; b; $cm^2\ s^{-2}$), for the restoring condition (Curve 1) and the ZHCA model (Curve 2).

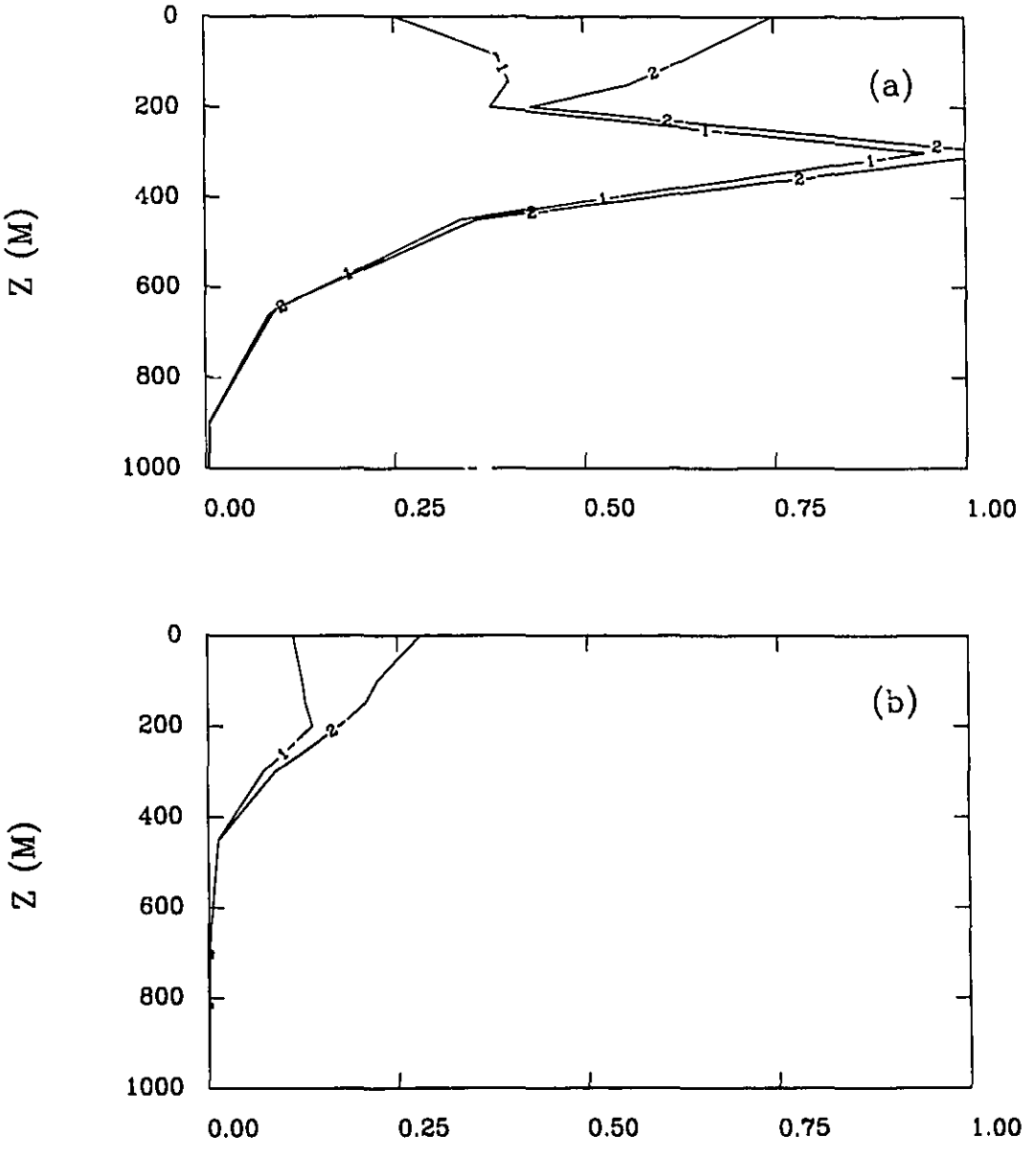

Figure 4.6: The vertical distribution of the 5-year mean temperature variance ($°C^2$) for the subtropical (a) and subpolar (b) gyres, for the restoring condition (Curve 1) and the ZHCA model (Curve 2).

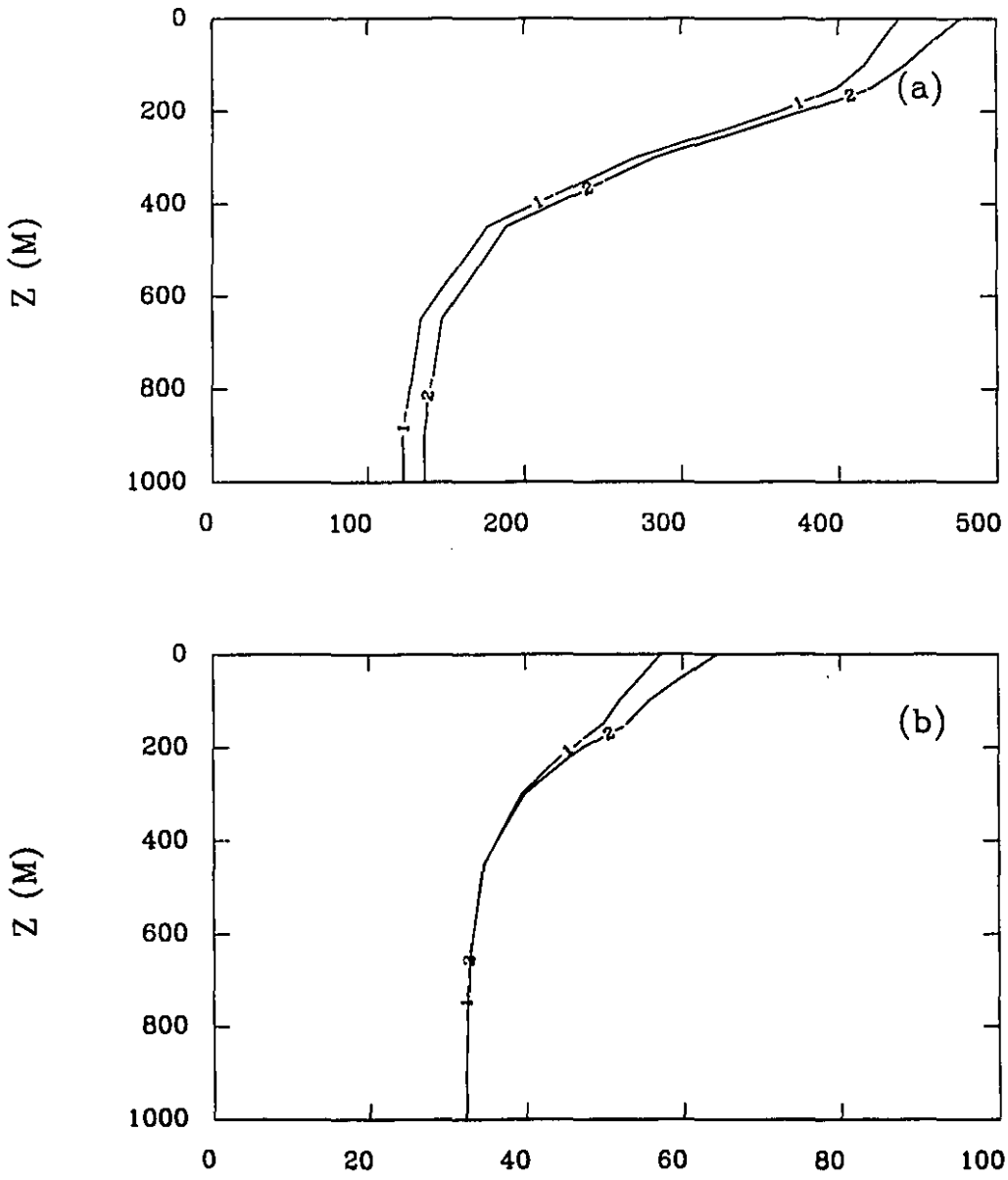

Figure 4.7: The vertical distribution of the 5-year mean eddy kinetic energy (K'; cm^2 s^{-2}) for the subtropical (a) and subpolar (b) gyres, for the restoring condition (Curve 1) and the ZHCA model (Curve 2).

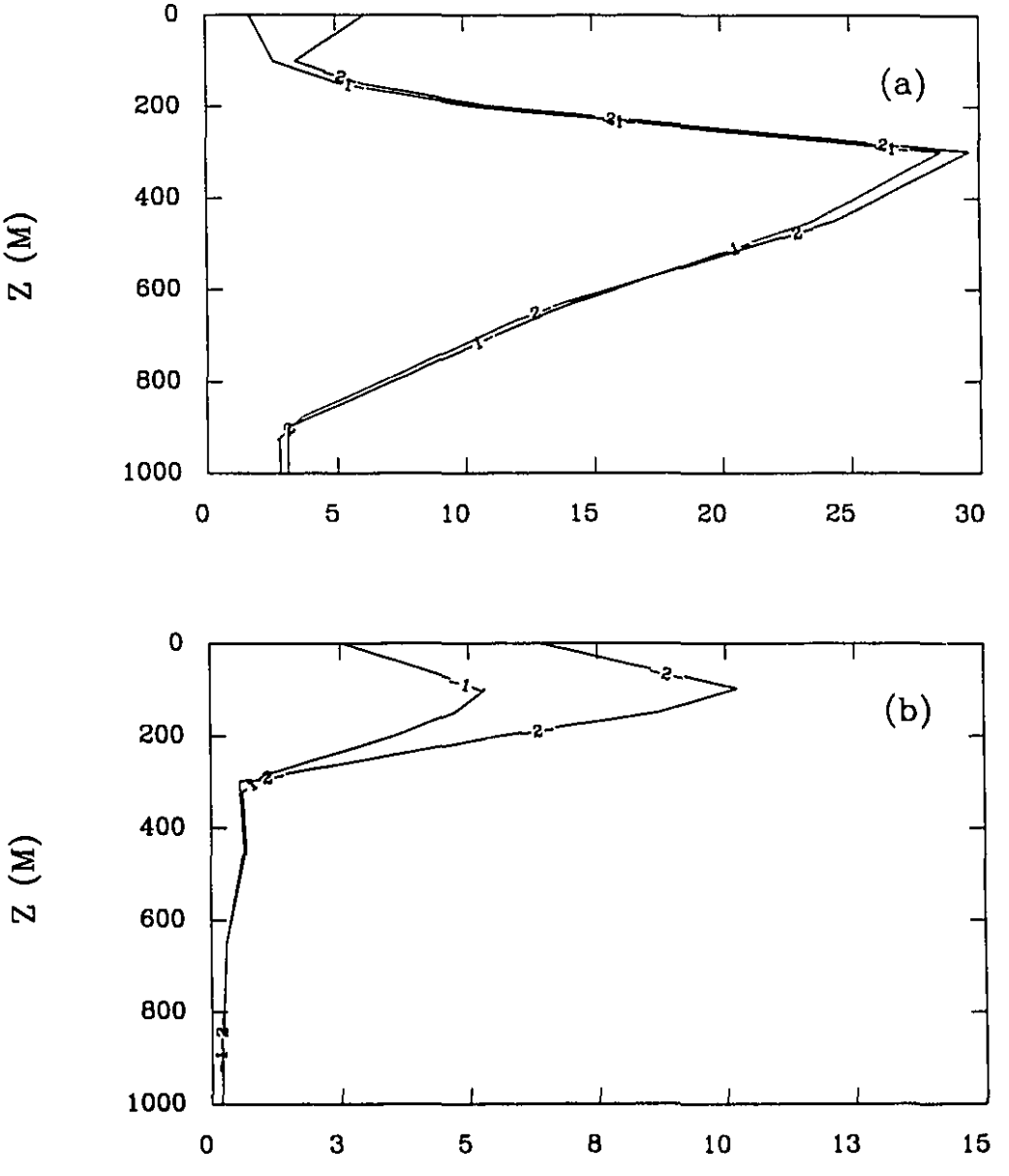

Figure 4.8: The vertical distribution of the 5-year mean vertical heat transport ($\overline{w'T'}$; $10^{-5} \times$ °C cm s^{-1}) for the subtropical (a) and subpolar (b) gyres, for the restoring condition (Curve 1) and the ZHCA model (Curve 2).

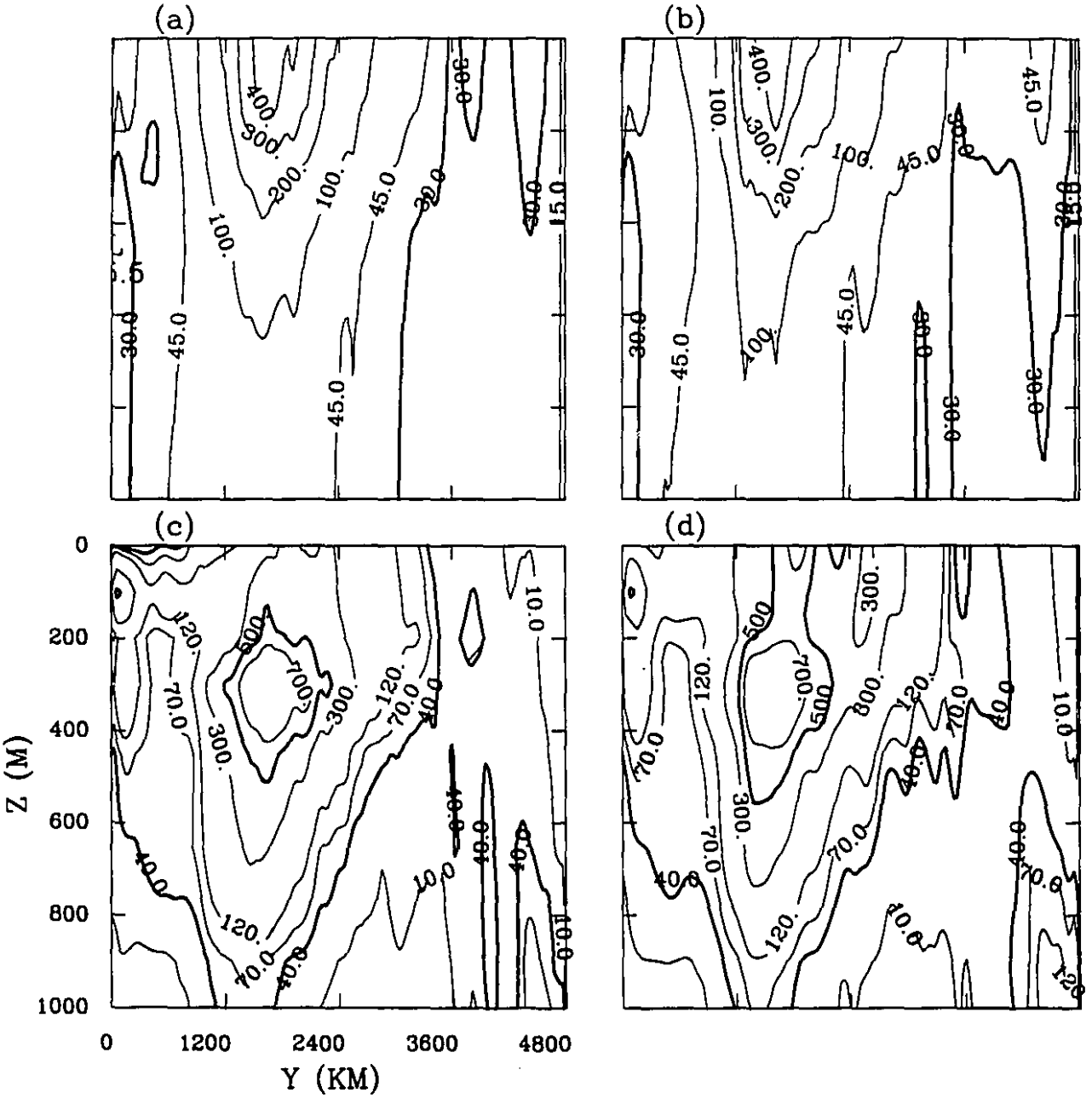

Figure 4.9: Meridional section of the 5-year mean zonally averaged eddy kinetic energy ($cm^2\ s^{-2}$) for (a) restoring condition; (b) the ZHCA model. The corresponding eddy available potential energy ($cm^2\ s^{-2}$) are shown in (c) and (d) respectively.

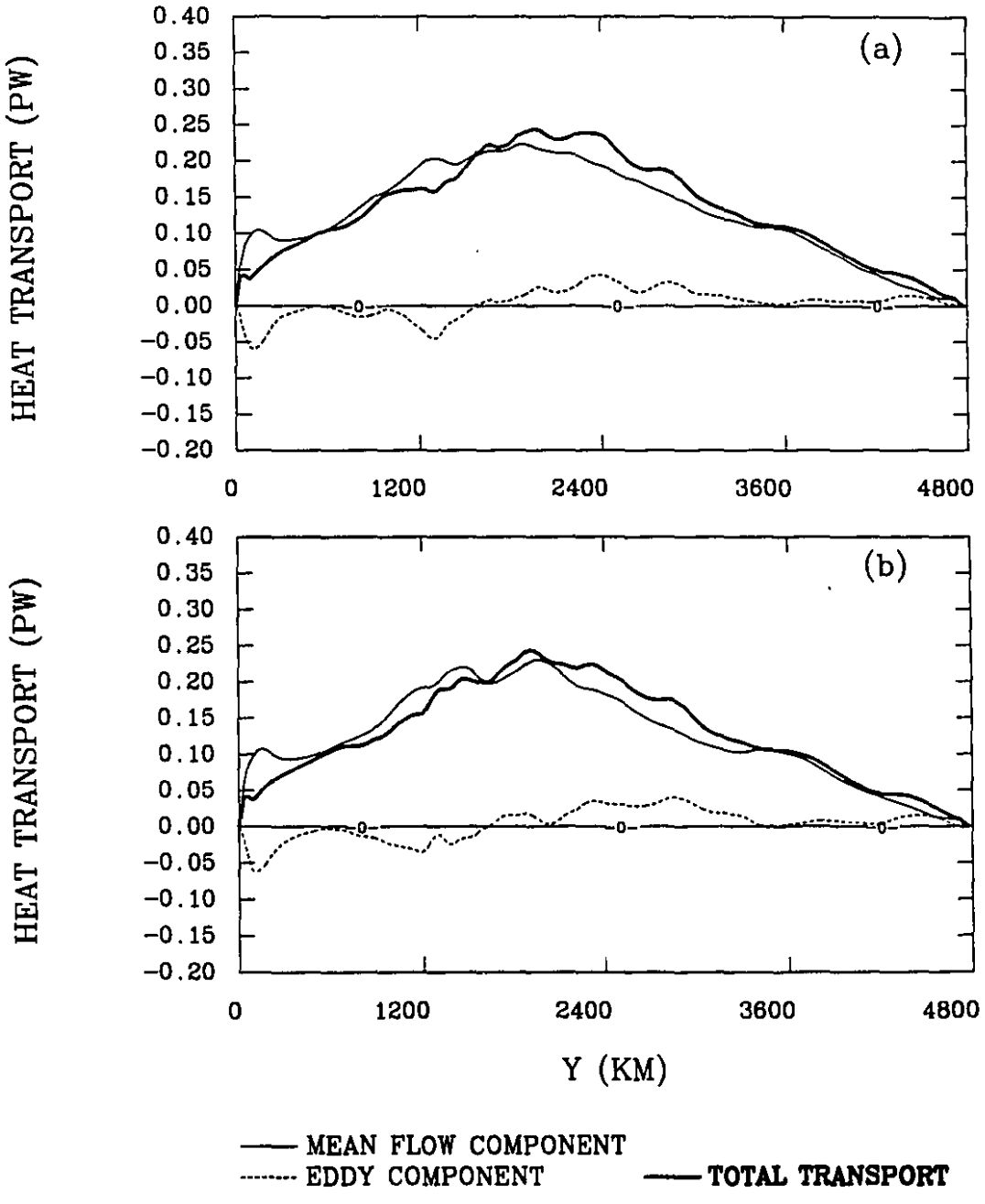

Figure 4.10: The 5-year mean northward heat transport (PW= 10^{15} watts) for: (a) restoring condition; (b) the ZHCA model.

Chapter 5

Maintenance of Midlatitude Free Jets

5.1 Introduction

Yoshida (1970) reported evidence of long zonal bands with a meridional scale of about 300 km in the zonal-component of the flow within the southwestern part of the North Pacific subtropical gyre. Richman et al. (1977), using moored current meter data taken during MODE I, found that their low frequency band is dominated by zonal velocity fluctuations, primarily confined to the thermocline. Rossby et al. (1983), Krauss and Boning (1987) obtained larger zonal than meridional diffusivities from observational data. These observational features were also found in primitive equation (PE) models with resolved eddies (Cox, 1987; Boning and Cox, 1988; Boning, 1989; Semtner and Chervin, 1992). The meridional scale of the zonally orientated bands can be explained by the theory of geostrophic turbulence, it is given by (Rhines, 1975; 1977),

$$k_y = (\frac{\beta}{2U})^{\frac{1}{2}} \tag{5.1}$$

where k is the meridional wavenumber, β the meridional gradient of Coriolis parameter, and U the root-mean-square particle velocity.

The eddy's effect on the mean circulation has been mainly investigated using quasi-geostrophic (QG) models (Holland and Rhines, 1980; Harrison, 1982; Harrison and Holland, 1981; Greatbatch, 1987) and barotropic models (e.g., Marshall, 1984). Harrison and Semtner (1986) compared QG and PE model simulations and pointed out it is important to examine the effects of eddies on the mean circulation in PE models with both wind-driven and thermohaline circulations. The momentum and vorticity balances in PE models have been discussed qualitatively by Robinson et al. (1977).

In this chapter, we examine the effects of eddies on the maintenance of midlatitude jets and its sensitivity to horizontal resolution and surface thermal boundary conditions, using both the mean momentum and vorticity equations. All the time mean are averaged over 5-year period. Section 2 discusses the flow fields in both the upper and deep ocean. Section 3 shows the mean momentum equations and the effects of eddies. Section 4 presents an analysis of the mean vorticity equation. The summary and conclusion are presented in Section 5.

5.2 The model and experiments

The model used in this Chapter is the same as described in the previous Chapters. The experimental design is summarised in Table 5.1.

Figures 5.1(a) and (b) show typical instantaneous and time mean flows of the second layer (Z = 75 m) and 12th layer (Z = 2800 m) for NO1 with $\Delta x = \Delta y$= 40 km (Henceforth, we will refer to the second layer as the upper ocean and the 12th layer as the deep ocean). The strong mean currents in the upper ocean are near the southern boundary which corresponds to the North Equatorial Current, and the subtropical extent of the western boundary which corresponds to the western boundary current. Significant eddy activity can be seen near intense currents from the instantaneous flow field, including the western boundary current and its outflow regions. As in the top layer shown in Chapter 3, there is also a signature of the thermahaline circulation

driven by the specified thermal forcing at the surface, producing northward flow along the subpolar extent of the western boundary layer (Cox, 1985; Boning, 1989). This is similar to the northward branch of Gulf Stream (Reynaud et al., 1994). In the deep ocean, the eddy activity is still very strong (note the change in scale of the deep ocean velocities). The western boundary current flows southward in the deep ocean.

Figures 5.1(c) and (d) show the mean flow for NO1 for the upper and deep ocean respectively. There is a clear signature of zonal bands in the mean flow fields, as shown in other PE simulations (Cox, 1987; Boning, 1989; Bryan and Holland, 1989; Semtner and Chervin, 1992). There are differences in the zonal bands in the deep ocean for different simulations. Boning (1989) showed that random topography can remove much of the zonality in the deep ocean, and at the same time leaving the flow above the thermocline unchanged. However, in Semtner and Chervin's (1992) global simulation with realistic topography, the zonality of the mean flow is still present. We will thus examine the effects of eddies on the maintenance of midlatitude jets for both the upper and deep ocean.

Figures 5.2 and 5.3 show typical instantaneous flow and time mean flow of NO2 and NO3 with $\Delta x = \Delta y = 30$ km. The flow fields are similar to those of NO1, except the eddy signature and the mean zonal bands are stronger due to the use of either higher horizontal resolution or the ZHCA model.

5.3 Mean momentum equations

In order to study the effect of eddies on the mean state, we decompose the dependent variables into the time mean and its deviation, denoted by an overbar and prime respectively,

$$u = \overline{u} + u'; v = \overline{v} + v'; p = \overline{p} + p'; w = \overline{w} + w' \tag{5.2}$$

Substituting Equation (5.2) into the u-momentum equation and taking the time

average, we obtain the mean zonal momentum equation:

$$\frac{\partial \overline{u}}{\partial t} - fv + \frac{1}{\rho_0}\frac{\partial \overline{p}}{\partial x} = -\nabla \cdot (\overline{\vec{V}}\,\overline{u}) - \nabla \cdot \overline{\vec{V}'u'} + others \qquad (5.3)$$

This equation represents the acceleration of the mean zonal flow. The terms shown on the left side of the equation are the tendency, Coriolis and pressure gradient terms respectively; the first and the second terms on the right side of the equation are the mean and eddy advection respectively. The dissipative terms and vertical advection are not explicitly included, and will not be discussed further. They are either small or represent dissipative effects in the open ocean; we are mainly interested in the relative role of eddies and mean advection in maintaining and increasing the midlatitude jets.

Figure 5.4 shows the mean zonal velocity at $Z = 75$ m averaged between $X = 900$ km and 1500 km, away from the western boundary current. The mean zonal velocity maximum increases from NO1 to NO3. The increase of the mean zonal flow at midlatitudes due to the use of a higher horizontal resolution has been studied in QG models by Barnier et al. (1991). The zonal bands have a meridional scale of about 400 km, consistent with the estimate given by Equation (5.1), with $U = 5$ cm s^{-1}. Figure 5.5 shows the mean zonal velocity at $Z = 2800$ m. The magnitude is now much weaker than at the upper ocean, but the meridional scale of the zonal bands are similar. However, there are alternate eastward and westward zonal bands, in contrast to the upper ocean, where the zonal flow is consistently eastward at midlatitudes.

Holland and Schmitz (1985) found in QG models that there is a subtle balance between the inertial character of the flow, which tends to cause the eastward flowing thin jet to extend far to the east, and an opposite tendency due to the instability of the jet, which tends to limit its eastward extension. In PE models (Bryan and Holland, 1989; Boning and Budich, 1992), the simulated midlatitude jets are usually much weaker than those of observations and QG models (Treguier, 1992). Therefore, it is important to investigate physical processes which may increase the midlatitude free jets. The geostrophic terms usually represent the leading order balance in the momentum equations (Robinson et al., 1977), and will not be discussed here. Indeed, the importance of the geostrophic terms does not mean eddies are not important

(Rhines, 1975; 1977). We thus examine the effect of eddies on the maintenance and variation of midlatitude free jet for different horizontal resolutions and top boundary conditions.

Figure 5.6 shows the mean zonal momentum eddy convergence and advection terms in the upper ocean. The eddy convergence can increase the eastward zonal flow at midlatitudes (negative viscosity). Consistent with earlier results, the effect of eddies increases with either increased horizontal resolution or the use of the ZHCA model. The mean advection is negligible compared to eddy momentum convergence. The enhanced mean zonal momentum eddy flux at higher horizontal resolution was noted by Boning and Budich (1992) in PE models. It is however interesting to note that NO3 has a better organized positive eddy momentum convergence pattern compared to NO2. Similar zonal eddy momentum flux convergence patterns have been found over the Kuroshio Extension (Nishida and White, 1982; Schmitz et al., 1982; Tai and White, 1990) and the Gulf Stream Extension (Schmitz, 1977). The recent analysis of Geosat altimeter data (Ikeda, 1993) suggests that eddy-eddy interactions play a role in accelerating/decelerating the North Atlantic Current when the latter varies slowly. Wood (1988) showed, using an idealized PE models of Gulf Stream meander, baroclinic instability as the main source for transients and a tendency for the eddy momentum flux to reinforce the mean flow. Our results demonstrate the sensitivity of this effect to both horizontal resolution and surface thermal boundary conditions.

Figure 5.7 shows the mean zonal momentum eddy convergence and advection terms in the deep ocean. The eddy convergence is one order smaller than in the upper ocean. Again, the effect of eddies increases with the increased horizontal resolution. However, the use of the ZHCA model does not have a significant effect in the deep ocean. Another difference from the upper ocean is that the eddy momentum convergence no longer has a preference to accelerate the eastward zonal flow.

The eddy momentum convergence was also computed for the mean meridional momentum equation; they can be either negative or positive (figures not shown).

Therefore eddies should be able to shift the mean flow jets northward or southward.

Before closing this section, we present an estimate of the relaxation time scale of the surface layer mean free jet due to eddies, i.e., the time required for eddies to produce a given free jet acceleration.

$$\frac{\partial \overline{u}}{\partial t} = -\nabla \cdot \overline{\vec{V}'u'}$$

Assuming a typical value of $-\nabla \cdot \overline{\vec{V}'u'}$ as 3×10^{-7} cms^{-2}, it takes about 180 days to produce a free jet increase of $\Delta u = 5$ cm s^{-1}. Thus eddy forcing can well induce variations of midlatitude free jets. Preliminary examination of a one year record from satellite altimetry seems to suggest the existence of a seasonal cycle in the intensity of both the surface transport and the eddy field in the Kuroshio and Gulf Stream extensions (Tai and White, 1990).

The effect of eddies on the north-south shift of the mean midlatitude jet can be examined in a similar manner.

$$\frac{\partial \overline{v}}{\partial t} = -\nabla \cdot \overline{\vec{V}'v'}$$

If we take $-\nabla \cdot \overline{\vec{V}'v'} = 1 \times 10^{-6}$ cm/s^2, an initially steady midlatitude jet with no north-south velocity will be displaced through eddies about 200 km in 180 days.

5.4 Mean vorticity equation

In order to study the effect of eddies on the mean circulation, the vorticity equation should be more useful than the momentum equations. Geostrophic adjustment occurs on a time scale of f^{-1}, and thus the momentum and continuity equations should be considered simultaneously on time scales larger than f^{-1}. The vorticity equation is thus a more appropriate tool to analyse the maintenance of the mean circulation.

We note that the mean flow is quasi-geostrophic. Thus the vorticity equation can be written as

$$\frac{\partial \overline{\zeta}}{\partial t} = -\beta \overline{v} - f \nabla \cdot \overline{\vec{V}} - \nabla \cdot (\overline{\vec{V}}\overline{\zeta}) - \nabla \cdot (\overline{\vec{V}'\zeta'}) + others \qquad (5.4)$$

where $\overline{\zeta}$ is the mean relative vorticity, and ζ' is the fluctuating relative vorticity. The first two terms in the right hand side of Equation (5.4) (mean advection of planetary vorticity and stretching terms) will be referred to as the "geostrophic terms". The third term is the mean vorticity advection, and the fourth term is the eddy vorticity flux. The remaining terms are again not explicitly included. We will concentrate on the relative importance of the geostrophic terms, eddy vorticity convergence and mean vorticity advection.

We start by defining different Rossby numbers for the mean and eddy flow in the momentum and vorticity equations,

$$\begin{aligned} R_0 &= U/f_0L \\ R'_0 &= U'/f_0L \\ R_{V0} &= U/\beta L^2 \\ R'_{V0} &= U'/\beta L^2 \end{aligned}$$

Here, R_0 and R'_0 are the Rossby number and eddy Rossby number defined using the momentum equations. The corresponding Rossby numbers defined using the the mean vorticity equation are R_{V0} and R'_{V0} respectively. The former Rossby numbers are smaller than the latter for scales

$$L \leq f_0/\beta$$

which is about 5000 km. Thus even though the Rossby number may be very small in the momentum equations, its counterpart in the vorticity equations may be larger.

Robinson et al. (1977) found that Ekman drifts are important in the top and bottom layers, which are strongly dependent on the specificed wind stress and bottom friction respectively. We examine the second and twelfth layers.

Figure 5.8 shows the contribution of different terms to the vorticity balance in the second layer from different components for NO1. The geostrophic terms are generally still the leading terms, but the effects of eddies and mean advection are also important. The horizontal and vertical frictions are usually smaller than the eddy and mean advection terms (figures not shown).

Figure 5.9 shows the vorticity balance terms for NO2 in the upper ocean. We can see that the mean vorticity ($\overline{\zeta}$) is larger, and the contribution of eddy vorticity convergence and mean vorticity advection become more important due to the increased horizontal resolution. Indeed, they are now comparable to the $\beta\overline{v}$ term. In addition, the eddy vorticity convergence is larger than the mean vorticity advection. These results are consistent with previous studies (Holland and Lin, 1975a; Robinson et al., 1977; Holland and Rhines, 1980; Harrison and Holland, 1981).

Figure 5.10 shows the vorticity balance terms for NO3. The mean vorticity, and the maximum contributions of the eddy vorticity convergence and mean vorticity advection are even larger than those for NO2. The distribution of positive and negative eddy vorticity flux are now more closely aligned with the corresponding mean vorticity extrema. This means eddies now play a stronger role in maintaining the mean circulation, due to the less constraining nature of the ZHCA model as the surface thermal boundary condition.

Figure 5.11 shows the vorticity balance terms for NO1 in the deep ocean. The mean advection term is now negligible compared to the eddy vorticity convergence term. The geostrophic terms can be balanced by the eddy vorticity convergence, with possibly dissipation as well. With the increase of horizontal resolution (Figure 5.12), eddies become more important, and the eddy vorticity convergence becomes more comparable to the geostrophic terms (Holland and Lin, 1975a; Robinson et al., 1977; Holland and Rhines, 1980; Harrison and Holland, 1981). As expected, the ZHCA model does not have a significant effect in the deep ocean (Figure 5.13).

5.5 Summary and conclusion

The mean momentum and vorticity equations have been used to examine the effect of eddies and mean advection on the mean circulation. The main results can be summarised as follows.

In the momentum equation, the zonal eddy momentum convergence is usually

larger than the mean advection. Eddy momentum convergence tends to increase the midlatitude free jets in the upper ocean, but there is no such preference in the deep ocean. The effects of the eddy momentum convergence on the mean zonal flow increases with either the use of higher horizontal resolution or the ZHCA model.

In the mean vorticity equation, the geostrophic terms are still the leading order balance terms in the upper ocean for the 40 km horizontal resolution (NO1). However, the effect of eddy vorticity convergence and mean vorticity advection become comparable to the geostrophic terms with 30 km horizontal resolution. Eddy vorticity convergence is usually larger than mean vorticity advection. The eddy vorticity convergence with ZHCA (NO3 case) is not only larger than the NO2 case with the same horizontal resolution, but the negative and positive convergence centers also have a better correlation with the extrema of mean vorticity. In the deep ocean, the mean advection term is negligible, but dissipation may be required for vorticity balance for the NO1 case. For both NO2 and NO3 cases, the eddy vorticity convergence is comparable to the geostrophic terms. In contrast to the upper ocean, the case of the ZHCA model does not lead to a significant change in the deep ocean.

Table 5.1: A summary of the numerical experiments. All experiments use the no slip condition with 14 vertical levels.

Case	$\Delta x = \Delta y$	surface boundary condition	Source
NO1	40 km	restoring	Chapter 3
NO2	30 km	restoring	Chapter 4
NO3	30 km	ZHCA	Chapter 4

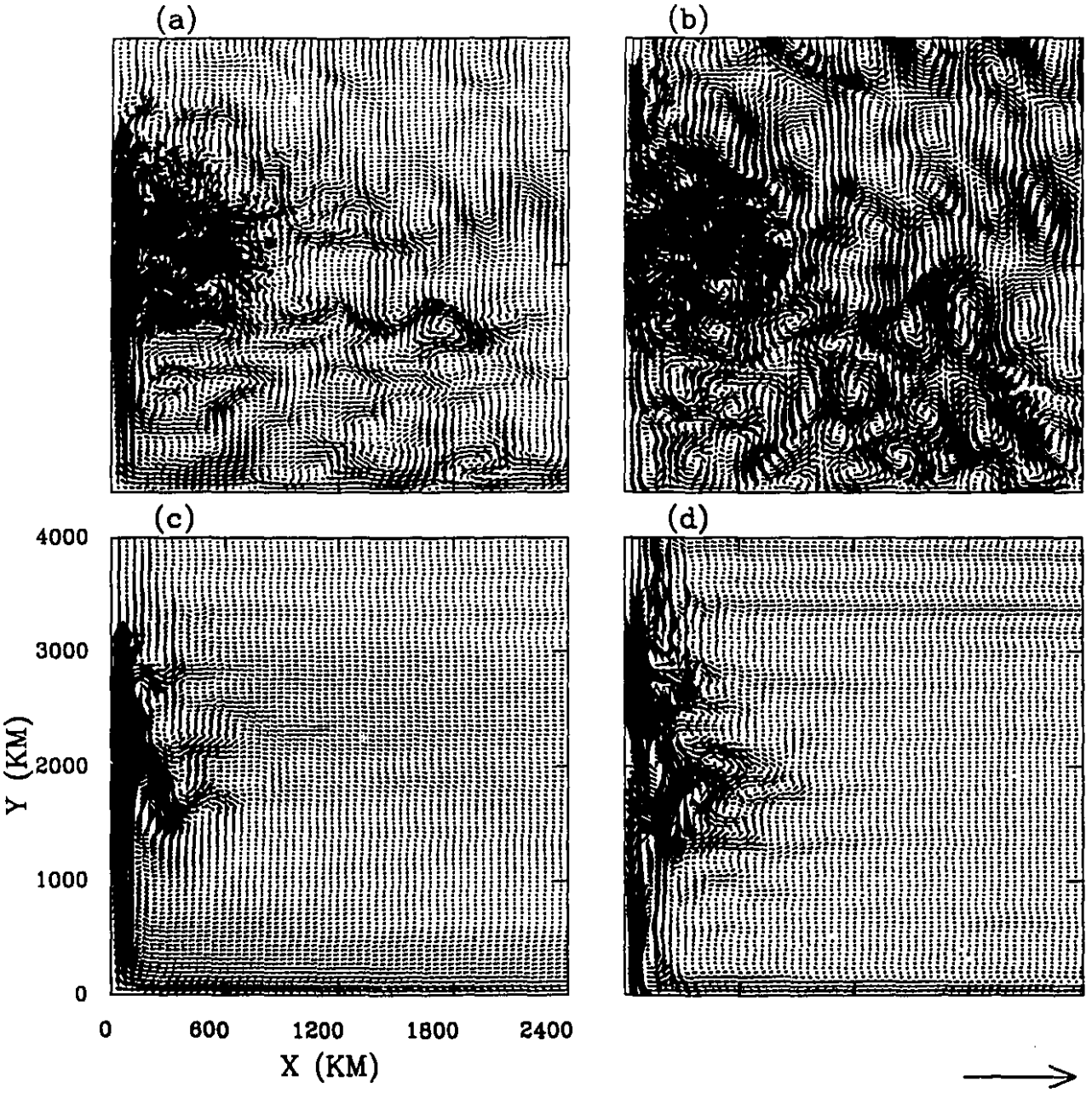

Figure 5.1: The instantaneous horizontal velocity distribution for NO1 (cm s^{-1}) at depths (a) $Z = 75$ m (178.0), and (b) $Z = 2800$ m (42.1). The 5-year mean horizontal velocity are shown as (c) $Z = 75$ m (139.0), and (d) $Z = 2800$ m (12.3). The magnitudes corresponding to the vector shown at the bottom right is given between parentheses.

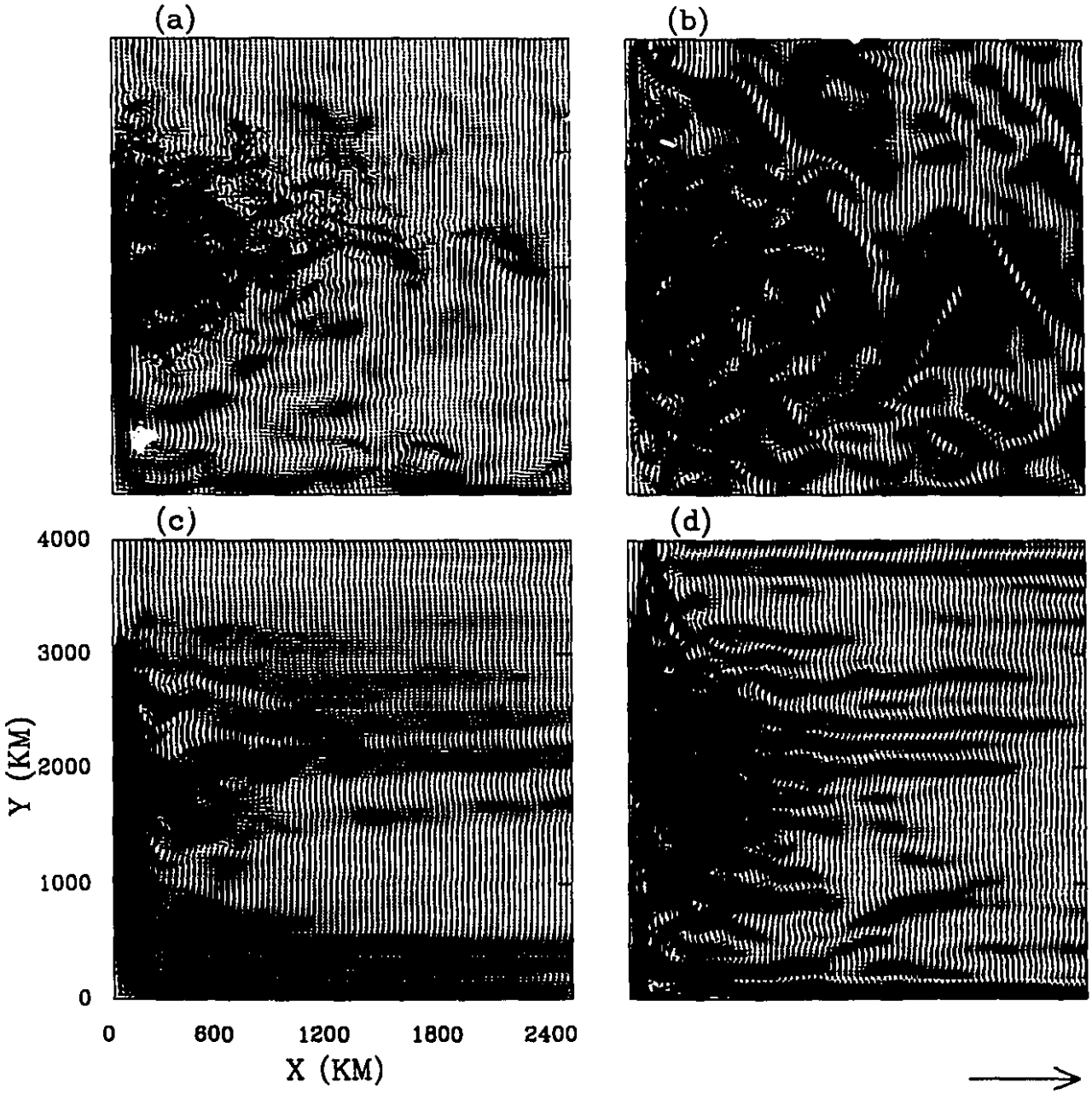

Figure 5.2: The instantaneous horizontal velocity distribution for NO2 (cm s^{-1}) at depths (a) $Z = 75$ m (257.0), and (b) $Z = 2800$ m (66.9). The 5-year mean horizontal velocity are shown as (c) $Z = 75$ m (113.0), and (d) $Z = 2800$ m (12.6). The magnitudes corresponding to the vector shown at the bottom right is given between parentheses.

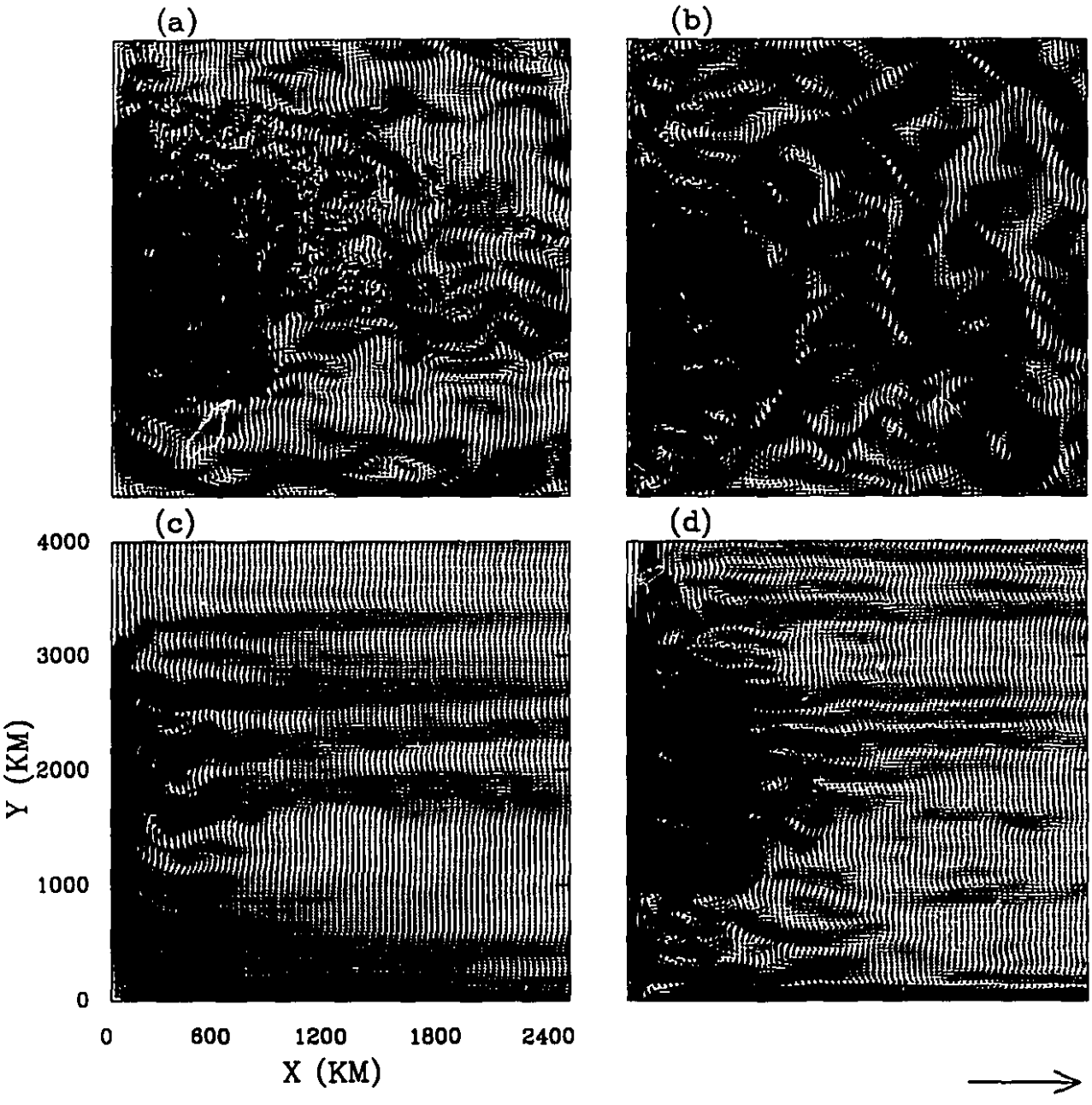

Figure 5.3: The instantaneous horizontal velocity distribution for NO3 (cm s^{-1}) at depths (a) $Z = 75$ m (177.0), and (b) $Z = 2800$ m (64.9). The 5-year mean horizontal velocity are shown as (c) $Z = 75$ m (122.0), and (d) $Z = 2800$ m (12.3). The magnitudes corresponding to the vector shown at the bottom right is given between parentheses.

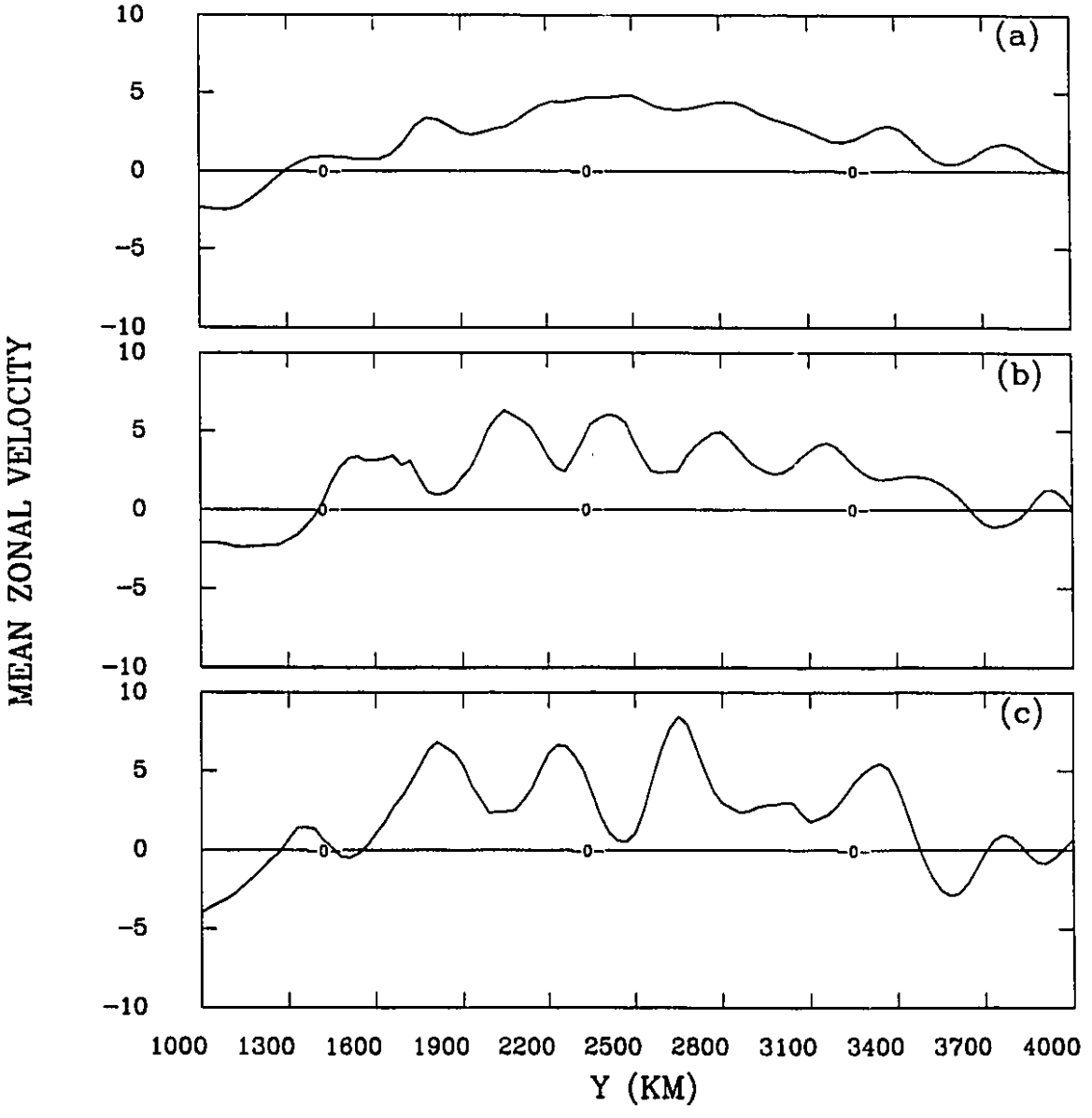

Figure 5.4: The 5-year mean zonal velocity at $Z = 75$ m, averaged between $X = 900$ and 1500 km for (a) NO1; (b) NO2; (c) NO3. The unit is cm s^{-1}.

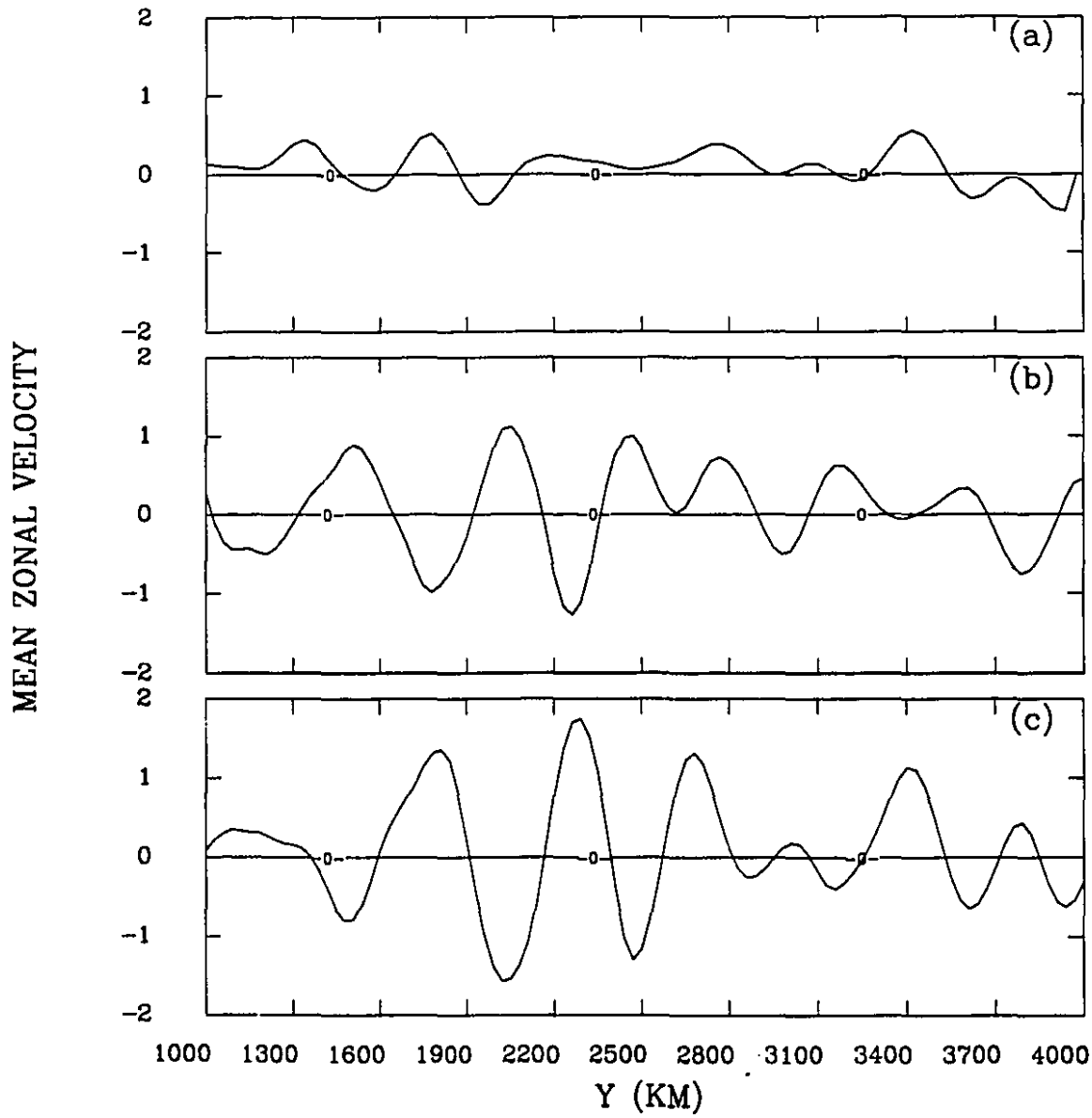

Figure 5.5: Same as Figure 5.4 but at $Z = 2800$ m.

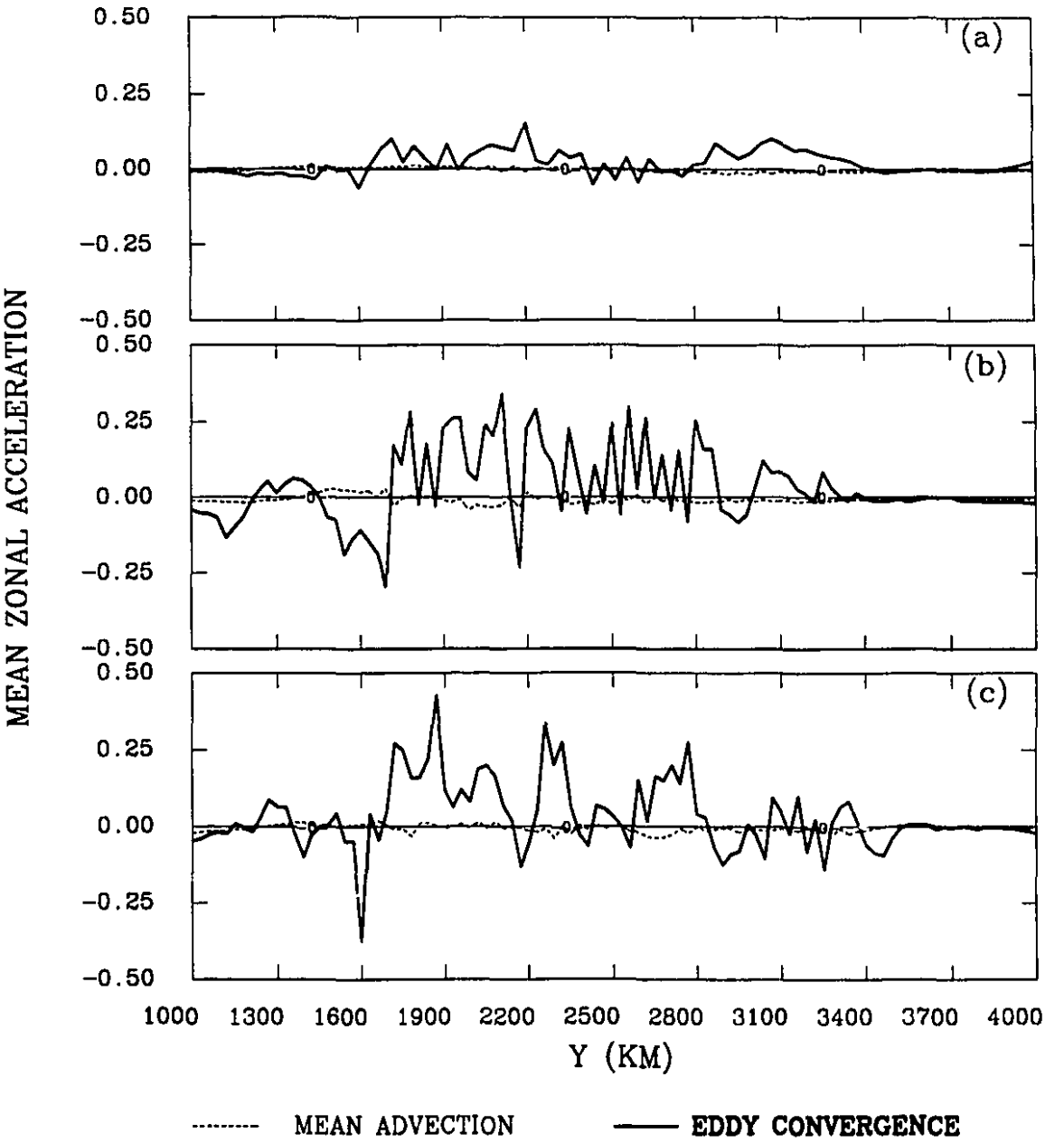

Figure 5.6: The 5-year mean zonal eddy momentum convergence and advection terms, averaged between $X = 900$ and 1500 km, at $Z = 75$ m, for (a) NO1; (b) NO2; (c) NO3. The unit is 10^{-6} cm s^{-2}.

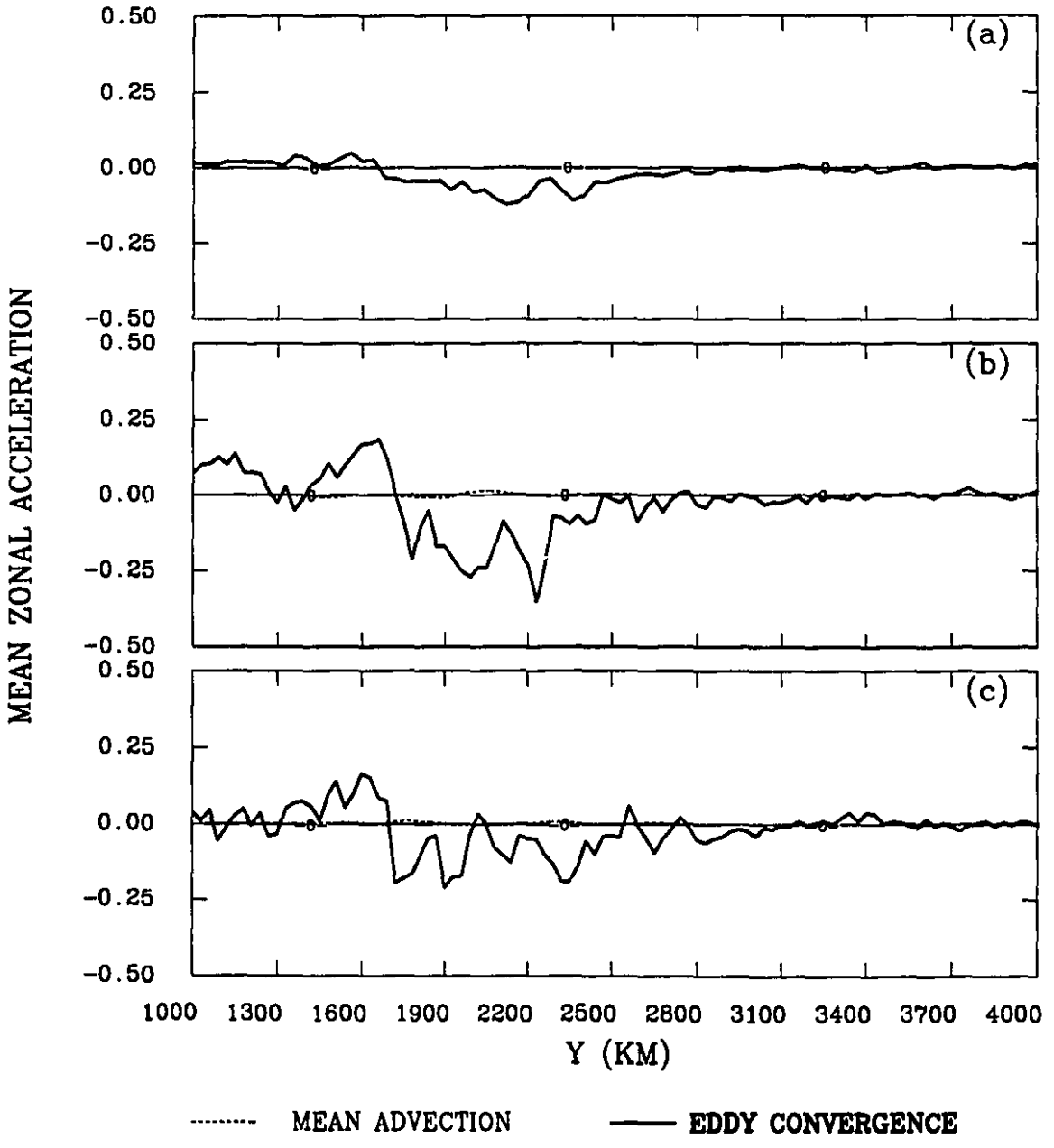

Figure 5.7: Same as Figure 5.6 but at $Z = 2800$ m.

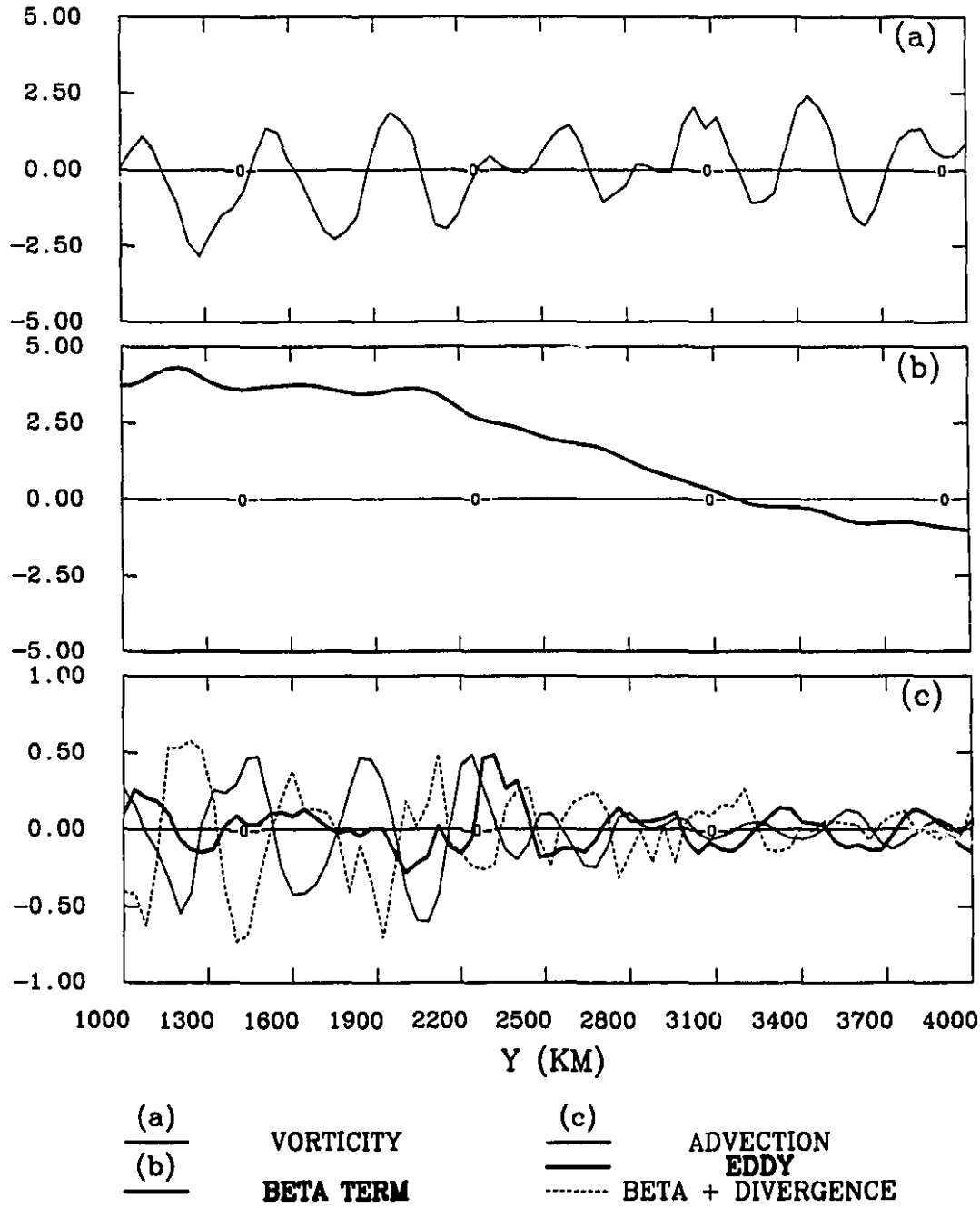

Figure 3.8: The 5-year mean zonally averaged terms of the vorticity equation at $Z = 75$ m for NO1. (a) mean vorticity (10^{-7} s^{-1}); (b) β-term (10^{-13} s^{-2}); (c) residual of geostrophic balance (BETA+DIVERGENCE), mean vorticity advection (ADVECTION) and eddy vorticity convergence (EDDY), all in units of 10^{-13} s^{-2}.

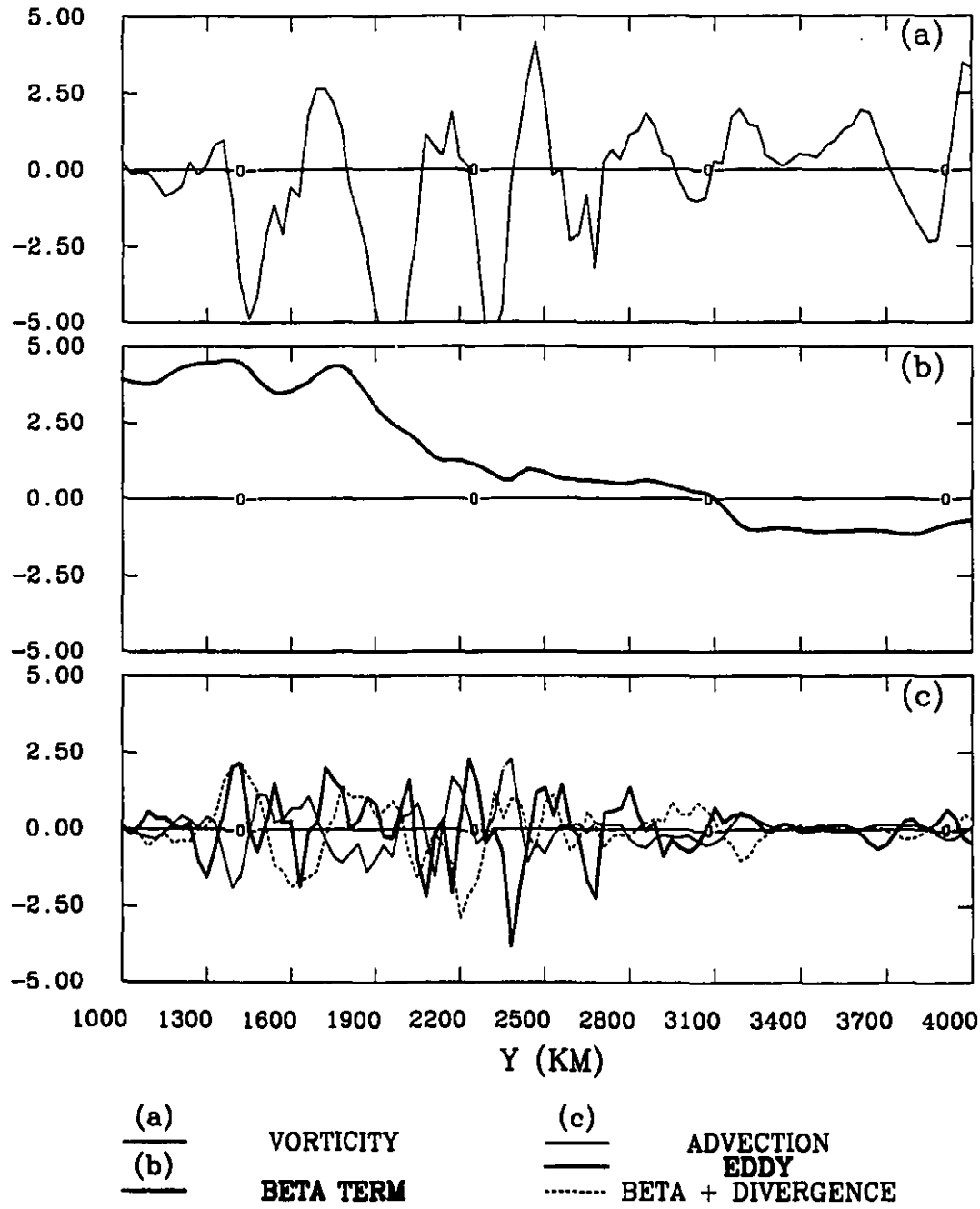

Figure 5.9: The 5-year mean zonally averaged terms of the vorticity equation at Z = 75 m for NO2. (a) mean vorticity (10^{-7} s^{-1}); (b) β-term (10^{-13} s^{-2}); (c) residual of geostrophic balance (BETA+DIVERGENCE), mean vorticity advection (ADVECTION) and eddy vorticity convergence (EDDY), all in units of 10^{-13} s^{-2}.

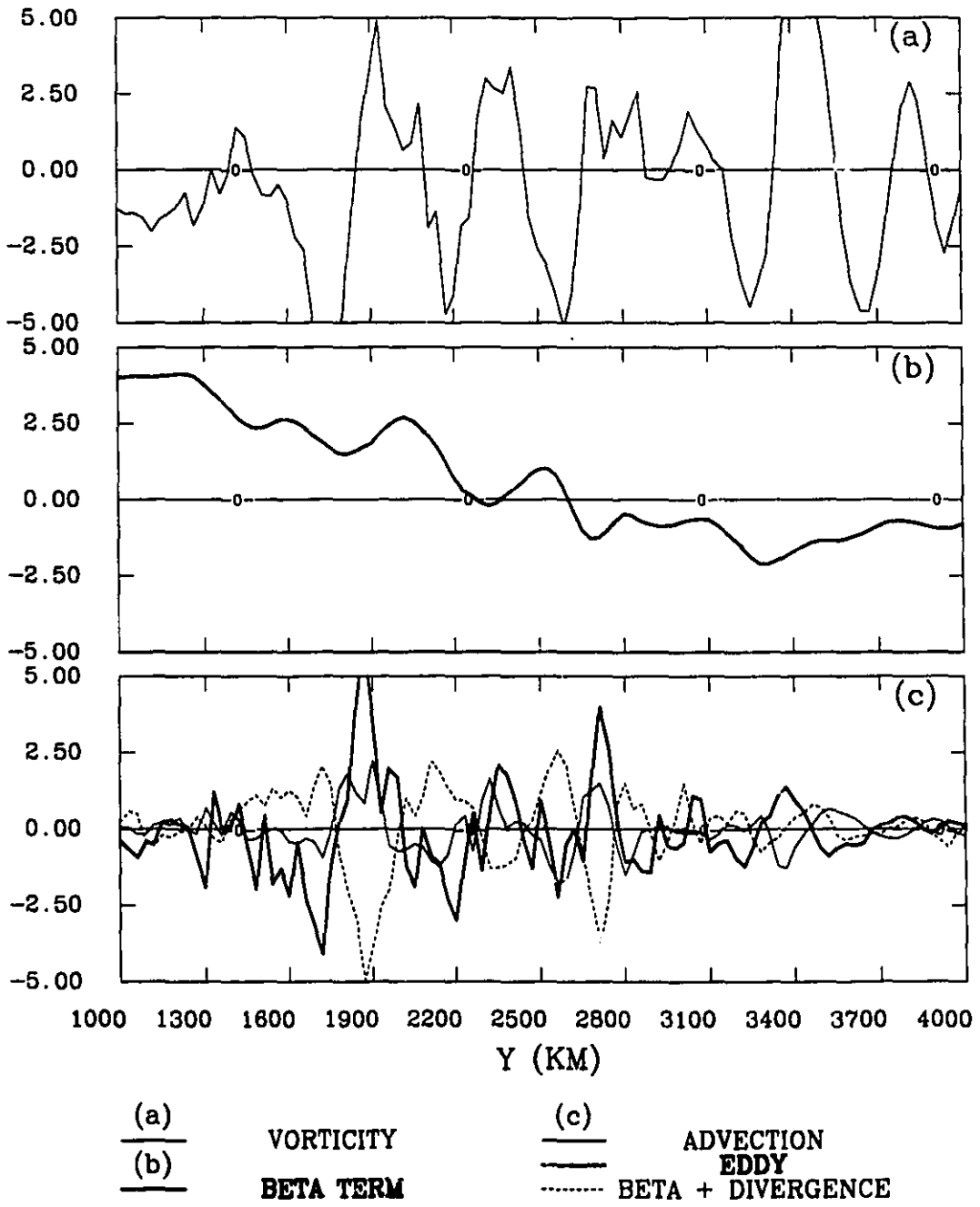

Figure 5.10: The 5-year mean zonally averaged terms of the vorticity equation at $Z = 75$ m for NO3. (a) mean vorticity (10^{-7} s^{-1}); (b) β-term (10^{-13} s^{-2}); (c) residual of geostrophic balance (BETA+DIVERGENCE), mean vorticity advection (ADVECTION) and eddy vorticity convergence (EDDY), all in units of 10^{-13} s^{-2}.

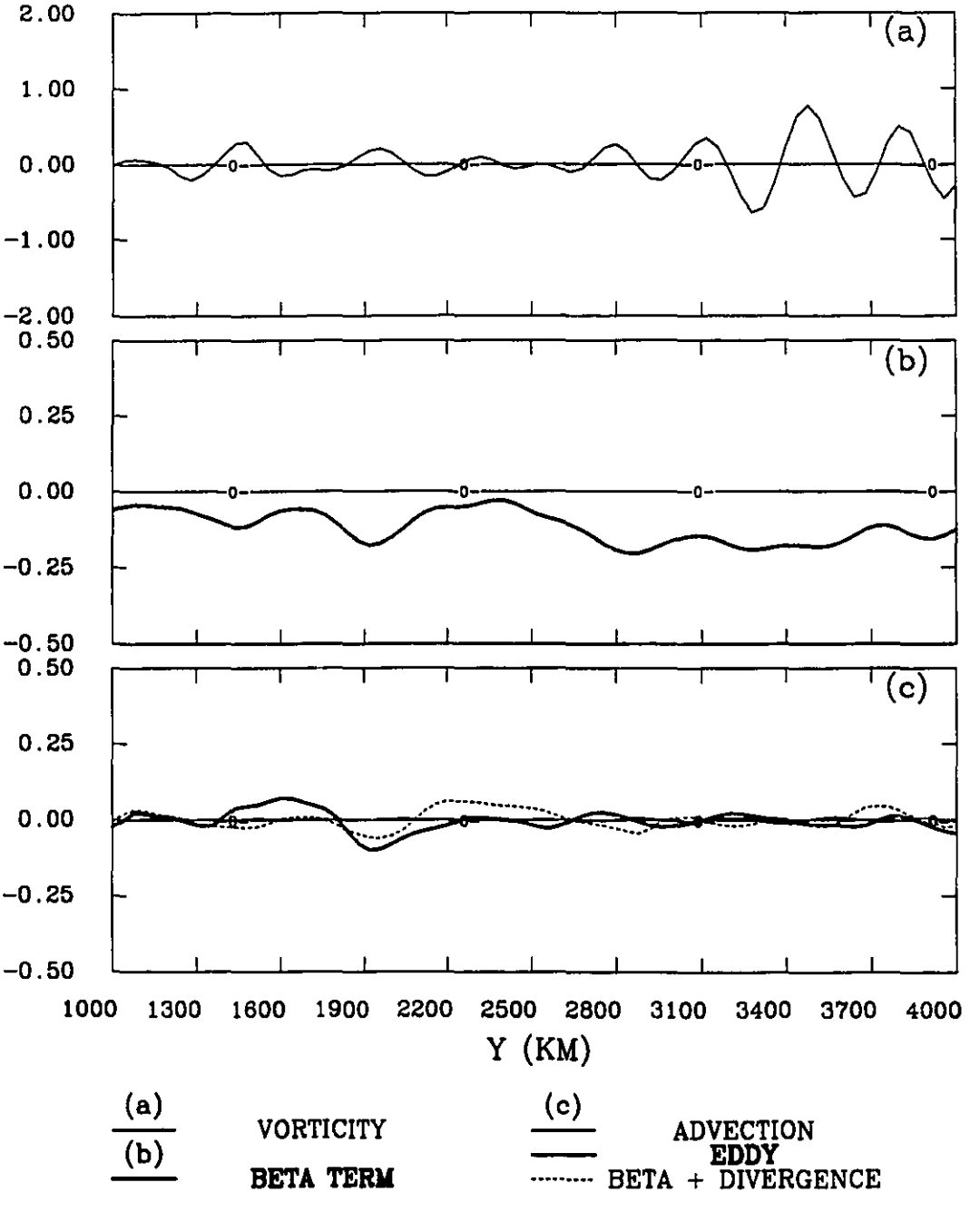

Figure 5.11: Same as Figure 5.8 but at $Z = 2800$ m.

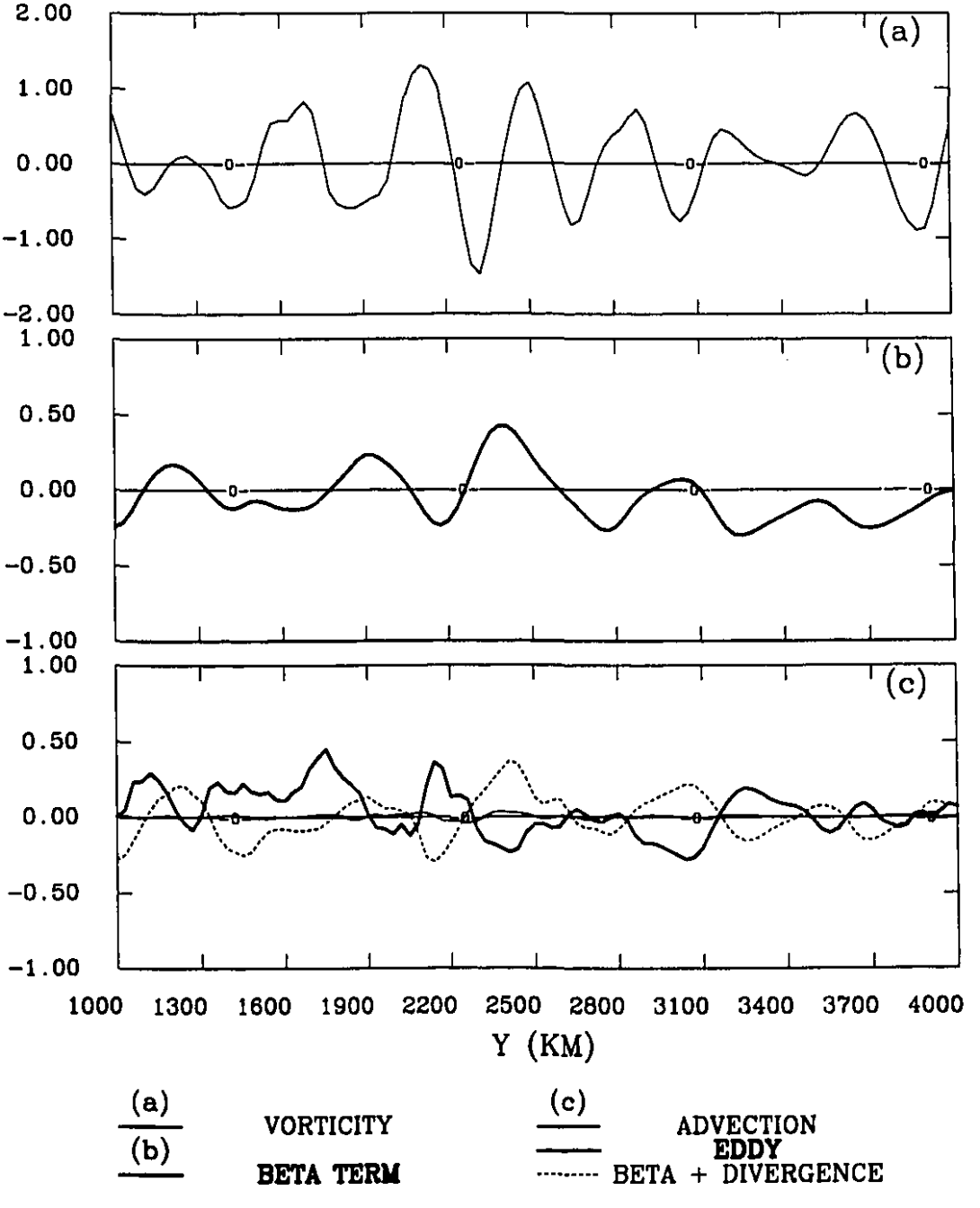

Figure 5.12: Same as Figure 5.9 but at $Z = 2800$ m.

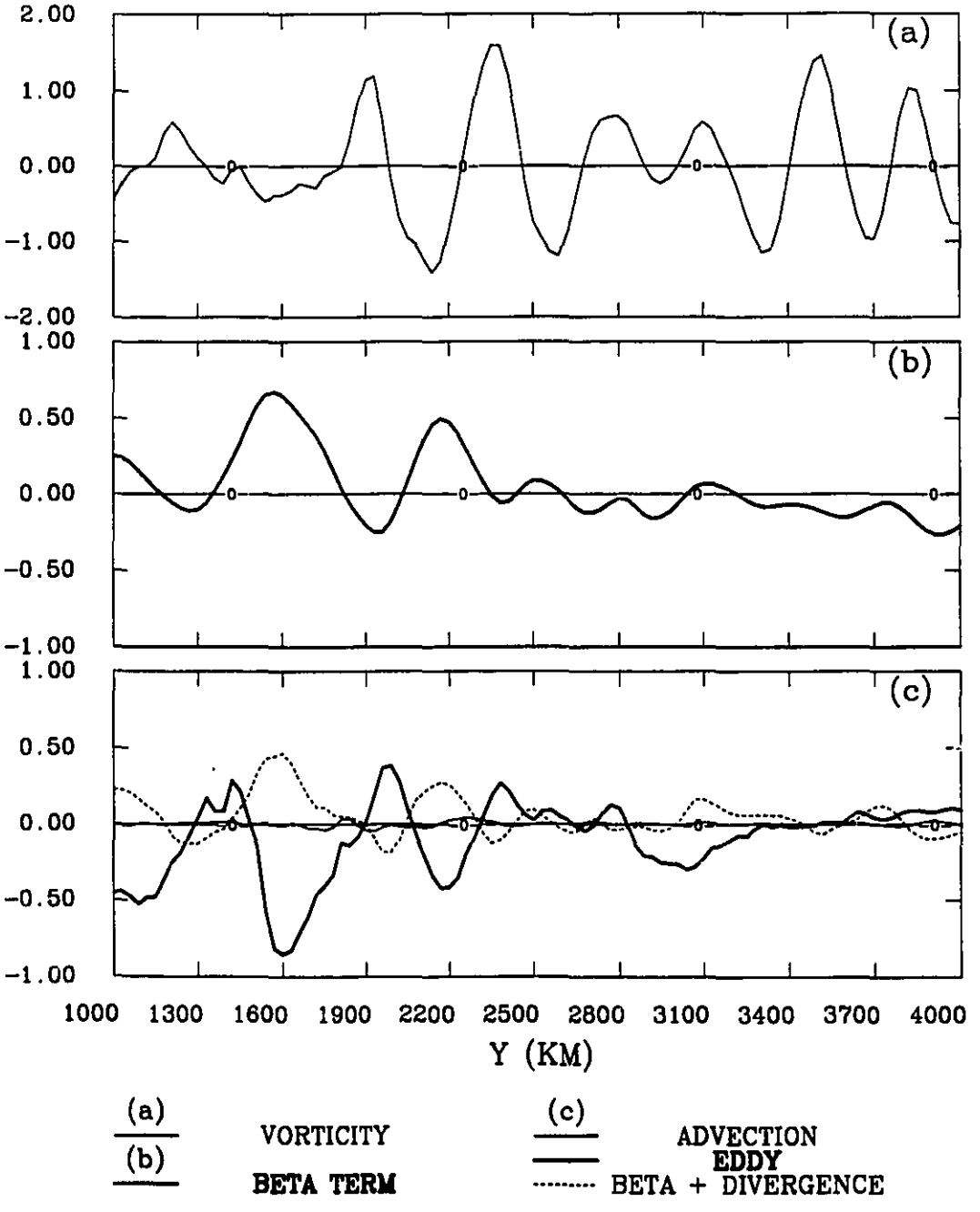

Figure 5.13: Same as Figure 5.10 but at $Z = 2800$ m.

Chapter 6

Conclusions

In this thesis, we first describe the formulation and verification of an ocean circulation model using the Arakawa C-grid. The C-grid has been shown to give more accurate results than the B-grid in the treatment of geostrophic adjustment (Arakawa and Lamb, 1977; Batteen and Han, 1981; Bryan, 1989) and linear convection (Xu and Lin, 1993). We include in the model a semi-implicit formulation of the Coriolis terms, and a small scale dissipative term which depends on the horizontal divergence. The latter reduces the noise in the vertical motion field. The model is formulated with β-plane geometry, and temperature is the only state variable. In the eddy resolving regime, this dissipative term is used only in the subpolar gyre region, where the Rossby radius of deformation is not well resolved. It has little effect elsewhere in the model domain.

The verification experiments are performed using idealized wind and temperature surface forcings in an ocean basin with a comparable size to the North Atlantic. We compare the results obtained at coarse horizontal resolution with those of other models. The surface heat flux, northward heat transport and thermohaline circulation are all simulated well. Results with different forms of frictional parameterizations are also discussed.

The model has been used to study the effect of no slip and free slip boundary conditions, and vertical resolution on eddy energetics and northward heat transport. Little eddy activity is found in the free slip case. There is intense eddy activity in the

no slip case due to both stronger baroclinic and barotropic instabilities. This result shows that a PE model has a different sensitivity to the lateral boundary conditions compared to QG models (Haidvogel et al., 1992). The sub-domain energetic analysis shows that the most energetic regions are concentrated near the western boundary current and its outflow region, where both barotropic and baroclinic instabilities are important. For the remaining regions, barotropic instability is negligible compared to baroclinic instability. The heat transport by the time variant flow is almost compensated by the enhanced time mean flow transport, with the result that the total heat transport for no slip boundary conditions is almost identical to that in the non-eddy resolving coarse resolution regime. For free slip boundary conditions, the heat transport is increased substantially in the midlatitudes and subpolar gyre due to the overshooting of western boundary current, which enhances the baroclinic gyre and overturning heat transport. Increasing the vertical resolution produces stronger baroclinic instability, but leaves the northward heat transport unchanged.

The model was also used to examine the effects of different surface thermal boundary conditions. A ZHCA model has been compared to the more conventional restoring condition. The former, being less constraining than the latter in terms of the surface temperature, allows more mesoscale variability and a stronger mean flow near midlatitudes and in the subpolar regions. Our results suggest that the use of the ZHCA model is one way to increase mesoscale varibility in eddy resolving models. For example, the CME model underestimates such variability in the eastward extension region of the Gulf Stream and in the subpolar gyre (Stammer and Boning, 1992; Treguier, 1992). Another important result is the stronger MKE in the eastward extension region of the midlatitude jets with the ZHCA model. This is especially relevant as Boning and Budich (1992) found that the MKE eastward extension is not sensitive to the horizontal resolution.

The vertical distributions of temperature variance obtained with the ZHCA model show maxima at the surface, subsurface level, or both, depending on geographical location. In contrast, the results we have obtained with the restoring condition all

show a maximum temperature variance below the surface. The vertical heat transport by the time varying flow, which converts eddy available potential energy to eddy kinetic energy, is also increased with the ZHCA model. The use of a constant heat flux and a restoring time scale appropriate for radiative damping in the ZHCA model permits the simulated sea surface temperature to depart more from the reference temperature, and allows advection to play a larger role in the surface heat balance.

The above experiments were used to diagnose the mean momentum and vorticity balance. Both increased horizontal resolution and the use of the ZHCA model can increase the midlatitude jets in the surface and deep layers. The midlatitude eddy momentum convergence represents the dominant ageostrophic contribution to both the mean zonal flow and its variation. The mean advection is consistently less important.

The effects of eddies have been further investigated by using the mean vorticity equation. The results show that eddy convergence term is the most important ageostrophic term, and can be as important as the geostrophic terms. The results show a similar sensitivity to the horizontal resolution and the ZHCA model as the momentum equations.

Our process oriented study is based on a rectangular domain with no bottom topography and is not intended to simulate the real ocean circulation. The results can only be suggestive of what happens in nature, but they should nevertheless be of great help in indicating what should be included in more realistic global and North Atlantic models. As a result of the computational requirement of the latter models, there is less opportunity to vary model parameters and to perform sensitivity studies.

APPENDIX A: A numerical solution of the linear Rayleigh-Bénard convection equations with B- and C-grid formulations

Tellus (1993), 45A, 193–200
Printed in Belgium – all rights reserved

TELLUS
ISSN 0280-6495

A numerical solution of the linear Rayleigh-Bénard convection equations with the *B*- and *C*-grid formulations

By WEIMIN XU and CHARLES A. LIN*, *Department of Atmospheric and Oceanic Sciences, and Center for Climate and Global Change Studies, McGill University, 805 Sherbrooke Street West, Montreal, Quebec, Canada H3A 2K6*

(Manuscript received 18 September 1992; in final form 5 January 1993)

ABSTRACT

The numerical solutions of the linear Rayleigh-Bénard convection equations using the Arakawa *B*- and *C*-grid formulations are compared with the analytic solution. The results show that the *C*-grid simulates better the growth rates of unstable modes. A convective parameterization is required when the horizontal grid size is larger than the horizontal scale of the most unstable mode, the latter being of the same order as the depth scale of the unstable stratification. Non-hydrostatic effects become important when the horizontal grid size is smaller than the scale of the unstable stratification.

1. Introduction

Convective instability can occur in both the atmosphere and ocean. In coarse resolution hydrostatic numerical models, the convective modes are not resolved, and their mixing effects are usually parameterized using convective adjustment. The convective scales can be explicitly resolved in high-resolution non-hydrostatic models. For the ocean, such models are usually formulated using the Arakawa (1972) *B*- and *C*-grids. In this note, we examine the effect of the 2 horizontal grid formulations and horizontal grid sizes on the simulation of Rayleigh-Bénard instability, by comparing their results to those obtained using analytic means. The importance of non-hydrostatic versus hydrostatic effects as a function of the horizontal resolution is also investigated. Martin and Pielke (1983) showed that the hydrostatic approximation remains valid in their study of sea-breeze modeling even when the aspect ratio is of order unity. A similar conclusion is found in the recent review of atmospheric convection by Molinari and Dudek (1992). It is thus of great interest to examine the role of non-hydrostatic effects in an oceanic context as well.

Arakawa and Lamb (1977), and Batteen and Han (1981) examined the effects of the 2 grids on the dispersive properties of inertial-gravity waves, which are essential for geostrophic adjustment. Their results show that for coarse grid (> 100 km) ocean models, the *B*-grid performs better than the *C*-grid, while the opposite obtains at high resolution (< 50 km). The critical parameter is the ratio of the Rossby radius of deformation to the grid size. Convective modes are buoyantly unstable modes; it is thus of interest to determine the performance of the 2 grids for the case of unstable stratification.

Davey and Whitehead (1981) investigated analytically convective instability in a 2-layer rotating fluid, and applied the results to sinking events in the ocean. They suggested that the horizontal scale of the fastest growing mode, found to be of the order of 500 m, may determine the scale of deep convection due to surface cooling. The effect of the earth's rotation is not important, except at small growth rates.

In this study, we use a numerical model to examine the effect of the *B*- and *C*-grid formulations on the convective instability of the linear

* Corresponding author.

Rayleigh-Bénard problem. The model formulation is presented in Section 2, the results in Section 3, and the conclusion in Section 4.

2. Model formulation

The linearized equations for the Rayleigh-Bénard problem are as follows:

$$u_t = -p_x/\rho_0 + fv + \nu \nabla^2 u, \tag{1}$$

$$v_t = -p_y/\rho_0 - fu + \nu \nabla^2 v, \tag{2}$$

$$\varepsilon w_t = -p_z/\rho_0 - g\rho'/\rho_0 + \varepsilon\nu \nabla^2 w, \tag{3}$$

$$T_t = (\Delta T/H)w + \kappa \nabla^2 T, \tag{4}$$

$$u_x + v_y + w_z = 0, \tag{5}$$

$$\rho' = -\alpha\rho_0 T. \tag{6}$$

The notation is standard: u, v, w are the velocity components in the east-west (x), north-south (y) and vertical (z) directions, respectively; t, p, ρ_0, ρ', f, g, ν, κ, α, ∇^2 denote time, pressure, reference density, perturbation density, constant Coriolis parameter, gravitational acceleration, viscosity, thermal diffusivity, thermal expansion coefficient, and the 3-dimensional Laplacian operator, respectively. The basic-state temperature has a linear distribution with a range of ΔT over the depth (H) of the channel. Stress-free boundary conditions ($u_z = v_z = 0$), together with vanishing normal velocity ($w = 0$) and temperature perturbation ($T = 0$), are used at the top and bottom boundaries ($z = 0$, H). The basic state is at rest with no horizontal variation of pressure and density. The multiplier ε takes on the value of either 0 or 1, corresponding to the hydrostatic and non-hydrostatic cases, respectively.

We may assume solutions to (1)–(6) of the following form:

$$[u, v, p] = [U, V, P]\cos(\pi mz/H)e^{i(kx+ly)+\lambda t}, \tag{7}$$

$$[w, T, \rho'] = [W, T^*, \rho^*]\sin(\pi mz/H)e^{i(kx+ly)+\lambda t}, \tag{8}$$

where k, l, m are wavenumbers in the x, y, and z directions; U, V, W, P and T^*, ρ^* are perturbation amplitudes. For unstable modes, $\lambda > 0$ is the growth rate. Substitution of eqs. (7), (8) in eqs. (1)–(6) together with the use of the boundary conditions yields an eigenvalue problem for the growth rate λ. The solution may be obtained analytically, as well as using B- and C-grid formulations. The arrangement for both grids is shown in Fig. 1. The horizontal velocities are carried at the same point for the B-grid, while this is not the case for the C-grid. The numerical solutions depend on the grid resolution δx, δy, δz; further details are presented in the Appendix. The nature of the solution depends on 3 physical dimensionless parameters:

$$\mathrm{Ra} = g\alpha\,\Delta T H^3/\nu\kappa,$$

$$\mathrm{Pr} = \nu/\kappa,$$

$$\mathrm{Ta} = f^2H^4/\nu^2.$$

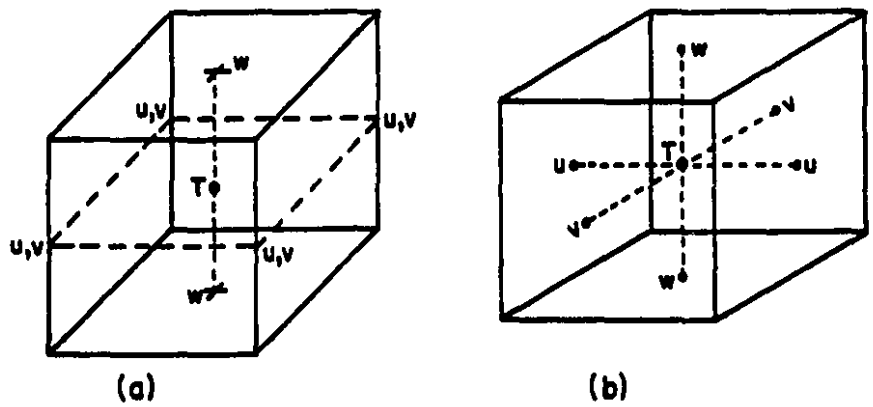

Fig. 1. The arrangement of velocity (u, v, w) and temperature (T) points in a grid box for the (a) B-grid, and (b) C-grid formulation.

The Rayleigh number (Ra) is a measure of the destabilizing temperature stratification ΔT relative to viscous and diffusive effects. The Prandtl number (Pr) is the ratio of the latter coefficients, while the Taylor number (Ta) is a measure of the rotation rate.

3. Results

The classic analytic solution (Chandrasekhar, 1961) of the Rayleigh-Bénard problem shows that unstable modes occur when the Rayleigh number is sufficiently large ($Ra > 27\pi^4/4$), and that the vertical scale of the most unstable mode is that of the gravest mode ($m = 1$), with a horizontal scale of the same order.

We define the dimensionless wavenumbers k_0, l_0, m_0 as

$$k_0 = k\,\delta x/\pi, \qquad l_0 = l\,\delta y/\pi, \qquad m_0 = m\,\delta z/\pi.$$

A numerical model with a grid spacing of δx can only resolve a minimum wavelength of $2\delta x$. This, together with the absence of horizontal boundaries, means that the dimensionless horizontal wavenumbers k_0 and l_0 are constrained to have values between zero and unity. For simplicity, we take the 2 wavenumbers to be identical, $k_0 = l_0$, i.e., symmetry in the zonal and meridional directions is assumed. A limit on the smallest resolved scale is of course not present in the analytic model. In the vertical, the presence of boundaries at $z = 0$ and $z = H$ determines the vertical scale of the gravest mode as $m = \pi/H$. This means that the dimensionless wavenumber $m_0 > \delta z/H$, for both the analytic and numerical models.

In order to compare more readily the wavenumbers of the analytic and numerical models, we define the rescaled wavenumbers as

$$k_{00} = k_0(H/\delta x), \qquad l_{00} = l_0(H/\delta y),$$

$$m_{00} = m_0(H/\delta z).$$

Note that $H/\delta x$, $H/\delta y$ and $H/\delta z$ are measures of the horizontal and vertical resolutions of the numerical model. As k_0, l_0 have values less than unity, this means that k_{00} and l_{00} are smaller than $H/\delta x$ and $H/\delta y$, respectively. For basin scale ocean circulation models used for climate studies, δz is of the same order as $H/10$. We will compare the results for the *B*- and *C*-grid formulations ranging from low ($\delta x = 10H$) to high ($\delta x = H/10$) horizontal resolution. For subsequent results, we take $Ra = 10^7$, $Pr = 1$ and $Ta = 10^2$, and identical grid spacings in the zonal and meridional directions ($\delta x = \delta y$), and $\delta z = H/10$.

Fig. 2 shows the growth rate of the unstable modes of the 3-dimensional non-hydrostatic ($\varepsilon = 1$) analytic model, as a function of the horizontal and vertical wavenumbers; its derivation is given in the Appendix. As noted earlier, the most unstable mode is the gravest mode in the vertical ($m_{00} = 1$) with its horizontal scale of the same order as the vertical scale. The horizontal scales which are actually resolved by the horizontal grid spacings of $\delta x = 10H$, H and $H/10$, are also indicated in Fig. 2. We see that the former 2 grid spacings do not resolve the most unstable mode. However, even for these cases, it is of interest to compare the performance of the 2 grid formulations in simulating the growth rates of the unstable modes.

Fig. 3 shows the growth rates at high horizontal resolution ($\delta x = H/10$) for the non-hydrostatic

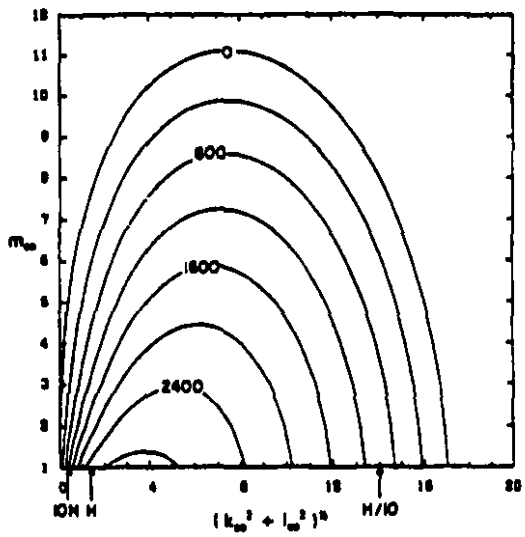

Fig. 2. The dimensionless growth rate ($\lambda H^2/\kappa$) of the unstable mode as a function of the dimensionless horizontal $[(k_{00}^2 + l_{00}^2)^{1/2}]$ and vertical (m_{00}) wavenumbers, from the analytic model. The resolution corresponding to the grid sizes of $\delta x = \delta y = 10H$, H and $H/10$ is shown by the arrow on the abcissa; only modes to the left of the arrow are resolved by the respective numerical model in these cases.

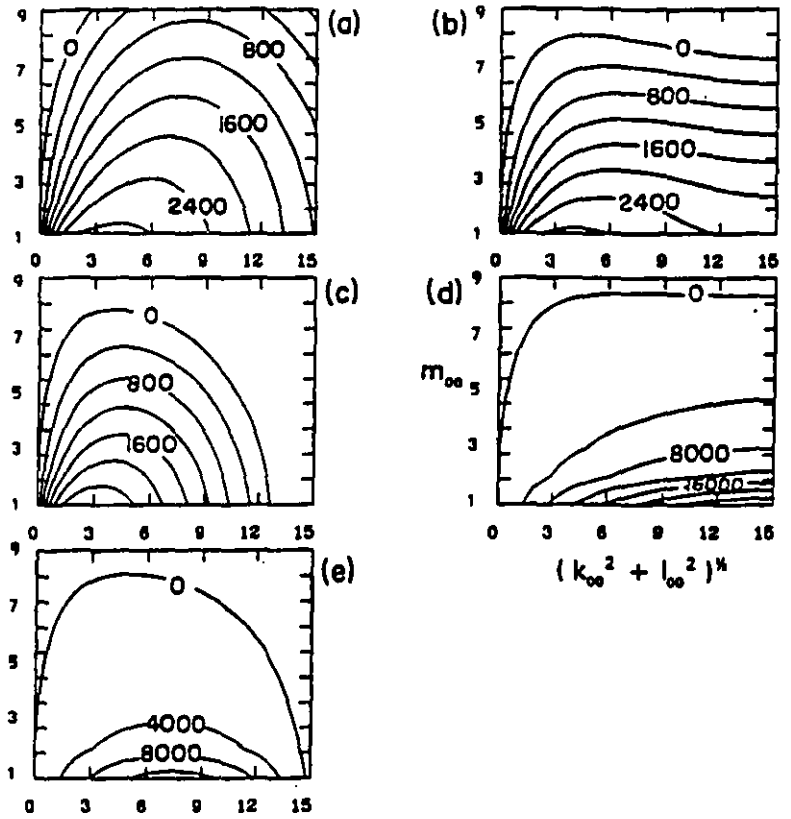

Fig. 3. The growth rate ($\lambda H^2/\kappa$) as a function of the horizontal $[(k_{00}^2 + l_{00}^2)^{1/2}]$ and vertical (m_{00}) wavenumbers, for the analytic and numerical models, with $\delta x = \delta y = H/10$ and $\delta z = H/10$: (a) analytic; (b) non-hydrostatic *C*-grid; (c) non-hydrostatic *B*-grid; (d) hydrostatic *C*-grid; (e) hydrostatic *B*-grid.

analytic model, and the hydrostatic and non-hydrostatic numerical models. We first note that in the limit of infinitely high resolution, the results of the *B*- and *C*-grids both converge to the non-hydrostatic analytic case; this has been verified by increasing the horizontal resolution beyond $\delta x = H/10$ (figures not shown). The most unstable mode is resolved at the latter resolution (Fig. 2), but the behaviour of the two grid formulations differ. For the non-hydrostatic case, the *C*-grid (Fig. 3b) simulates a larger range of unstable horizontal scales compared to the *B*-grid (Fig. 3c), and this is in better agreement with the analytic results (Fig. 3a). Indeed, the *B*-grid yields a high wavenumber cutoff which is not present in the analytic results at these wavelengths. In addition, the growth rate of the most unstable mode is underestimated more by the *B*-grid. This is probably due to the dissipative nature of the grid-point averaging needed to calculate the horizontal pressure gradient in the *B*-grid formulation. The hydrostatic numerical results (Figs. 3d, e) for both grids give completely incorrect growth rates; this is expected for high horizontal resolution, where non-hydrostatic effects become important.

The results for coarser horizontal resolution are shown in Fig. 4 ($\delta x = H$) and Fig. 5 ($\delta x = 10H$). Note that the most unstable mode is no longer resolved at these resolutions (Fig. 2). However, the *B*-grid simulations show a most unstable mode (Figs. 4c and 5c), with a growth rate which is much smaller than the analytic results (Figs. 4a and 5a). In contrast, the *C*-grid performs much better: the growth rate distribution and its magnitude (Figs. 4b, 5b) are both simulated well. We also note that the non-hydrostatic and hydrostatic results for the

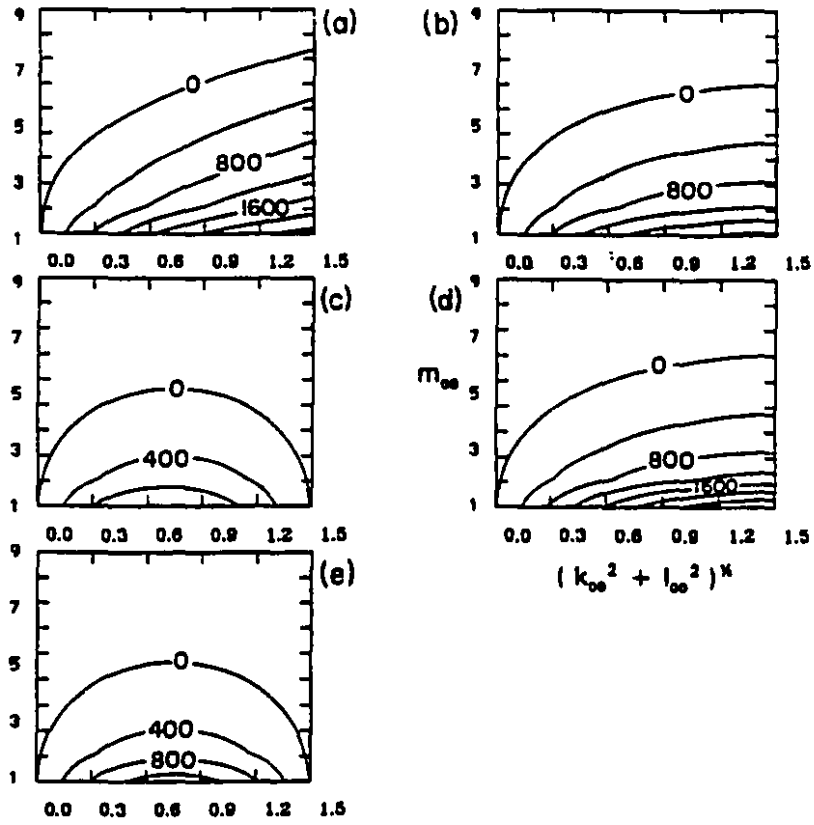

Fig. 4. As Fig. 3, but for $\delta x = \delta y = H$.

2 respective grids are now similar, due to the coarse horizontal resolution used in these cases.

Davey and Whitehead (1981, hereafter referred to as DW), performed an analytic linear stability analysis using a statically unstable two-layer fluid system. Their results suggest a preferred horizontal scale of about 500 m for deep convection events due to surface cooling in the ocean. To simplify the analysis, they did not consider the effects of vertical viscosity. We now estimate the value of the Rayleigh number implied by the choice of the degree of static instability in their model. The latter is measured by the reduced gravity parameters $g' = (\delta\rho/\rho_0)\,g$, where $\delta\rho = \rho_2 - \rho_1$ is the density difference between the 2 layers, and ρ_0 is a reference density value. The magnitude of $\delta\rho$ is small compared to ρ_0, and $\delta\rho < 0$ for static instability. The depths of the two layers are H_1 and H_2. DW estimated a representative value of $g' = -10^{-3}\,\mathrm{m\,s^{-2}}$, corresponding to typical cooling events in the upper ocean, with depths $H_1 = 100$ m and $H_2 = 1000$ m, respectively. To determine an equivalent Rayleigh number, we note that the corresponding temperature stratification is $\delta T = -(g'/g)T_0$, for some reference temperature T_0. This temperature difference occurs over the depth H, which is taken to be the geometric mean of H_1 and H_2; this is of course a crude assumption, as it is not strictly possible to approximate a 2-layer system with a linear profile. This then leads to a value $\mathrm{Ra} = 6 \times 10^7$, with $\alpha = 2.5 \times 10^{-4}\,^{\circ}\mathrm{C}^{-1}$, $\nu = \kappa = 10^{-4}\,\mathrm{m^2\,s^{-1}}$. This is comparable to the value of $\mathrm{Ra} = 10^7$ that we used in the analysis of the performance of the *B*- and *C*-grids. Our results do not change substantially for $\mathrm{Ra} = 10^6$ or 10^8, although the growth rates do increase with the Rayleigh number. We have used identical values of the horizontal and vertical eddy viscosities, which is typical of the vertical viscosity in numerical ocean models. In the latter, the

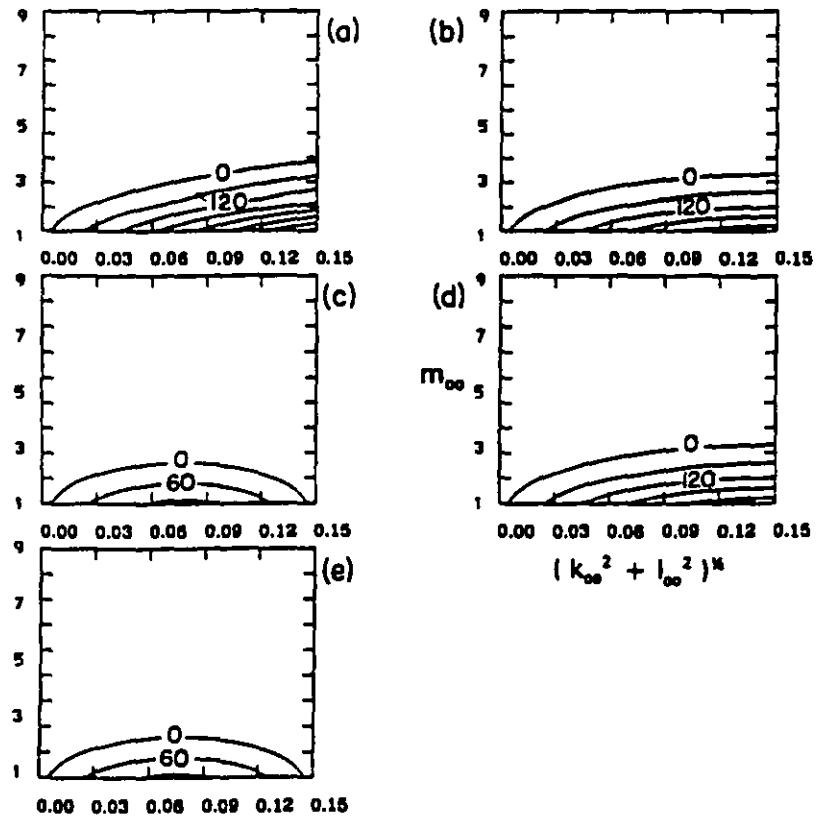

Fig. 5. As Fig. 3, but for $\delta x = \delta y = 10H$.

horizontal viscosity is many orders larger than the vertical value, due to the use of a coarser horizontal resolution compared to the vertical resolution. However, the horizontal contribution to the Laplacian term, which consists of the product of the horizontal viscosity and the horizontal gradient of the velocity shear, remains comparable to the vertical contribution, due to the coarse horizontal resolution ($\Delta x \gg \Delta z$) in such models. This means that the Laplacian diffusion is almost isotropic. In our high horizontal resolution case ($\Delta x = H/10 = \Delta z$), the horizontal and vertical resolutions are equal; there is thus no reason to use a much larger horizontal viscosity. For the intermediate and low horizontal resolution cases ($\Delta x = H$, $10H$; $\Delta z = H/10$), the use of equal horizontal and vertical viscosities means that the former is underestimated compared to that found in numerical models. The use of a larger horizontal viscosity in these cases would severely damp the convective modes, with the *C*-grid still performing better than the *B*-grid. We have thus chosen to use identical values of the horizontal and vertical viscosities.

DW also showed that except for small growth rates found near marginal instability, the effects of the earth's rotation are not important. Thus, the choice of the Taylor number Ta is not crucial; this has been verified in our analysis. We have used a value of $Ta = 10^2$ throughout this study, which corresponds to weak rotation compared to the earth's rotation. Increasing Ta would increase the critical value of the Rayleigh number for the onset of instability, and the result that the *C*-grid performs better than the *B*-grid still remains valid. Increasing the Prandtl number would increase the growth rate; the *C*-grid performs better than the *B*-grid in these cases as well (figures not shown).

4. Conclusions

We have examined the numerical solutions to the classic Rayleigh-Bénard problem in the hydrostatic and non-hydrostatic limits, using both the Arakawa *B*- and *C*-grid formulations. The results have been compared with the analytic solution. The relevant dimensionless parameters are the Rayleigh (Ra), Prandtl (Pr) and Taylor (Ta) numbers, as well as the grid resolution relative to the depth of the fluid ($\delta x/H$, $\delta y/H$, $\delta z/H$).

The most unstable mode is resolved in the non-hydrostatic case when sufficiently high horizontal resolution is used ($\delta x < H$). Conversely, at coarse horizontal resolution ($\delta x > H$), the hydrostatic and non-hydrostatic results become closer. The most unstable mode has horizontal and vertical scales of the same order, is thus not resolved in both cases. This in turn means that a convective adjustment parameterization is required in coarse horizontal resolution models, in both the hydrostatic and non-hydrostatic cases.

In general, the *C*-grid performs better than the *B*-grid in simulating the growth rate of convectively unstable modes. Note that in the Batteen and Han (1981) study of geostrophic adjustment, the *C*-grid also worked better for the frequency of inertial-gravity waves, when the horizontal resolution is smaller than the first modal Rossby radius of deformation.

A difficulty with the simulation of convectively unstable modes in a numerical model is that such instability can occur at any scale, down to that of the grid resolution. We have circumvented this in our study by taking the grid resolution to be less than the scale of the instability ($\delta z < H$), thus allowing the resolution of unstable modes at sufficiently high horizontal resolution. In such cases, the *C*-grid performs better than the *B*-grid. This conclusion is of interest as progressively higher horizontal resolution is used in eddy-resolving ocean circulation models (Holland, 1989).

5. Appendix

Substituting the wave-form solutions given in eqs. (7)–(8) in the linearized eqs. (1)–(6), we obtain the following set of eigenvalue equations for the growth rate λ:

$$[a_{11}-\lambda]U + a_{12}V + a_{13}T^* = 0,$$

$$a_{21}U + [a_{22}-\lambda]V + a_{23}T^* = 0,$$

$$a_{31}U + a_{32}V + [a_{33}-\lambda]T^* = 0.$$

The coefficients $\{a_{ij}\}$ assume different values for the analytic and numerical models. For the analytic model, we have

$$a_{11} = -n^2\nu, \qquad a_{23} = 0,$$

$$a_{12} = -(m/n^2)f, \qquad a_{31} = \Delta T/H,$$

$$a_{13} = g\alpha(k^2+l^2)/n^2, \qquad a_{32} = 0,$$

$$a_{21} = mf, \qquad a_{33} = -n^2\kappa.$$

$$a_{22} = -n^2\nu,$$

In the above, $n^2 = k^2 + l^2 + m^2$ is the 3-dimensional wavenumber. The convective growth rate λ is then obtained as an eigenvalue.

For the numerical model, the coefficients $\{a_{ij}\}$ are given by the following relations.

$$a_{11} = \mathrm{Pr}H^2 d = a_{22},$$

$$a_{33} = H^2 d,$$

$$a_{12} * a_{21} = -b^2\mathrm{TaPr}^2,$$

$$a_{13} * a_{31} = (a_1^2c^2/a_3^2)\mathrm{RaPr},$$

$$a_{23} * a_{32} = (a_2^2c^2/a_3^2)\mathrm{RaPr},$$

$$a_{13} * a_{32} * a_{21} = -(a_1a_2c^2b/a_3^2)\mathrm{RaPr}^2\mathrm{Ta}^{1/2},$$

$$a_{31} * a_{12} * a_{23} = (a_1a_2c^2b/a_3^2)\mathrm{RaPr}^2\mathrm{Ta}^{1/2}.$$

The above equations relate the coefficients to the dimensionless numbers Ra, Pr, Ta, the depth of the fluid H, and the parameters a_1, a_2, a_3, b, c, d. The values of the latter 6 parameters depend on whether the hydrostatic approximation is made, and the grid scheme used; they are shown below.

(1) Hydrostatic *C*-grid model:

$$a_1 = \sin(k\,\delta x/2)/\delta x,$$

$$a_2 = \sin(l\,\delta y/2)/\delta y,$$

$$a_3 = \sin(m\,\delta z/2)/\delta z,$$

$$b = \cos(k\,\delta x/2)\cos(l\,\delta y/2),$$

$$c = \cos(m\,\delta z/2),$$

$$d = -(a_1^2 + a_2^2 + a_3^2).$$

(2) Hydrostatic *B*-grid model:

$a_1 = 2\sin(k\,\delta x/2)\cos(l\,\delta y/2)/\delta x,$

$a_2 = 2\cos(k\,\delta x/2)\sin(l\,\delta y/2)/\delta y,$

$a_3 = 2\sin(m\,\delta z/2)/\delta z,$

$b = 1,$

$c = \cos(m\,\delta z/2),$

$d = -(a_1^2 + a_2^2 + a_3^2).$

(3) Non-hydrostatic *B*- and *C*-grid models:

The non-hydrostatic solutions of *B*- and *C*-grid models are the same as the corresponding hydrostatic counterparts except

$a_{11} = \mathrm{Pr}H^2 d + h_1,$

$a_{22} = \mathrm{Pr}H^2 d - h_1,$

$a_{33} = H^2 d,$

$a_{12} * a_{21} = -h_2 h_3 b^2 \mathrm{TaPr}^2,$

$a_{13} * a_{31} = (a_1^2 c^2/d)\mathrm{RaPr},$

$a_{23} * a_{32} = (a_2^2 c^2/d)\mathrm{RaPr},$

$a_{13} * a_{32} * a_{21} = -(a_1 a_2 c^2 b/d)h_1 \mathrm{RaPr}^2\mathrm{Ta}^{1/2},$

$a_{31} * a_{12} * a_{23} = (a_1 a_2 c^2 b/d)h_2 \mathrm{RaPr}^2\mathrm{Ta}^{1/2},$

and where

$h_1 = -a_1 a_2 b/d,$

$h_2 = 1 - a_2^2/d,$

$h_3 = 1 - a_2^2/d.$

Acknowledgments

Helpful discussion with Dr. D. L. Zhang during the course of this work is gratefully acknowledged. Ms. U. Seidenfuss helped in the preparation of the figures. Financial support is provided by the Natural Sciences and Engineering Research Council (NSERC), and the Atmospheric Environment Service (AES) of Canada. The preparation of this work was aided by the computational facilities of CERCA (Centre de Recherche en Calcul Appliqué). Helpful comments from 2 anonymous referees, which improved the manuscript, are gratefully acknowledged.

REFERENCES

Arakawa, A. 1972. *Numerical simulation of weather and climate*, Technical Report no. 7. Department of Meteorology, University of California, Los Angeles, USA.

Arakawa, A. and Lamb, V. R. 1977. Computational design of the basic dynamical processes of the UCLA general circulation model. In: *Methods of computational physics*, vol. 17. Academic Press, New York, 173–265.

Batteen, M. L. and Han, Y.-J. 1981. On the computational noise of finite difference schemes used in ocean models. *Tellus 33*, 387–396.

Chandrasekhar, S. 1961. *Hydrodynamic and hydromagnetic stability*. Dover Press, New York, USA, 645 pp.

Davey, M. K. and Whitehead, J. A., Jr. 1981. Rotating Rayleigh-Taylor instability as a model of sinking events in the ocean. *Geophys. Astrophys. Fluid Dynamics 17*, 237–253.

Holland, W. R. 1989. Experiences with various parameterizations of subgrid scale dissipation and diffusion in numerical models of ocean circulation. In: *Parameterization of small-scale processes*. Proceedings of Aha Huliko'a Winter Workshop, 1989, P. Muller and D. Henderson (eds.). Hawaii Institute of Geophysics, Hawaii, USA, pp. 99–116.

Martin, C. L. and Pielke, R. 1983. The adequacy of the hydrostatic assumption in sea breeze modeling over flat terrain. *J. Atmos. Sci. 40*, 1472–1481.

Molinari, J. and Dudek, M. 1992. Parameterization of convective precipitation in mesoscale numerical models: a critical review. *Mon. Wea. Rev. 120*, 326–344.

APPENDIX B: Finite difference equations

We give below the finite difference forms of the governing equations

(a) Continuity equation

$$w(i,j,k+1/2) - w(i,j,k-1/2) = \Delta z_k [\frac{u(i+1,j,k) - u(i,j,k)}{\Delta x} + \frac{v(i,j+1,k) - v(i,j,k)}{\Delta y} \quad \text{(B1)}$$

The boundary conditions for Equation (B1) are:

$$u(i,j,k) = 0$$

at longitudinal boundaries

$$v(i,j,k) = 0$$

at latitudinal boundaries

$$w(i,j,k+1/2) = 0$$

at the surface (z=0)

(b) Temperature equation

$$\frac{\partial T_{i,j,k}}{\partial t} = \frac{TU_{i+1/2,j,k} - TU_{i-1/2,j,k}}{\Delta x} + \frac{TX_{i+1/2,j,k} - TX_{i-1/2,j,k}}{\Delta x} + \frac{TV_{i,j+1/2,k} - TV_{i,j-1/2,k}}{\Delta y} + \frac{TY_{i,j+1/2,k} - TY_{i,j-1/2,k}}{\Delta y} + \frac{TW_{i,j,k+1/2} - TW_{i,j,k-1/2}}{\Delta z} + \frac{TZ_{i,j,k+1/2} - TZ_{i,j,k-1/2}}{\Delta z} \quad \text{(B2)}$$

with

$$\begin{aligned} TU_{i+1/2,j,k} &= u(i,j,k)(T_{i,j,k} + T_{i+1,j,k})/2 \\ TX_{i+1/2,j,k} &= (T_{i+1,j,k} - T_{i,j,k})/\Delta x \\ TV_{i,j+1/2,k} &= v(i,j,k)(T_{i,j,k} + T_{i,j+1,k})/2 \\ TY_{i,j+1/2,k} &= (T_{i,j+1,k} - T_{i,j,k})/\Delta y \\ TW(i,j,k+1/2) &= w(i,j,k+1/2)(T_{i,j,k} + T_{i,j,k+1})/2 \\ TZ(i,j,k+1/2) &= (T_{i,j,k+1} - T_{i,j,k})/\Delta z_{k+1/2} \end{aligned}$$

and $\Delta z_{k+1/2} = z_{k+1} - z_k$

The lateral boundary conditions are:

$$TU_{i+1/2,j,k} = 0$$

$$TX_{i+1/2,j,k} = 0$$

$$TV_{i,j+1/2,k} = 0$$

$$TY_{i,j+1/2,k} = 0$$

$$TW_{i,j,k+1/2} = 0$$

the bottom boundary condition is

$$TZ_{i,j,k+1/2} = 0$$

the surface boundary condition is

$$TZ_{i,j,k+1/2} = Q^T_{i,j}$$

(c) Hydrostatic equation

$$p_{k+1} - p_k = -\rho_{k+1/2} g \Delta z_{k+1/2} \qquad \text{(B3)}$$

where $\rho_{k+1/2} = (\rho_{k+1} + \rho_k)/2$, consistent with the definition of $T_{i,j,k+1/2}$.

(d) Momentum equations

$$\begin{aligned}\frac{\partial u_{i,j,k}}{\partial t} &= -\frac{1}{\rho_0}\frac{\partial p_{i,j,k}}{\partial x} + \frac{uu_{i+1/2,j,k} - uu_{i-1/2,j,k}}{\Delta x} \\ &+ \frac{uv_{i,j+1/2,k} - uv_{i,j-1/2,k}}{\Delta y} + \frac{uw_{i,j,k+1/2} - uw_{i,j,k+1/2}}{\Delta z} \\ &+ \frac{ux_{i+1/2,j,k} - ux_{i-1/2,j,k}}{\Delta x} + \frac{uy_{i,j+1/2,k} - uy_{i,j-1/2,k}}{\Delta y} \\ &+ \frac{uz_{i,j,k+1/2} - uz_{i,j,k-1/2}}{\Delta z_k} + f\overline{v}^{xy} \\ &+ \epsilon\lambda\frac{D_{i+1/2,j,k} - D_{i-1/2,j,k}}{\Delta x} \end{aligned} \tag{B4}$$

where

$$\begin{aligned} uu_{i+1/2,j,k} &= (u_{i,j,k} + u_{i+1,j,k})(u_{i,j,k} + u_{i+1,j,k})/4 \\ uv_{i,j+1/2,k} &= (u_{i,j,k} + u_{i,j+1,k})(v_{i,j,k} + v_{i+1,j,k})/4 \\ uw_{i+1/2,j,k} &= (w_{i,j,k} + w_{i,j,k+1})(u_{i,j,k} + u_{i+1,j,k})/4 \\ ux_{i+1/2,j,k} &= A_{MH}(u_{i+1,j,k} - u_{i,j,k})/\Delta x \\ uy_{i,j+1/2,k} &= A_{MH}(u_{i,j+1,k} - u_{i,j,k})/\Delta y \\ uz_{i,j,k+1/2} &= A_{MV}(u_{i,j,k+1} - u_{i,j,k})/\Delta z \\ \overline{v}_{i,j,k}{}^{xy} &= (v_{i,j,k} + v_{i+1,j,k} + v_{i,j+1,k} + v_{i+1,j+1,k})/4 \end{aligned}$$

$$\begin{aligned}\frac{\partial v_{i,j,k}}{\partial t} &= -\frac{1}{\rho_0}\frac{\partial p_{i,j,k}}{\partial y} + \frac{vu_{i+1/2,j,k} - vu_{i-1/2,j,k}}{\Delta x} \\ &+ \frac{vv_{i,j+1/2,k} - vv_{i,j-1/2,k}}{\Delta y} + \frac{vw_{i,j,k+1/2} - vw_{i,j,k+1/2}}{\Delta z} \\ &+ \frac{vx_{i+1/2,j,k} - vx_{i-1/2,j,k}}{\Delta x} + \frac{vy_{i,j+1/2,k} - vy_{i,j-1/2,k}}{\Delta y} \\ &+ \frac{vz_{i,j,k+1/2} - vz_{i,j,k-1/2}}{\Delta z_k} - \overline{f\overline{u}_{i,j,k}{}^{x}}^{y} \\ &+ \epsilon\lambda\frac{D_{i,j+1/2,k} - D_{i,j-1/2,k}}{\Delta y} \end{aligned} \tag{B5}$$

where

$$vu_{i+1/2,j,k} = (v_{i,j,k} + v_{i+1,j,k})(u_{i,j,k} + u_{i+1,j,k})/4$$

$$
\begin{aligned}
vv_{i,j+1/2,k} &= (v_{i,j,k} + v_{i,j+1,k})(v_{i,j,k} + v_{i+1,j,k})/4 \\
vw_{i+1/2,j,k} &= (v_{i,j,k} + v_{i+1,j,k})(w_{i,j,k} + w_{i,j,k+1})/4 \\
vx_{i+1/2,j,k} &= A_{MH}(v_{i+1,j,k} - v_{i,j,k})/\Delta x \\
vy_{i,j+1/2,k} &= A_{MH}(v_{i,j+1,k} - v_{i,j,k})/\Delta y \\
vz_{i,j,k+1/2} &= A_{MV}(v_{i,j,k+1} - v_{i,j,k})/\Delta z \\
\overline{f\overline{u}_{i,j,k}{}^{x}}{}^{y} &= (f_j(u_{i,j,k} + u_{i+1,j,k}) + f_{j+1}(u_{i,j+1,k} + u_{i+1,j+1,k}))/4
\end{aligned}
$$

The special treatment of Coriolis terms conserve the total energy, i.e., there is no net gain of kinetic energy due to the Coriolis terms.

(e) Elliptic equation for surface pressure

$$
\frac{1}{\rho_0}\nabla^2 p_s = \frac{\partial \hat{G}_x}{\partial x} + \frac{\partial \hat{G}_y}{\partial y} \tag{B6}
$$

where

$$
\nabla^2 p_{si,j,k} = \frac{p_{si+i,j,k} - 2p_{si,j,k} + p_{si-1,j,k}}{\Delta x^2} + \frac{p_{si,j+1,k} - 2p_{si,j,k} + p_{si,j-1,k}}{\Delta y^2}
$$

APPENDIX C: Definition of energetic variables

Available potential energy:

$$P = \frac{1}{2}\alpha g \int\int\int \frac{(T-\hat{T})^2}{d\hat{T}/dz} dV \quad \text{(C1)}$$

Kinetic energy:

$$K = \frac{1}{2}\int\int\int (u^2+v^2) dV \quad \text{(C2)}$$

where $\hat{()}$ represents the deviation from a spatial average, and dV is the volume element.

We decompose a predictive variable into its time mean and deviation,

$$u = \overline{u}+u'; v = \overline{v}+v'; w = \overline{w}+w'; T = \overline{T}+T' \quad \text{(C3)}$$

Mean available potential energy ($\overline{P}$):

$$\frac{1}{2}\alpha g \int\int\int \frac{(\overline{T}-\hat{T})^2}{d\hat{T}/dz} dV \quad \text{(C4)}$$

Eddy available potential energy (P'):

$$\frac{1}{2}\alpha g \int\int\int \frac{\overline{(T'^2)}}{d\hat{T}/dz} dV \quad \text{(C5)}$$

Mean kinetic energy ($\overline{K}$):

$$\frac{1}{2}\int\int\int (\overline{u}^2+\overline{v}^2) dV \quad \text{(C6)}$$

Eddy kinetic energy (K'):

$$\frac{1}{2}\int\int\int\overline{(u'^2+v'^2)}dV \tag{C7}$$

Integrating over a closed domain, an energy component can change by the work of external forces, wind, buoyancy, diffusion, and frictional dissipation. We do not discuss the last two processes here in detail.

The four main energy conversion mechanisms can be defined as: The conversion of mean kinetic energy to mean potential energy by the work of mean buoyancy:

$$(\overline{P},\overline{K}) = \alpha g\int\int\int\overline{w}\overline{T}dV, \tag{C8}$$

The conversion of mean to eddy potential energy (baroclinic instability):

$$(\overline{P},P') = \alpha g\int\int\int\frac{\overline{u'T'}\partial\overline{T}/\partial x+\overline{v'T'}\partial\overline{T}/\partial y}{d\hat{T}/dz}dV, \tag{C9}$$

The conversion from eddy potential to eddy kinetic energy:

$$(P',K') = -\alpha g\int\int\int\overline{w'T'}dV, \tag{C10}$$

The conversion from mean kinetic to eddy kinetic energy(barotropic instability):

$$(\overline{K},K') = -\int\int\int(\overline{u'u'}\frac{\partial\overline{u}}{\partial x}+\overline{u'v'}(\frac{\partial\overline{v}}{\partial x}+\frac{\partial\overline{u}}{\partial y})+\overline{v'v'}\frac{\partial\overline{v}}{\partial y})dV. \tag{C11}$$

APPENDIX D: Components of mean heat transport

We decompose the mean northward heat transport F^H into six terms (Bryan, 1986). We first define the vertical and zonal means

$$< () >= \frac{1}{H}\int_{-H}^{0} ()dz \tag{D1}$$

$$[()] = \frac{1}{L_X}\int_{0}^{L_X} ()dx \tag{D2}$$

In the following, $*$ indicates a deviation from the zonal average, and $'$ indicates a deviation from the vertical average. For simplicity, we drop the overbar on v and T, understanding that they represent the time mean values. The six components are Barotropic gyre transport:

$$F^H{}_1 = HL_X C_p[< v >^* < T >^*], \tag{D3}$$

Baroclinic overturning transport:

$$F^H{}_2 = HL_X C_p < [v_B{}'][T'] >, \tag{D4}$$

Baroclinic gyre transport:

$$F^H{}_3 = HL_X C_p[< v_B{}'^* T'^* >], \tag{D5}$$

Ekman overturning transport:

$$F^H{}_4 = HL_X C_p < [v_E{}'][T'] >, \tag{D6}$$

Ekman gyre transport (this vanishes for a zonally uniform wind stress, as in our study):

$$F^H{}_5 = HL_X C_p < v_E{}'^* T'^* >, \tag{D7}$$

Explcit diffusion:

$$F^H{}_6 = HL_X C_p [< T >]_y. \tag{D8}$$

In the above v_E is the Ekman current and is assumed to be confined wholly to the upmost model layer, and v_B is the remainder of the baroclinic velocity.

REFERENCE

Andrich P., P., Delecluse, C., Levy and G., Madec, 1988: A Multi-tasked General Circulation Model of the Ocean, Report of Laboratoire d'Oceanographie Dynamique et de Climatologie, University Paris 6, 75002 Paris, France.

Arakawa, A., 1972: Numerical simulation of weather and climate, Technical Report no. 7. Department of Meteorology, University of California, Los Angeles, USA.

Arakawa, A., and V.R., Lamb, 1977: Computational design of the basic dynamical processes of the UCLA general circulation model. In: *Methods of Computational Physics*, **17**, Academic Press, New York, 173-265.

Arhan, M., A., Colin de Verdiere, and H., Mercier, 1989: Direct observations of the mean circulation at 48°N in the Atlantic Ocean. *J. Phys. Oceanogr.*, **19**, 161-181.

Asselin, R.A., 1972: Frequency filter for time integration. *Mon. Wea. Rev.*, **100**, 487-490.

Barnier, B., B.L., Hua, and C., Le Provost, 1991: On the catalytic role of high baroclinic modes in eddy-driven large-scale circulations. *J. Phys. Oceanogr.*, **21**, 976-997.

Batteen, M.L., and Y.-J., Han, 1981: On the computational noise of finite difference schemes used in ocean models. *Tellus*, **33**,387-396.

Blandford, R., 1971: Boundary conditions in the homogeneous ocean model. *Deep-Sea Res.*, **18**, 739-751.

Bleck, R., C., Rooth, D., Hu, and L.T., Smith, 1992: Salinity-driven thermocline transients in a wind- and thermohaline-forced isopycnal coordinate model of the North Atlantic. *J. Phys. Oceanogr.*, **22**, 1486-1505.

Blumberg, A.F., and G.L., Mellor, 1987: A description of a three-dimensional coastal circulation model, in *Three-Dimensional Coastal Ocean Models*, **4**, edited by N. Heaps, pp. 208, American Geophysical Union, Washington, D.C..

Boning, C.W., 1989: Influences of a rough bottom topography on flow kinetic in an eddy-resolving circulation model. *J. Phys. Oceanogr.*, **19**, 77-97.

Boning, C.W., Doscher, R., and R.G., Budich, 1991: Seasonal transport variation in the subtropical North Atlantic: Experiments with an eddy-resolving model. *J. Phys. Oceanogr.*, **21**, 1271-1289.

Boning, C.W., and R.G., Budich, 1992: Eddy dynamics in a primitive equation model: Sensivity to horizontal resolution and friction. *J. Phys. Oceanogr.*, **22**, 361-381.

Bretherton, F.P., 1982: Ocean climate modelling. *Progress in Oceanography*, **11**, Pergamon, 93-129.

Brugge, R., H.L., Jones, and J.C., Marshall, 1991: Non-hydrostatic ocean modeling for studies of open-ocean deep convection. *Proc. Workshop on Deep Convection and Deep Water Formation in the Oceans*, Monterey, Elsevier Science, 325-340.

Bryan, F.O., 1986: Maintenance and variability of the thermohaline circulation. Ph.D. thesis, GFDL, Princeton University, Princeton, NJ, pp. 254.

Bryan, F.O., 1987: Parameter sensitivity of primitive equation ocean general circulation models. *J. Phys. Oceanogr.*, **17**, 970-985.

Bryan, F.O. and W.R. Holland, 1989: A high resolution simulation of the wind- and

thermohaline-driven circulation in the North Atlantic Ocean. In: "Parameterisation of Small-Scale Processes", Proc. of 'Aha Huliko'a Winter Workshop 1989, edited by P. Muller and D. Henderson, 99-116, Hawaii Institute of Geophysics, University of Hawaii, Hawaii, 1989.

Bryan, K., 1963: A numerical investigation of a nonlinear model of a wind-driven ocean. *J. Atmos. Sci.*, **20**, 594-606.

Bryan K, S. Manabe and P. Pacanowski, 1975: A global ocean-atmosphere climate model. Part II: The ocean circulation. *J. Phys. Oceanogr.*, **5**, 30-46.

Bryan, K., 1969: A numerical method for the study of the circulation of the world ocean. *J. Comput. Phys.*, **4**, 347-376.

Bryan, K., 1984: Accelerating the convergence to equilibrium of ocean-climate models. *J. Phys. Oceanogr.*, **14**, 666-673.

Bryan, K., 1986: Polarward buoyancy transport in the ocean and mesoscale eddies. *J. Phys. Oceanogr.*, **16**, 927-933.

Bryan, K., 1987: Potential vorticity in models of the ocean circulation. *Q. J. R. Meteorol. Soc.*, **13**, 713-734.

Bryan, K., 1989: The design of numerical models of the ocean circulation. In "Oceanic Circulation Models: *Combining Data and Dynamics*", Anderson, D.L.T. and J. Willebrand (eds.), 465-500.

Bryan, K., 1991: Poleward heat transport in the ocean: A review of a hiearchy of models of increasing resolution. *Tellus*, **43AB**, 104-115.

Cai, W., R., Greatbatch, and S., Zhang, 1993: Interdecadal variability in an ocean model driven by a constant, zonally-redistributed surface heat flux. *J. Phys. Oceanogr.*, submitted.

Chandrasekhar, S., 1961: *Hydrodynamic and hydromagnetic stability.* Dover Press, New York, USA, 645 pp.

Charney, J.G., and M.E. Stern, 1962: On the stability of internal baroclinic jets in a rotating atmosphere. *J. Atmos. Sci.*, **19**, 159-172.

Charney J.G., and G.R., Flierl, 1981: Oceanic analogues of large-scale atmospheric motions. In *Evolution of Physical Oceanography*, Warren B.A. and Wunsch C. (eds.), chapter 18, MIT press, Cambridge, MA.

Cheney, R.E., and P.L., Richardson, 1976: Observed decay of a cyclonic Gulf Stream ring. *Deep-Sea Res.*, **23**, 143-155.

Cheney, R.E., and J.G., Marsh, 1983: Global mesoscale variability from collinear tracks of SEASAT altimeter data. *J Geophys. Res.*, **88**, 4,343-4,354.

Clarke, R.A., and J.-C., Gascard, 1983: The formation of Labrador Sea water, Part I. Large- scale processes. *J. Phys. Oceanogr.*, **13**, 1764-1778.

Colin de Verdiere, A., 1988: Buoyancy driven planetary flow. *J. Mar. Res.*, **46**, 215-265.

Colin de Verdiere, A., 1989: On the interaction of wind and buoyancy driven gyres. *J. Mar. Res.*, **47**, 595-633.

Cox, M.D., and K. Bryan, 1984: A numerical model of the ventilated thermocline. *J. Phys. Oceanogr.*, **14**, 674-687.

Cox, M.D., 1984: A primitive equation, three dimensional model of the ocean. GFDL Ocean Tech. Report No. 1, Princeton, NJ.

Cox, M.D., 1985: An eddy-resolving numerical model of the ventilated thermocline. *J. Phys. Oceanogr.*, **15**, 1312-1324.

Cox, M.D., 1987: An eddy-resolving numerical model of the ventilated thermocline: Time dependence. *J. Phys. Oceanogr.*, **17**, 1044-1056.

Dantzler, H.L., Jr., 1977: Potential energy maxima in the tropical and subtropical North Atlantic. *J. Phys. Oceanogr.*, **7**, 512-519.

Davey, M.K., and J.A., Whitehead, 1981: Rotating Rayleigh-Taylor instability as a model of sinking events in the ocean. *Geophys. Astrophys. Fluid Dynamics*,

17, 237-253.

Demin, Y.L., and A.S., Sarkisyan, 1977: Calculation of equatorial currents. *J. Mar. Res.* **35**, 339-356.

Dengg, J., 1993: The problem of Gulf Stream separation: A barotropic approach. *J. Phys. Oceanogr.*, **23**, 2182-2200.

Deser, C., and M.L. Blackmon, 1993: Surface climate variations over the North Atlantic Ocean during winter: 1900-1989, *J. Climate*, **6**, 1743-1753.

Dietrich, D.E., M.G., Marietta, and P.J. Roache, 1987, An ocean modeling system with turbulent boundary layers and topography: numerical description. *International Journal for Numerical Methods in Fluids* **7**, 833-855.

Dietrich, D.E., P.J., Roache, and M.G., Marietta, 1990: Convergence studies with the Sandia Ocean Modeling System. *International Journal for Numerical Methods in Fluids* **11**, 127-150.

Dietrich, D.E., and C.A., Lin, 1994: Eddy shedding in Gulf of Mexico. *J. Geophys. Res.*, (in press).

Dickinson, R.E., 1981: Convergence rate and stability of ocean-atmosphere coupling schemes with a zero-dimensional climate model. *J Atmos. Sci.*, **38**, 2112-2120.

Dukowicz, J.K., R.D., Smith, and R.C., Malone, 1993: A reformulation and implementation of the Bryan-Cox-Semtner ocean model on the Connected Machine. *J. Atmospheric and Oceanic Tech.*, **10**, 195-208.

Emery, W.J., C.C., Ebbesmeyer, and J.P., Dugan, 1980: The fraction of the vertical isotherm deflections associated with eddies: An estimate from multiship XBT surveys. *J. Phys. Oceanogr.*, **10**, 885-899.

Emery, W.J., 1983: On the geographic variability of the upper level mean and eddy fields in the North Pacific and North Atlantic. *J. Phys. Oceanogr.*, **13**, 269-291.

Emery, W.J., W.G., Lee, and L., Magaard, 1984: Geographic and seasonal distributions of Brunt-Vaisala frequency and Rossby radii in the North Pacific and North Atlantic. *J. Phys. Oceanogr.*, **14**, 294-317.

Ezer, T., and G.L., Mellor, 1992: A numerical study of the variability and the separation of the Gulf Stream, induced by surface atmospheric forcing and lateral boundary flows. *J. Phys. Oceanogr.*, **22**, 660-682.

Fu, L., 1983: On the wavenumber spectrum of ocean variability observed by the SEASAT altimeter. *J Geophys. Res.*, **88**, 4,331-4,341.

Fu, L., T., Keffer, P.P. Niiler, and C., Wunsch, 1982: Observations of mesoscale variability in the western North Atlantic: A comparative study. *J. Mar. Res.*, **40**, 809-848.

Gordon, A.L., 1978: Deep Antarctic convection west of Maud Rise. *J. Phys. Oceanogr.*, **8**, 600-612.

Gough, W., 1991: Ph.D. Thesis. Dept. of Atmospheric and Oceanic Sciences, McGill University.

Gough, W., and C.A. Lin, 1992: The response of an ocean general circulation model to long time scale surface anomalies. *Atmosphere-Ocean*, **30**, 653-674.

Greatbatch, R., 1987: A model for the inertial recirculation of a gyre. *J. Mar. Res.*, **45**, 601-634.

Greatbatch, R., and S., Zhang, 1994: An interdecadal oscillation in an idealised ocean basin forced by constant heat flux. *J. Climate*, in press.

Greatbatch, R., G. Li and S., Zhang, 1994: Assimilating time dependent surface data into an ocean climate model. *J. Phys. Oceanogr.*, (submitted).

Heldley, M., and M.K., Yau, 1988: Radiation boundary conditions in numerical modeling, *Mon. Wea, Rev.*, **116**, 1721-1736.

Haidvogel, D.B., and W.R. Holland, 1978: The stability of ocean currents in eddy-resolving general circulation models. *J. Phys. Oceanogr.*, **8**, 393-413.

Haidvogel, D.B., J., Wilkin, and J., Young, 1991: A Semi-spectral Primitive Equation Ocean Circulation Model Using Vertical Sigma and Orthogonal Curvilinear Horizontal Coordinates. *J. Comput. Phys.*, **94**, 151-185.

Haidvogel, D.B., J.C., McWilliams, and P.R., Gent, 1992: Boundary current separation in a Q-G eddy resolving ocean circulation model. *J. Phys. Oceanogr.*, **22**, 882-902.

Han, Y.J., 1975: Numerical simulation of mesoscale ocean eddies. Ph.D. thesis, UCLA, 154 pp.

Han, Y.J., 1984: A numerical world ocean general circulation model. Part II. A baroclinic experiment. Dynamics of Atmospheres and Oceans, **8**, 141-172.

Haney, R.L., 1971: Surface thermal boundary condition for ocean circulation model. *J. Phys. Oceanogr.* **1**, 241-248.

Harlow, F.H., and J.E., Welch, 1965: Numerical calculation of the time-dependent viscous incompressible flow of fluid with free surface, *The Physics of Fluid*, **8** , No. 12, 2182-2189.

Harrison, D.E., and A.R. Robinson, 1978: Energy analysis of open regions of turbulent flows-Mean eddy energetics of a numerical ocean circulation experiment. *Dynamics of Atmospheres and Oceans*, **2**, 185-211.

Harrison, D.E., and W.R. Holland, 1981: Regional eddy vorticity transport and the equilibrium vorticity budgets of a numerical model ocean circulation. *J. Phys. Oceanogr.*, **11**, 190-208.

Harrison, D.E., and A.J., Semtner, 1986: On the generation of deep mean flows: Some numerical experiments. *J. Geophys. Res.*, **91**, 2569-2573.

Holland, W.R., and L.B., Lin, 1975a: On the generation of mesoscale eddies and their contribution to oceanic general circulation. Part I: A preliminary numerical experiment. *J. Phys. Oceanogr.*, **5**, 642-657.

Holland, W.R., and L.B., Lin, 1975b: On the generation of mesoscale eddies and

their contribution to oceanic general circulation. Part II: A parameter study. *J. Phys. Oceanogr.*, **5**, 658-669.

Holland, W.R., 1978: The role of mesoscale eddies in the general circulation of the ocean-Numerical experiments using a wind-driven quasi-geostrophic model. *J. Phys. Oceanogr.*, **8**, 363-392.

Holland, W.R., and P.B., Rhines, 1980: An example of eddy induced ocean circulation. *J. Phys. Oceanogr.*, **10**, 1010-1031.

Holland, W.R., Harrison, D.E. and A.J. Semtner, 1983: Eddy-resolving numerical models of large-scale ocean circulation. In Eddies in Marine Sciences, Robinson, A.R. (ed.), Springer-Verlag, 379-403.

Holland, W.R., and W.J., Schmitz, 1985: Zonal penetration scale of model midlatitude jets. *J. Phys. Oceanogr.*, **15**, 1859-1875.

Holland, W.R., and M.L., Batteen, 1986: The parameterization of sub-grid-scale heat diffusion in eddy-resolved ocean circulation models. *J. Phys. Oceanogr.*, **16**, 200-206.

Holton, J.R., 1979: *An Introduction to Dynamic Meteorology*, Academic Press, Inc., (London) LTD.

Huang, R.X., 1990: Does atmospheric cooling drive the Gulf Stream separation. *J. Phys. Oceanogr.*, **20**, 750-757.

Hurlburt, H.E., A.J., Wallcraft, Z., Sirkes, and E. J., Metzger, 1992: Modeling of the global and Pacific Oceans: On the path to eddy-resolving ocean prediction, *Oceanography*, **5**, 9-18.

Ikeda, M., 1993: Mesoscale variabilities and Gulf Stream bifurcation in the Newfoundland Basin observed by the Geosat Altimeter Data, *Atmosphere-Ocean*, **31(4)**, 567-589.

Jones H., and J., Marshall, 1993: Convection with Rotation in a neutral ocean: A study of open-ocean deep convection. *J. Phys. Oceanogr.*, **23**, 1009-1039.

Killworth, P., 1977: Mixing on the Weddell Sea continental slope. *Deep-Sea Res.*, **24**, 427-448.

Killworth, P., 1979: On 'chimney' formations in the ocean. *J. Phys. Oceanogr.*, **9**, 531-554.

Killworth, P., 1983: Deep convection in the world ocean. *Rev. Geophys. and Space Phys.*, **21**, 1-26.

Killworth, P., 1985: A two-level wind and buoyancy driven thermocline model. *J. Phys. Oceanogr.*, **15**, 1414-1432.

Killworth, P., 1989: On the parameterization of deep convection in ocean models. In: "Parameterisation of Small-Scale Processes", Proc. of 'Aha Huliko'a Winter Workshop 1989, edited by P. Muller and D. Henderson, 99-116, Hawaii Institute of Geophysics, University of Hawaii, Hawaii,1989.

Lai, D.Y., and P.L., Richardson, 1977: Distribution and movement of Gulf Stream rings. *J. Phys. Oceanogr.*, **7**, 670-683.

Legg, S., and J., Marshall, 1993: A Heton model of the spreading phase of open-ocean deep convection. *J. Phys. Oceanogr.*, **23**, 1040-1056.

Le Traon, D.Y., M.C., Rouquet, and C., Boissier, 1990: Spatial scales of mesoscale variability in the North Atlantic as deduced from Geosat Data. *J. Geophys. Res.*, **95**, 20,267-20,285.

Lin, C.A., and D.E., Dietrich, 1994: A study of low Reynolds number convective adjustment. *Geophys. Astrophys. Fluid Dyn.*, (in press).

Marotzke, J., 1991: Influence of Convective Adjustment on the stability of the thermohaline circulation. *J. Phys. Oceanogr.*, **21**, 903-907.

Marotzke, J., and J., Willebrand, 1991: Multiple equilibria of the global thermohaline circulation. *J. Phys. Oceanogr.*, **21**, 1372-1385.

Marshall, J.C., 1984: Eddy-mean-flow interaction in a barotropic ocean model. *Quart. J. Roy. Meteor. Soc.*, **110**, 573-590.

Marshall, J.C., and G. Nurser, 1988: On the recirculation of the subtropical gyre. *Quart. J. Roy. Meteor. Soc.*, **114**, 1517-1534.

Marshall, D., and J., Marshall, 1992: Zonal penetration scale of midlatitude oceanic jets. *J. Phys. Oceanogr.*, **22**, 1018-1032.

Martin, C.L., and R., Pielke, 1983: The adequacy of the hydrostatic assumption in sea breeze modeling over flat terrain. *J. Atmos. Sci.*, **40**, 1472-1481.

Martinson, D.G., P.D. Killworth, and A.L. Gordon, 1981: A convective overturn model for the Weddell Polynya. *J. Phys. Oceanogr.*, **11**, 466-488.

McWilliams, J.C., N.J., Norton, P.R., Gent, and D.B., Haidvogel, 1990: A linear balance model of wind-driven, midlatitude ocean circulation. *J. Phys. Oceanogr.*, **20**, 1349-1378.

MEDOC group, 1970: Observation of formation of deep water in the Mediterranean Sea. *Nature*, **227**, 1037-1040.

Mellor, G, 1992: USER'S Guide for A Three-Dimensional,Primitive Equation, Numerical Ocean Circulation Model. Atmospheric and Oceanic Sciences Program, Princeton University, Princeton, NJ 08540.

Mintz, Y., 1979: On the simulation of the oceanic general circulation. Report of the JOC study Conference on Climatic Models: Performance, Intercomparison and Sensitivity Studies. *Vol. II.* GARP Publ. Ser. No. 22, 607-687.

Molinari, J., and M. Dudek, 1992: Parameterization of convective precipitation in mesoscale numerical models: a critical review. *Mon. Wea. Rev.*, **120**, 326-344.

Mysak, L.A., E. R. Johnson, and W. W. Hsieh, 1981: Baroclinic and barotropic instabilities of coastal currents. *J. Phys. Oceanogr.*, **11**, 209-230.

Mysak, L.A., and C. A. Lin, 1990: Role of the oceans in climate variability and climate change. *The Canadian Geographer*, **34**, 352-369.

Nishida, H., and W.B., White, 1982: Horizontal eddy fluxes of momentum and kinetic

energy in the near-surface of the Kuroshio Extension. *J. Phys. Oceanogr.*, **12**, 160-170.

Oort, A.H., and T.H., Vonder Haar, 1976: On the observed cycle in the ocean-atmosphere heat balance over the northern hemisphere. *J. Phys. Oceanogr.*, **6**, 781-800.

Reynauds, T., A.J., Weaver, and R. Greatbatch, 1994: The mean circulation of Northwestern Atlantic Ocean: An observational study. (in preparation).

Rhines, P.B., 1975: Waves and turbulence on a beta-plane. *J. Fluid Mech.*, **69**, 417-443.

Rhines, P.B., 1977: The dynamics of unsteady currents. *The Sea*, **6**, Wiley Interscience, 189-318.

Richardson, P.L., C., Maillard, and T.B., Stanford, 1979; The physical structure and life history of cyclonic Gulf Stream ring. *J. Geophys. Res.*, **84**, 7727-7741.

Richardson, P.L., 1983: Eddy kinetic energy in the North Atlantic from surface drifters. *J Geophys. Res.*, **88**, 4,355-4,367.

Richardson, P.L., 1985: Average velocity and transport of the Gulf Stream near 55 °W. *J Mar. Res.*, **43**, 83-111.

Richman, J.G., C. Wunsch and N.G. Hogg, 1977: Space and time scales of mesoscale motion in the western North Atlantic. *Rev. Geophys. Space Phys.*, **15**, 385-420.

Richtmyer, R.D., and K.W., Morton, 1967. *"Difference Methods for Initial Value problems"*, Interscience Publisher, New York, 1967.

Robert, A., 1966: The integration of a low order spectral form of the primitive meteorological equations. *Jour. of Meteo. Soc. of Japan*, **44**, No. 5, 237-245.

Robert, A, 1981: A stable numerical integration scheme for the primitive meteorological equations. *Atmos. Ocean*, **19**, 35-46.

Robinson, A. R., D.E. Harrison, Y. Mintz, and A.J. Semtner, 1977: Eddies and the general circulation of an idealized oceanic gyre: A wind and thermally driven primitive equation numerical experiment. *J. Phys. Oceanogr.*, **7**, 182-207.

Rossby, H.T., S.C. Riser and A.J. Mariano, 1983: The western North Atlantic- a Lagrangian viewpoint. In Eddies in Marine Sciences, Robinson, A.R. (ed.), Springer-Verlag, 66-88.

Sadourny, R., 1975: The dynamics of finite-difference models of the shallow water equations. *J. Atmos. Sci.*, **32**, 680 (1975).

Sarmiento, J.L., and K., Bryan, 1982: An ocean transport model for the North Atlantic, *J Geophys. Res.*, **87**, 394-408.

Sarmiento, J.L., 1986: On the north and tropical Atlantic heat balance. *J Geophys. Res.*, **91**, 11,677-11,689.

Schmitz, W.J., Jr., 1977: On the deep general circulation in the western North Atlantic. *J Geophys. Res.*, **81**, 4981-4982.

Schmitz, W.J., Jr., and W.R., Holland, 1982: A preliminary comparison of selected numerical eddy-resolving general circulation experiments with observations. *J. Mar. Res.*, **40**, 75-117.

Schmitz, W.J., Jr., and W.R., Holland, 1986: Observed and modeled mesoscale variability near the Gulf Stream and Kuroshio Extension. *J Geophys. Res.*, **91**, 9624-9638.

Schmitz, W.J., Jr., P.P., Niiler, R.L., Bernstein, and W.R., Holland, 1982: Recent long-term moored instrument observations in the western North Pacific. *J Geophys. Res.*, **87**, 9425-9440.

Schopt, P.S., 1983: On the equatorial waves and El Nino: II, Effects of air-sea thermal coupling, *J. Phys. Oceanogr.*, **13**, 1878-1893.

Seaver, G., 1987: Geographic and temporal eddy variability in the Western North Atlantic as sensed by satellite: An eddy generation mechanism. *J. Phys.*

Oceanogr., **17**, 1602-1618.

Semtner, A.J., 1974: An oceanic general circulation model with bottom topography. *Numerical Simulation of Weather and Climate*, Tech. Rep. No. 9, Dept. of Meteor., UCLA, 99 pp.

Semtner, A.J., and Y. Mintz, 1977: Numerical simulation of the Gulf Stream and mid-ocean eddies. *J. Phys. Oceanogr.*, **7**, 208-230.

Semtner, A.J., and W.R., Holland, 1978: Intercomparison of quasi-geostrophic simulations of the western North Atlantic Circulation with primitive equation results. *J. Phys. Oceanogr.*, **8**, 735-754.

Semtner, A.J., 1986(a): History and methodology of modelling the circulation of the world ocean. In: *Advanced Physical Oceanographic Numerical Modelling*, edited by James J. O'Brien. (D. Reidel Publishing Company, 1986), p. 23.

Semtner, A.J., 1986(b): Finite-difference formulation of a world ocean model. In: *Advanced Physical Oceanographic Numerical Modelling*, edited by James J. O'Brien. (D. Reidel Publishing Company, 1986), p. 187.

Semtner, A.J., and R.M., Chervin, 1988: A simulation of the global ocean circulation with resolved eddies. *J Geophys. Res.*, **93**, 15,502-15,522.

Semtner, A.J., and R.M., Chervin, 1992: Ocean general circulation from a global eddy-resolving model. *J Geophys. Res.*, **97**, 5,493-5550.

Smagorinsky, J., 1963: General circulation experiments with the primitive equations: I. The basic experiments. *Mon. Wea. Res.* **91** 99-164.

Spall, M.A., 1990: Circulation in The Canary Basin: A model/data analysis. *J. Geophys. Res.*, **95**, 9611-9628.

Stammer, D., and C.W., Boning, 1992: Mesoscale variability in the Atlantic Ocean from Geosat Altimetry and WOCE High-Resolution Numerical Modeling. *J Phys. Oceanogr.*, **22**, 732-752.

Tai, C.-K., and W.B., White, 1990: Eddy variability in the Kuroshio Extension as

revealed by Geosat altimetry: Energy propagation away from the jet, Reynolds stress, and seasonal cycle. *J Phys. Oceanogr.*, **20**, 1761-1777.

Takano, K., 1974: A general circulation model for the world ocean. Technical Report No. 8, Dept. of Meteorology, Univ. of California, Los Angeles.

Takano, K., 1975: Relationship between the grid size and coefficient of lateral eddy viscosity in the finite difference computation of the linear vorticity equation in the ocean. *Jour. Ocean. Soc. Japan*, **31**, 105-108.

Thompson, J.D., and W.J. Schmitz, 1989: A limited-area model of the Gulf Stream: Design, initial experiments, and model-data intercomparison. *J Phys. Oceanogr.*, **19**, 791-814.

Treguier, A.M., and H.L., Hua, 1987: Oceanic quasi-geostrophic turbulence forced by stochastic wind fluctuation. *J Phys. Oceanogr.*, **17**, 397-411.

Treguier, A.M., and H.L., Hua, 1988: Influence of bottom topography on stratified quasi-geostrophic turbulence in the ocean. *Geophys. Astrophys. Fluid Dynamics*, **43**, 265-305.

Treguier, A.M., 1992: Kinetic energy analysis of an eddy resolving, primitive equation model of the North Atlantic Ocean. *J. Geophys. Res.*, **97**, 687-701.

Vastano, A.C., J.E., Schmitz, and D.E., Hagan, 1980: The physical oceanography of two rings observed by the cyclonic ring experiment, Part I: Physical Structure. *J. Phys. Oceanogr.*, **10**, 493-513.

Veronis, G., 1966: Wind-driven ocean circulation-2: Numerical solutions of nonlinear problem. *Deep-Sea Res.*, **13**, 31-57.

Veronis, G., 1981: Dynamics of large-scale ocean circulation. In *Evolution of Physical Oceanography*, Warren B.A. and Wunsch C. (eds.), chapter 5, MIT press, Cambridge, MA.

Weaver, A.J., and E.S., Sarachik, 1990: On the importance of vertical resolution in certain ocean circulation models. *J. Phys. Oceanogr.*, **20**, 600-609.

Weaver, A.J., and E.S., Sarachik, 1991: The role of mixed boundary conditions in numerical models of the ocean's climate. *J. Phys. Oceanogr.*, **21(9)**, 1470-1493.

Wood, R.A., 1988: Unstable waves on oceanic fronts: Large-amplitude behavior and mean flow generation. *J. Phys. Oceanogr.*, **18**, 775-787.

Wunsch, C., 1981: Low-Frequency Variability of the Sea. In *Evolution of Physical Oceanography*, Warren B.A. and Wunsch C. (eds.), chapter 11, MIT press, Cambridge, MA.

Wunsch, C., 1983: Western North Atlantic Interior. In Eddies in Marine Sciences, Robinson, A.R. (ed.), Springer-Verlag, 66-88.

Wyrtki, K., L., Magaard, and J. Hager, 1976: Eddy energy in the oceans. *J. Geophys. Res.*, **81**, 2641-2646.

Xu, W., and C.A. Lin, 1993: A numerical solution of the linear Rayleigh-Bernard convection equations with B- and C-grid formulations. *Tellus*, **45A**, 193-200.

Yoshida, K., 1970: Subtropical countercurrents: band structures revealed from CSK data. *The Kuroshio*, J.C. Marr, Ed., East-West Center Press, 197-204.

Zhang, S., C.A. Lin, and R. Greatbatch, 1992: A thermocline model for ocean-climate studies. *J. Mar. Res.*, **50**, 99-124.

Zhang, S., R. Greatbatch, and C.A., Lin, 1993: A re-examination of the polar halocline catastrophe and implications for coupled ocean-atmosphere models. *J. Phys. Oceanogr.*, **23(2)**, 287-299.